Effect of the Incorporation of Defects in ZnO Nanocrystals on the Generation of Reactive Oxygen Species for Applications in Photodynamic Therapy

By

MILTON A. MARTINEZ JULCA

A thesis submitted in partial fulfillment of the requirements for the degree of
MASTER OF SCIENCE
In
Physics
UNIVERSITY OF PUERTO RICO, MAYAGUEZ CAMPUS
2015

Approved by:

---------- ----------
Oscar Perales-Pérez, PhD Date
President, Graduate Committee

---------- ----------
Félix Fernández, PhD Date
Member, Graduate Committee

---------- ----------
Dorial Castellanos, PhD Date
Member, Graduate Committee

---------- ----------
Omar Colon Reyes, PhD Date
Representative of Graduate Studies

---------- ----------
Rafael A. Ramos, PhD Date
Director of Department of Physics

Abstract

Photodynamic therapy (PDT) is an alternative to traditional cancer treatments. This approach involves the use of photosensitizer (PS) agents and their interaction with light. As a consequence, cytotoxic reactive oxygen species (ROS) are generated that will kill cancer cells. On the other hand, ZnO is a biocompatible and nontoxic material with the capability to generate ROS, specifically singlet oxygen (SO), which makes this material a promising candidate for PDT. Unfortunately up to now, the photo-excitation of ZnO-based requires the use of ultraviolet (UV) light, which limits their biomedical applications.

Doping of ZnO is expected to induce defects in the host oxide structure and favor the formation of trap states that should affect the electronic transitions related to the generation of SO. Accordingly, the present work reports the effect of the type and level of dopant element (Lithium, Li, and Titanium, Ti species) on the ZnO structure and its capability to generate SO.

Pure and doped ZnO nanoparticles were synthesized under size-controlled conditions using a modified version of the polyol method. These modified version was conducive to the synthesis of highly monodisperse nanoparticles with a particle size in the 87-140 nm range. Photoluminescence (PL) spectroscopy measurements of pure and doped ZnO nanoparticles, excited by UV light (345 nm), revealed the characteristics emission peaks for ZnO as well as other peaks associated to defect states in the band gap. The observed increase of the emission intensity of the emission peak corresponding to defect states, relative to the intensity of the main emission peak, was attributed to the promotion of trap states associated to interstitial Zn or to the substitution of Zn ions by dopant species. Use of a sensor green kit evidenced the enhancing effect of the dopant type and concentration on the capability of the ZnO-based nanoparticles to generate SO species under UV illumination. This dopant-dependence of SO generation was attributed to the enhancement of the concentration of trap states in the host ZnO, a fact that was supported by PL measurements.

The two-photon excitation of ZnO-based nanoparticles would enable the use of visible or NIR light to excite this material, opening actual possibilities to expand their use to the biomedical field. As an attempt to verify the capability of ZnO-based nanoparticles to be used in 2-photon PDT, a preliminary work based on the two-photon fluorescence microscopy (TPFM) technique, using near-infrared light of 690nm, was carried out. The observed PL transitions will favor triplet states formation necessary to yield cytotoxic reactive oxygen species. Accordingly, the fact that ZnO-based nanoparticles can be excited by the 2-photon approach using a 690nm light would enable this nanomaterial to become cytotoxic to cancer cells via photo-induced ROS generation.

Resumen

La terapia fotodinámica (por sus siglas en inglés, PDT) es una alternativa a los tratamientos tradicionales contra el cáncer. Este enfoque implica el uso de agentes fotosensitizadores y su interacción con la luz. Como consecuencia, especies reactivas de oxigeno (por sus siglas en inglés, ROS) citotóxicas son generadas que destruirán las células cancerosas. Por otro lado, óxido de zinc (por sus siglas en inglés, ZnO) es un material biocompatible, no tóxico, biodegradable con la capacidad de generar ROS, específicamente oxígeno singlete (por sus siglas en inglés, SO), lo cual hace este material sea un candidato prometedor para PDT. Desafortunadamente, hasta ahora, los materiales basados en ZnO requieren la excitación bajo luz ultravioleta (UV), lo que limita sus aplicaciones biomédicas.

Dopando ZnO es esperado inducir defectos en la estructura del ZnO y favorece la formación de estados trampas que deberían afectar las transiciones electrónicas relacionadas a la generación de SO. En consecuencia, el presente trabajo reporta el efecto del tipo y nivel de elemento dopante (Litio (Li) y Titanio (Ti)) en la estructura del ZnO y su capacidad para generar SO.

Nanoparticulas de ZnO puros y dopados fueron sintetizadas bajo condiciones de tamaño controlado utilizando a una versión modificada del método de poliol. Esta versión modificada fue propicia para la síntesis de nanopartculas altamente monodispersas con un tamaño de particula en el rango de 87-140 nm. Mediciones de espectroscopia de nanoparticulas de ZnO puras y dopadas, bajo luz ultravioleta (345nm), revela los picos de emisión caracteristicos del ZnO, así como estados de defectos en la banda de energía prohibida. El incremento observado de la intensidad de emisión de los picos de emisión de los estados de defectos, relativo a la intensidad del pico principal de emisión del ZnO, fue atribuido a la promoción de estados trampas asociado a los zincs intersticiales o sustitución de iones de Zn por especies dopantes. El uso de un kit de verde sensor evidencia el efecto de incremento del tipo y concentración del dopante en la capacidad de las nanoparticulas basadas en ZnO para generar especies de SO bajo la iluminación de UV. Este elemento

dopante depende de la generación de SO puede ser atribuido al aumento de concentración de estados trampas en la estructura del ZnO, un hecho que fue soportado por las mediciones de fotoluminiscencia.

La foto excitación con 2 fotones de nanoparticulas basadas en ZnO permitiría el uso de luz visible o luz cercana al infrarrojo para excitar el material, abriendo posibilidades reales para ampliar su uso en el campo biomédico. Como intento de verificar la capacidad de las nanoparticulas basadas en ZnO para ser usados en PDT con 2 fotones, un trabajo preliminar basado en la técnica de microscopia de fluorescencia de dos fotones (por sus siglas en inglés, TPFM) usando luz cercana al infrarrojo de 690 nm, se llevó a cabo. Las transiciones de fotoluminiscencia observados favorecerán la formación de estados tripletes necesarios para producir especies reactivas de oxígeno. En consecuencia, el hecho que las nanoparticulas basadas en ZnO puedan ser excitadas por el enfoque de 2 fotones usando luz de 690 nm puede permitir este nanomaterial para convertirse citotóxico para las células del cáncer a través de la generación de ROS foto inducida.

Dedicatory

Dedicated to my family

In special to my mother and sister, Rosa and Karina.

Acknowledgments

Many people have helped me accomplish this thesis, and I owe my gratitude to all of them. Firstly, I will give highest appreciation to my advisor Dr. Oscar Perales-Pérez and my Co-Advisor, Dr. Félix Fernández. My gratitude is not only for giving me a chance to work on this amazing project and their friendship, but also for their effective instruction, and broad knowledge given to me during this time.

Thanks to Dr. Heidy Sierra, for their scientific support and help in measurements of Multiphoton Microscopy. I would like to thank Dr. Boris Renteria, for their support in the measurements and scientific discussions at The Nano materials Processing Laboratory at UPRM.

I also want to thank Dr. Marcos De Jesus Ruiz, Dr. Jorge Rios, Dr. Samuel Hernandez, Dr. Joaquin Aparicio and graduate students Elena Flores-Velez and Ana Vega, for their support and collaboration. My gratitude to Dr. Oscar Resto, Nanoscopy Facilities IFN, for the Field Emission Scanning Electron Microscopy measurements.

Last but not least, to my undergraduate student who helped me the most during the editing and the revising of this Thesis and with her collaboration for this research to progress favorably, I just want to say, thanks for everything Ivonnemary Rivera. A special note of gratitude to Myriam Padilla, Adelaida Rivera and Karem Torres, administrative staff of CREST.

This material is based upon work supported by The NSF under Grant No. HRD 0833112 (CREST Program).

Table of contents

1. Introduction

1.1 Motivation

In recent years, nanotechnology has represented a great impact to medical developments in the so-called nanomedicine. The progress in nanomedicine is explained by the synthesis of various nanomaterials exhibiting outstanding properties (optical, magnetic, electrochemical, bactericidal, others) for biomedical applications including drug delivery, sensing, and cancer diagnosis and treatment; for instance, graphene, carbon nanotubes, zinc oxide and gold nanomaterials have unique features that cannot be found in the bulk material. Organic nanoparticles, such as dendrimers, liposomes, polymers, among others, also exhibit interesting properties that enable their potential use in biomedicine [1]. However, inorganic nanoparticles (NPs) have received much attention for both, diagnostic and therapeutic purposes, for cancer detection and therapies [1, 2]. NPs are materials that have a size in the nanometer scale, which enable them to get inside the capillaries and penetrate through tissues. Besides, some nanomaterials are biocompatible, i.e. they are biodegradable and not toxic to the human immune system [3].

Nowadays, the patients diagnosed with cancer have increased their probability of surviving because of the great efforts invested in biomedical research; advances in cancer research have represented more benefits in the prevention, diagnostic, detection, and treatment arenas. However, despite of the rapid developments in the fight against an approximately 585,720 U.S residents, between children and young adults, will die of some type of cancer disease in the year of 2014, due to their cancer diagnosis being in the final stage. It is expected that the number of deaths caused by cancer will increase in 6.4 million since 2012 to 2035 [4]; therefore, the development of new materials, compounds and therapies to detect, prevent, and treat the cancer will become indispensable.

The intensive research in cancer has promoted the development of various diagnosis and treatments approaches, including magnetic resonance imaging (MRI), radiotherapy, chemotherapy, surgery, and hyperthermia. MRI is a noninvasive clinical method that uses non-ionizing electromagnetic fields at different ratio frequency pulses and generates detailed images of organs that help to determine the existence of certain diseases.

Nowadays, MRI is used in the detection of diseases like breast cancer and prostate cancer, among others [5, 6]. Radiotherapy or radiation therapy, requires the use of high energy X-rays, gamma rays that in turn, destroy the DNA of carcinogenic cell. Unfortunately, this treatment produces severe side effects such as skin damage, fetal harm, permanent hair loss, and also produces mutations in the healthy genes that cause secondary malignancies cells. Moreover, chemotherapy uses cytotoxic drugs, between the main drugs are: Taxol, Vinblastine and Doxorubicin. The disadvantage of this treatment are that these types of drugs are not selective, hypersensitive, the cancers cells are resistant at these drugs, and can even degrade in toxic moieties affecting others body organs like the liver and also cause cardio-toxicity [3]. An alternative, tough more radical, cancer treatment is surgery that consists in the extirpation of tumor volume, but in most cases it has been combined with chemotherapy or radiotherapy [3, 7]. Hyperthermia, consists in the use of heat as source to damage the cancer cells, this therapy actuates sensitizing sites by radiation and involves a large time period (around 42 weeks) [3, 8]. All these traditional treatment routes cause secondary effects and damage to adjacent healthy cells.

The photodynamic therapy (PDT) represents a more advantageous route; it is minimally invasive, exhibit low toxicity, and is more selective. This approach requires the presence of a photosensitizer (PS) that is activated with external source at one specific wavelength [9-11]. PDT has been used in treatment of superficial tumors, e.g. bladder, melanoma, skin, and esophagus. This therapy consists of the administration of the PS, through intravenous injection or topically, in the proximity of the pathological sites. Next, the cancer tissue is irradiated with non-thermal light to lead the excitation of PS. Upon excitation of the PS by light and the presence of triplet electronic state, the generation of cytotoxic reactive oxygen species (ROS) or singlet oxygen (SO) species takes place from initial molecular oxygen, which can destroy cancer cells without side effects to surrounding tissues [12]. Although few commercial photosensitizers are available, Porphyrin, Chlorine, and Phthalocyaninea, among others, none of them fulfill the requirements of an ideal PS. Porphyrin is a FDA-approved PS; however, it still hosts some disadvantages: insolubility in water, which leads to a stronger interaction between PS molecules that decreases the production of SO, and aggregation in aqueous medium that makes it more difficult to get inside of the diseased tissues [13].

On the other hand, the use of inorganic NPs in cancer therapy is becoming more promising due to their high surface-to-volume ratios, tuning of optical properties, better accumulation in tumor zones, and capacity to generate reactive oxygen species ROS [14, 15]. Inorganic NPs like Zinc Oxide (ZnO) have received much interest in cancer research. ZnO nanoparticles have the following properties: is a non-toxic material, biodegradable, shows chemical and thermal stability, luminescent at ambient and high temperatures, biocompatibility, and can react with water to generate ROS [16-18]. Despite of these favorable features, the research of the effect of dopants on the structural and functional properties, related to generation of cytotoxic SO species, are still scarce.

On the above basis, the present work addressed the effect of Ti- and Li-doping of ZnO NPs on their structural and optical properties [16, 17]. Induced structural defects (e.g. interstitial and vacancies) were associated to those trap states required to generate SO species [16], which makes ZnO a promising candidate for PDT applications. The proposed research will be focused on the proof-of-concept related to the capability of pure and doped-ZnO as a direct PS, including preliminary study about the interaction of these nanoparticles under 2-photon excitation conditions.

1.2 Objectives

1.2.1 Main

- Determine the effect of doping of ZnO nanoparticles on their capability to generate cytotoxic species for potential biomedical applications.

1.2.2 Specifics

- Determine optimum conditions for the size-controlled synthesis of pure and doped ZnO NPs.
- Induce the enhancement of structural defects (e.g. interstitials Zinc or oxygen vacancies) to enhance the yield of SO generation.
- Confirm the enhanced generation of SO species in doped-ZnO NPs.

1.2.3 Thesis contents

In the first chapter of this thesis the motivation and objectives of the research work will be presented. Chapter II includes the review of the main concepts involved with the research, as well as the description of the action mechanisms in photodynamic therapy. In chapter III, the experimental methods to synthesize pure and ZnO NPs; including structural, morphological and optical characterization as well as the generation of ROS at different concentrations of dopant in the ZnO NPs, will be presented. Both chapters IV and V were focused on the discussion and interpretation of the results. Chapter V presents the most relevant conclusions form our work, whereas Chapter VI will show the list of consulted references.

2. Background

2.1. Nanotechnology and Cancer Nanomedicine

In the last years, the nanoscience knowledge has been on-the-rise due to breakthrough developments for health applications. Nanoscience studies materials at the nanometer scale (from 1nm until a few 100 nanometers), with the aim of building of new structures and devices with innovative properties that are different from the bulk (Figure 1). The application and understanding of the nanoscience, technology, and engineering is also known as nanotechnology. Nanotechnology enables the making and design of nanomaterials with different structures in nanoscale (nanostructures) that can be composed of noticeable components that show new and peculiar features [19].

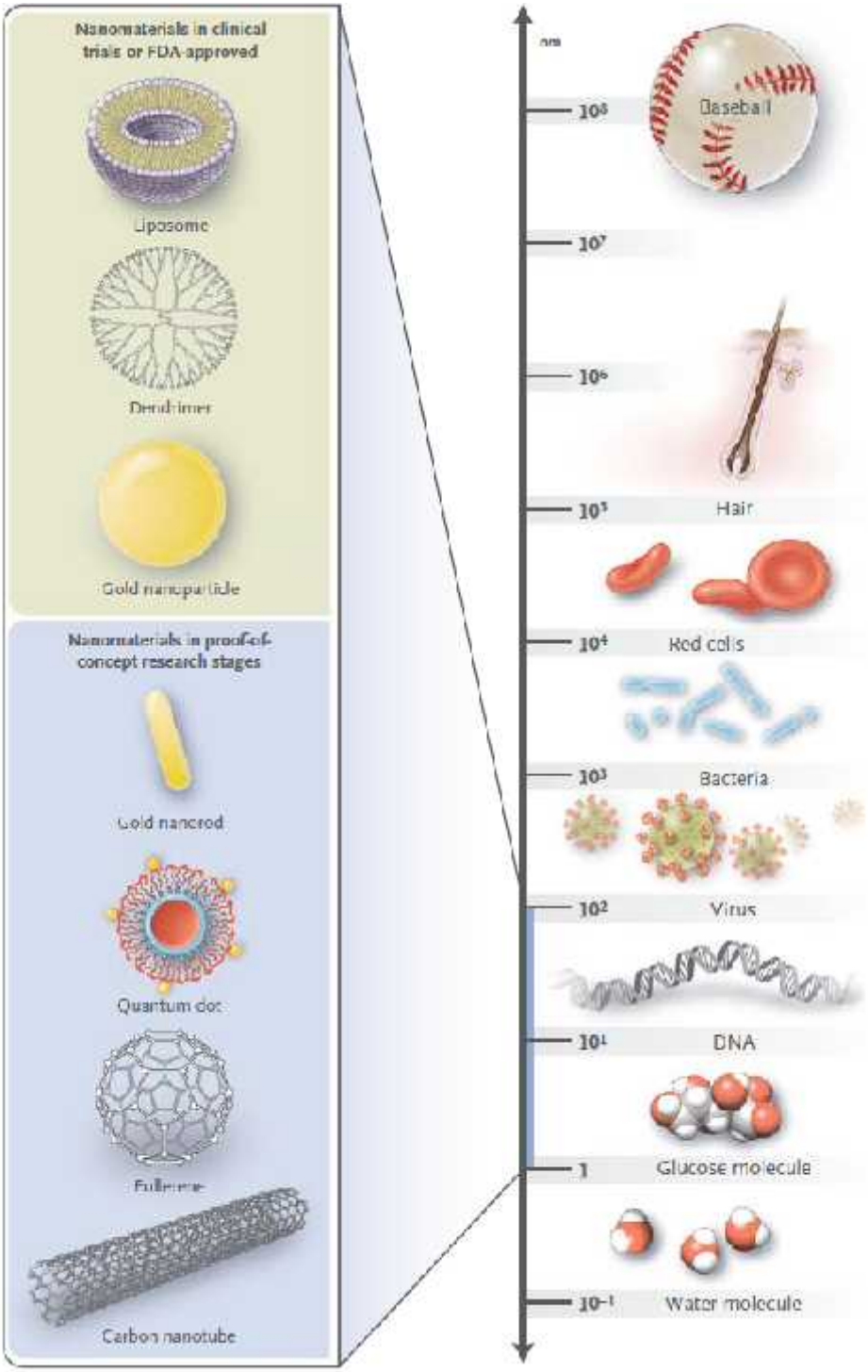

Figure 1. Nanomaterials approved by FDA and biological scale [20].

According to the number of confined dimensions in the nanometer range, the nanomaterials can be classified: a) Zero Dimensional, where all dimensions are at the

nanoscale and includes nanoparticles with different shapes; b) One-Dimensional, in which two dimensions are at nanoscale, for example: nanorods, nanowires, nanotubes; c) Two-Dimensional nanomaterials that only has one dimension in the nanoscale, for instance: nanofilms, nanolayers, nanoplates, nanodiscs, and nanoprisms. Figure 2 shows various schemes of nanomaterials according to their dimension confinement and Table 1 summarizes the corresponding features [22]. Depending on the dimensionality, composition, structure and functional features, current and novel nanomateriales will exhibit strong size-dependent functionalities that would enable their applications in the biomedical field. In the last decades, the advances in nanotechnology and nanoscience have opened new paths in medicine, raising a new yield: Nanomedicine. Nanomedicine has been seen like a great alternative in the production of new therapeutic agents to treat, diagnose and cure some diseases, using nanomaterials and devices such as particles, biosensors which can enhance human health. These nanomaterials have as minimum one dimension at the nanometer scale [21].

Cancer is well-known as the main cause of natural deaths in our society; this high mortality is due to the failure in detecting the disease at the early stages. Besides, cancer cells exhibit more resistance than healthy cells to applied therapies increasing their survival chances. For these reasons, a new and more suitable medicine, based on nanomaterials and nanotechnology, to face the cancer challenges becomes indispensable. Nanomaterials can overcome some disadvantages of traditional drugs and allow the tenability of their functional properties by controlling temperature, light, pH, magnetic or electric fields and stress. Different kinds of nanomaterials have been evaluated for biomedical applications including drug delivery and as theranostic agents (i.e. as therapeutic and diagnostic mean) in cancer therapy [19, 21].

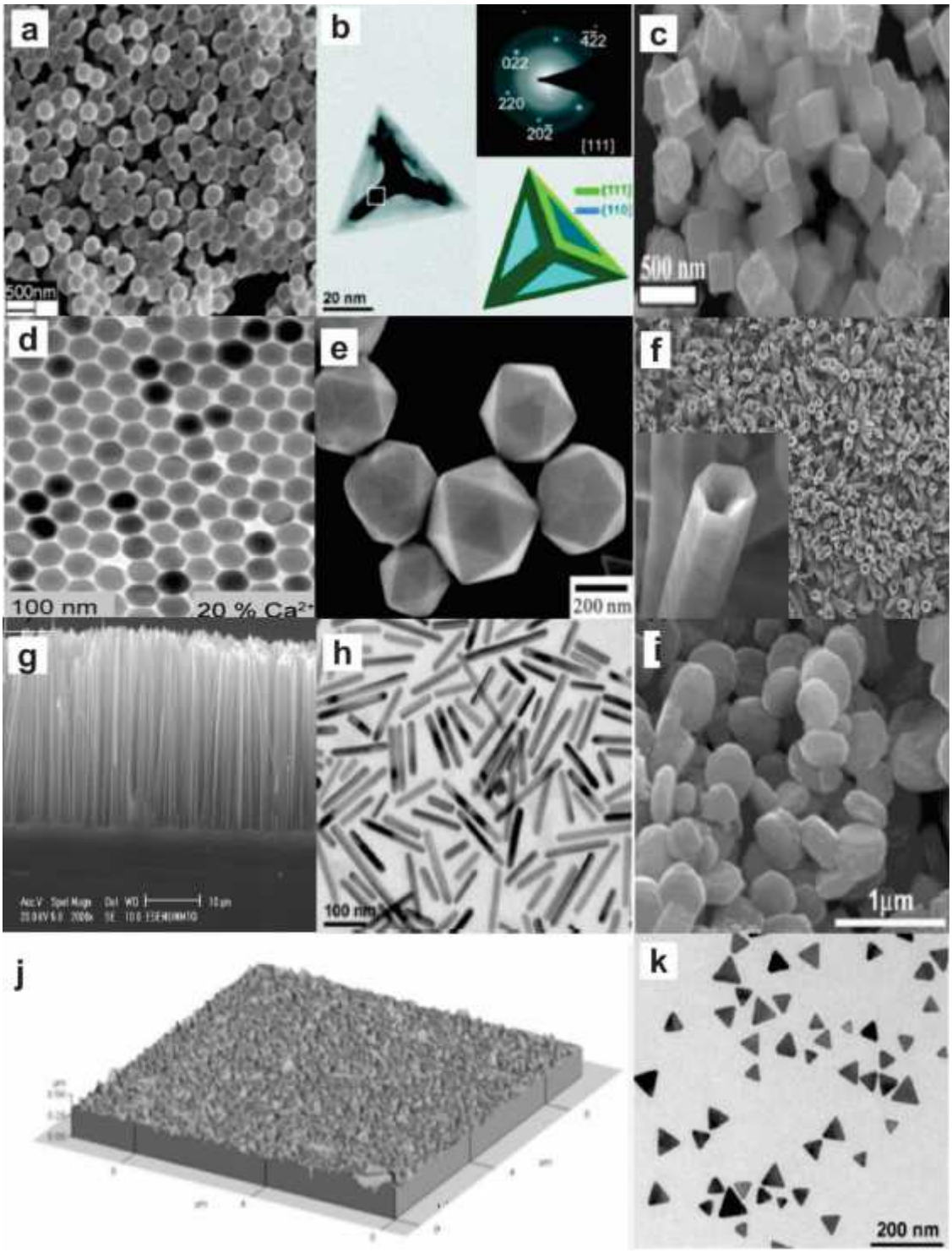

Figure 2. A collection of nanostructures synthesized by different methods: a) Nanospheres, b) Nanotetrahedrons, c) Nanocubes, d) Hexagonal nanoplatelets, e) Nanoicosahedral particles, f) Nanotubes, g) Nanowires, h) Nanorods, i) Nanodiscs, j) Thin Films, k) Triangular nanoplates [23-32].

Table 1. Nanomaterials features according to their dimensions [22]

Nanomaterials	Features
0-Dimensional	Crystalline or amorphous Single crystal or polycristalline Can show different shapes Can be inorganic or organic
1-Dimensional	Crystalline or amorphous Single crystal or polycristalline Chemically pure or impure Can be inorganic or organic
2-Dimensional	Crystalline or amorphous Mono- or multilayered surface Can be inorganic or organic

In turn, depending on their composition and structure, nanoparticles can be classified as: inorganic (metal, metal oxides, quantum dots, carbon nanotubes), and organic (liposomes, dendrimers, nanogels). Each nanoparticle classification exhibit different advantages and drawbacks; for instance, inorganic NPs can exhibit excellent magnetic, optical and electric properties and produce ROS, but only few are known to be used as drug delivery systems [20]. In addition, carbon nanotubes are being applied cancer treatment tests because to its excellent properties such as large surface area and also like a therapeutic agent in photo-thermal therapy [33].

2.2. Photodynamic Therapy (PDT)

Photodynamic Therapy (PDT) is one of the most promising cancer treatments due to its selectivity and less-invasive nature. Since 1999, the PDT has been approved by the Food and Drug Association (FDA) to treat pre-skin cancer. Nowadays PDT has been used for the treatment different cancer treatments like bladder, skin, head, neck, ovaries and some other diseases such as bacteria and also viruses [34-35]. However, the main targets in the PDT

approach are the cancer cell wall [36]. PDT consists of three important components: a photosensitizer, (PS), a light source with a specific length, and molecular oxygen.

The Photosensitizer (PS)

The use of a PS in PDT started in 1898 where Oscar Raab used a dye. He observed the toxic effect of Acridine dye on Paramecia cells, and noted that the effect was minimal in thunderstorm days in comparison to normal days. His conclusion was that the Acridine dye, through some mechanism, transformed the light into a kind of energy to destroy paramecia cells. In 1905, H. Tappeiner and his research group reported the first studies on the use of a PS like eosin, fluorescein, and sodium dichloroanthracene disulfonate in tumors and some skin diseases. The application of these dyes in the skin was topical, also in some cases intra-tumoral injections were conducted with positive results. Tappeiner´s results suggested that when the PS is incorporated into cells, ROS should be produced in presence of oxygen [37].

Photosensitizers (PSs) were developed mainly based on porphyrins. These PSs consist of aromatic molecules that show an effective production of excited triplet states by longer periods of time [38]. A PS is a fluorophore compound that can be concentrated at cancer cells, absorbs the energy from an external source and releases the energy at the surroundings cancer cells [39]. Several PSs are fluorescent, which helps in obtaining an optical imaging of organism to diagnose and detect the cancer cell present in the body of patient [40]. The properties of an ideal PS are [12]:

- Chemically stability.
- Low tendency to self-aggregation.
- No-toxic n absence of light
- No photo-bleaching.
- Target specificity in cancer cells.
- Easy and fast clearance by the body.
- No hydrophobic.
- High SO yield.
- Easy to synthesize.

However, none of PSs existent has ideal properties. Photofrin (Pho) is one of the first PSs approved for the treatment of many cancers. Besides, this compound has some drawbacks, principally its weak absorption intensity at wavelengths near infrared (NIR) region at 630 nm. The light at 630 nm can only penetrate the tissue at around 2-3 mm in depth which is convenient only to surface tumors. Other disadvantages exhibited by this PS are the long periods of time the human body takes to clean the residues of the PS (six to ten weeks). Despite of this drawback, Pho has te capacity to generated large amounts of SO species. At present, it is used to treat bladder, esophageal, lung and esophagus cancers [40, 41]. Porphyrin (Por) is another PS used for conventional cancer treatments. Por is eliminated faster from the body than Pho, but has low absorption intensity in the NIR at 648 nm [40-42]. Naphthalocyanine (Nap) is another PS that has the following advantages: penetrates the tissue two times more than Por in PDT, because it exhibits a high intensity of absorbance in the 750-900nm range; it has been reported its better photochemical and photophysical stability than Por. Por drawbacks is its complicated synthesis, low solubility in organic solvents, and poor hydrophilicity, which is an important factor for biomedical applications [42].

The aggregation of the PSs in a biological medium would reduce the production of ROS [41, 43]. Also, some PSs are amenable to photo-bleaching. Photo-bleaching is the drop in fluoroscence due to chemical harm induced by irradiation of laser after repeated excitation/emission cycles. It decreases the rate generation of SO [44, 45]. Another limitation of existent PSs is based on the poor generation of SO when the PS absorbs light of a wavelength representing low energy; the energy required by the PS to yield SO is 94 KJ mol^{-1} or 1270 nm [40]. Based on the precedent considerations, the production of new PSs with improved stability and efficiency to generate SO species sounds justified.

The Light source

The light provides the energy necessary to activate the PS toward high levels of energy to generate ROS. The kind of light to be used in PDT will be dependent on the profundity where the tumor resides. For example, the red light (620 -750 nm) penetrates 3 mm through the tissue, whereas orange (590-620 nm) and blue light (400-450 nm) penetrate 1.5 mm and less than 1mm, respectively [46]. It's obvious that the NIR light in

the 700-800 nm range penetrates the tissue deeper (5-6 mm) compared to visible light and the tissue can be repaired much faster avoiding any possibility of phototoxic harm. Also, the most intense peak in the optical absorbance spectrum of a PS would represent its optimal photo-activation wavelength [40, 47]. The majority of the PSs clinically approved for PDT absorb in the visible spectral region underneath 700 nm (Table 2). The appropriate wavelength to be chosen depends on the disease conditions.

Table 2. List of PSs and their typical maximum absorption band [47].

Class	**Photosensitizer for Photodynamic Therapy**	**Typical maximun absorption (nm)**
Porphyrins	Porfirmer Sodium	630
	Protoporphyrin IX (eg. For aminolevullinic acid)	633
Chlorins	Temoporfin(meta-tetrahydroxyphenylchlorin)	652
	Verteporfin(benzoporphyrin)	690
Phthalocyanines	Sulphonated aluminium phthalocyanine mixture	680
Phenothiazinium	Not yet approved	670
Texafrins	Not yet approved	734
Bacteriochlorins	Not yet approved	740

The Oxygen

The presence of molecular oxygen in tissues is important for the PS effectiveness since it is the source to generated cytotoxic ROS and SO species. SO could act either in the cell wall or inside the carcinogenic cell [49, 50].

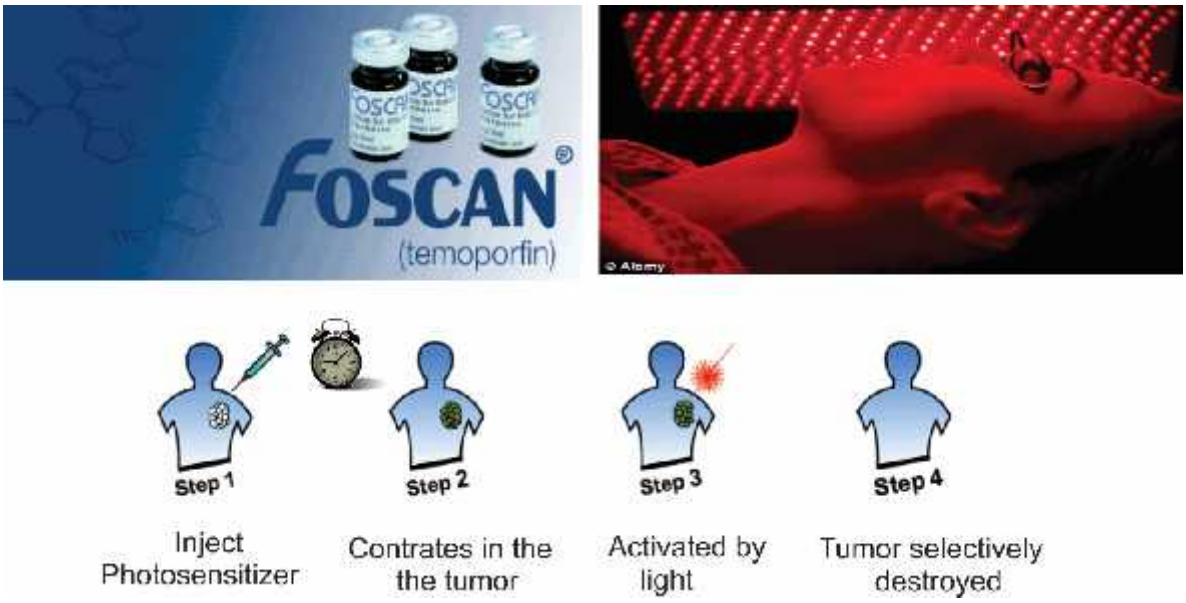

Figure3. The traditional PDT approach. *Foscan* is the commercially available FDA-approved PS [51-53]

The PS effectiveness to generate SO will obviously decrease in the treatment of cells that contain a low oxygenation or are deprived of oxygen (hypoxic cancer cells). This kind of cancer cells grow very fast, reach poorly vascularized zones and leave less concentration of oxygen, compared to healthy ones. However, the hyperbaric oxygen therapy is an alternative treatment that could improve the effect of PS under the described circumstances [49, 54]. The hyperbaric treatment consists in the administration of pure oxygen in a close chamber at pressures of 1.5- 3 atmospheres and through an oxygen mask the patient breathes the oxygen available. Then, the oxygen is absorbed by the blood and carried to the pathological sites [55, 56].

Figure4. Hyperbaric oxygen therapy [57]

2.3. Antimicrobial Photodynamic Therapy (APDT)

Others than cancer, several diseases are caused by microorganism or microbial pathogens such as: *Staphylococcus aureus*, *Escherichia coli*, among others. These microorganisms are resistant to certain antibiotics due to their fast growth and mutation to enhance their resistance to traditional antibiotics. APDT is based on the same basic concepts of PDT. The main benefits of this route are: minimal invasion, produces a few side effects, acts only in localized zone, avoid the microorganisms to start its regrowth after treatment, easy clearance from the body. As in PDT, APDT involves the presence of three components: PS agent, a light-external source with adequate wavelength, able to excite the PS, and oxygen. In short words, the PS is administered to the bacteria-intoxicated patient, followed by the light irradiation of the PS to generate ROS. Finally, the bacteria die and the PS is expulsed from the body [58]. Evaluated PSs have exhibited an effective action against Gram-negative bacteria; the reason is the relation with microbial cell which has a negative charge [59]. ROS induce oxidative stress in the bacteria wall to cause DNA and cytoplasmic membrane damage, which will finally cause the microorganism death [58]. The specific targets cells in PDT are mainly cell wall and membranes, including an

adequate adhesion between the PS and these biological structures [37]. According to previous studies with Escherichia *coli*, a PS such as tetra-*N*-methylpyridylporphyrin exhibited the capacity to generate SO in the internal and external zone of the cell [60]. The lifetime of SO in different biological medium are indicated in Table 3.

Table 3. Lifetime of SO in different medium [60].

Medium	**Lifetime of SO (μs)**
H_2O	3.5
D_2O	68
Lipids	50-100
Organics solvents	10-100
Inside cell	0.2

2.4. PDT Mechanisms

2.4.1 Biological Mechanism.

To trigger the PDT process, the patient should be diagnosed to detect the cancer cell or damaged tissue. The PS is administrated to the patient in different ways: intravenously, applied topically to skin, or via oral. The PS is distributed throughout all body and after a certain time (e.g. approximately between a time range of 4 - 6 hours for 5-aminolevulinic acid) the PS will be absorbed and will concentrate in major proportions in the cancer cell compared to the healthy tissues [49, 50, 61]. This is due for many factors:

(a) PS has more affinity to cells that present a quick cell division like cancer cells and its process of growth. Among one the many processes of cell division, mitosis is involved. Mitosis is the action of forming new cells or cell duplicates from a previous cell. Mitosis is essential for healthy cells but when a irregularity appears, cancer could be induced [60, 62].

(b) The PS is bonded to cell receptors containing high concentrations of low density lipoproteins, like in cancer cells [58].

(c) Cancer cells are characterized by an increased permeability, a retention capacity that would trap PS, macromolecules or proteins, which can be disseminates around the tumor. Healthy cells do not exhibit this behavior. [60, 63].

In absence of light, the PS is not toxic to cancer cell. Therefore, when the cancer cells or the damaged organism absorbed the PS, it is activated by external light source with an adequate wavelength and dose for a time period of around 8 min [61]. Then the PS absorbs the external light to start its activation, and interact with molecular oxygen to reach ROS generation, including SO, superoxide, and peroxide anions. Then ROS induces oxidative stress in the cancer cell promoting damage to lipids, nucleic acid, DNA and proteins as a result the cancer cell death [64]. Although several studies have reported SO as the main cytotoxic species in PDT, ROS could also contribute to destroy the cancer cell. Furthermore, in the majority of biological molecules the superoxide has a low activity and minimal oxidative capacity [60, 65]. The lifetime and the distance that the SO can diffuse in the cell are less than 3.5μs and 0.01-0.02μm, respectively. SO is highly reactive cytotoxic specie that can destroy the cancer cell from different pathways: apoptosis, necrosis and auto-phagocytosis without affecting the healthy tissues [66]. Also, a previous *in vitro* study of mice tumors evidenced that the PS Pho caused damage in the mitochondria that are characteristic of the apoptosis [67].

Additionally, the generation of superoxides and hydrogen peroxide in healthy cells is a normal process that occurs in the mitochondria and are needed to some biological reactions take place. The ROS generation control in normal cell is also important to maintain cell energy and avoid damage in the mitochondria. For this purpose, the presence of antioxidant enzymes is indispensable. In cancer cells, this phenomenon is similar; oxidative stress will be induced when the proportion level of ROS is larger than the anti-oxidant [68]. This scenario triggers different changes in the cancer cell: the proteins begin to oxidize, lipid peroxidation happens, DNA damages affecting nucleic acids. Alternatively, the cells try to repair the harm caused by ROS till their death [65]. Skin photo-sensitivity in the patient is a factor that must be overseen for a few days to weeks to assure the complete recovery of the patient [69].

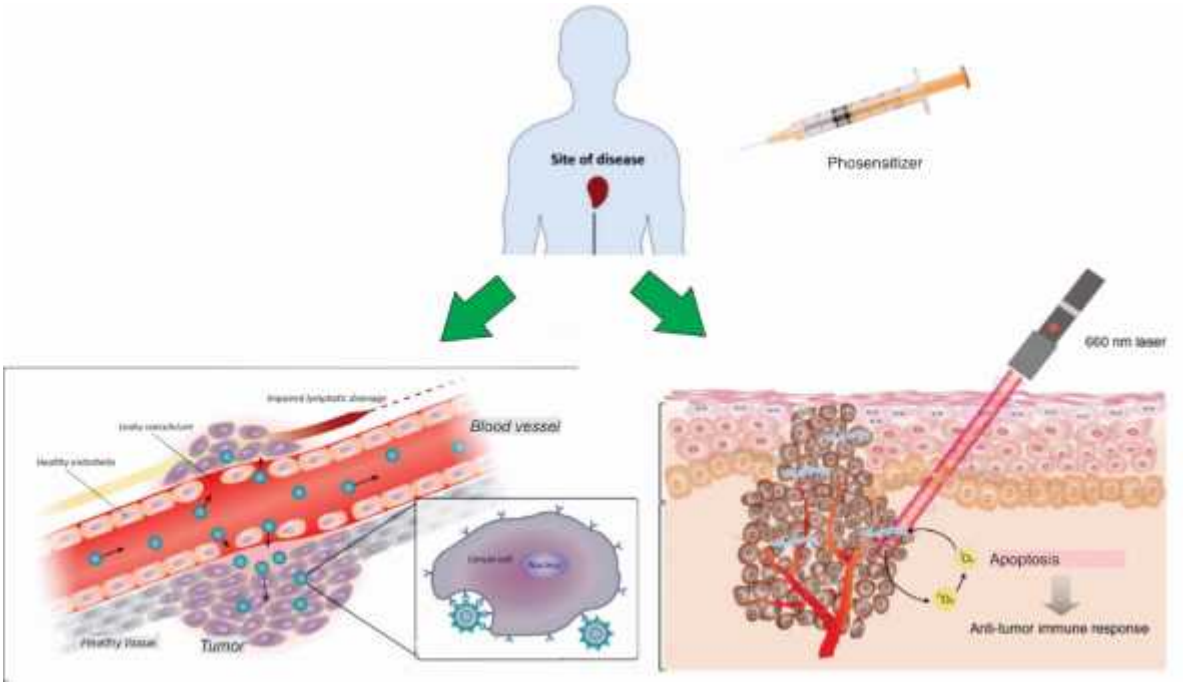

Figure 5. Schematic illustration of the biological mechanism of PDT after the injection of the PS [71, 72]

Lastly, the zone treated with PS should be protected from sunlight to the extent of using sun protection that do not have in particular physical, or inorganics filters (e.g. avobenzone) and apply for a time 48 hours after the applied treatment [70]. In the last years, PDT is broadened in other applications and recently focused on infectious conditions, bactericidal, and photo-aging [61].

2.4.2. Photo-physical and Photochemical Mechanisms

Photo-physical Mechanism

The Jablonsky's energy diagram represents those electronic energy levels that model the nature of the semiconductors. For an electron of a lower energy state (valence band) be promoted up to a high energy states (conduction band), an external source is necessary. In this case these energy levels are represented as triplet states (system where the total sum of all spins are zero) and singlet states (systems with parallel spins or total spin are different of zero) [41]. In energy terms, when PS is irradiated with a light source at

specific wavelength, the PS absorbs the energy of photons and gets excited from single ground state (S_0) towards some of the excited singlet states (S_n). Because the PS is unstable in its state, it is relaxed energetically in the following ways: non radiative, relaxation vibrational or heat. The typical time to reach the first excited singlet is in the order of 10^{-12}s [49]. In this excited state, the PS have two pathways; one way is that the PS could undergo a direct transition of returning to the ground single state losing energy either by emitting light (also known as fluorescence) or undergoes internal conversion by means of heat, nevertheless its time of transition to SO have a value of 10^{-9}s [37, 41, 73]. A second pathway is that the PS goes through an inter-systemic crossing, in other words a transition from the excited singlet state toward a triplet state through the spin inversion process of excited singlet state to obtain a parallel spin electron (triplet state), for this reason the change in electronic state involves that the life time in the triplet state should be upper from that of the singlet state to approximately 10^{-2}s. In the case of singlet state, this possess a total spin quantum number (S) equal to 0 (with a spin multiplicity equal to 1, according to equation of spin multiplicity (2S+1)), while compared to triplet state, it has a S=1 and 3 of spin multiplicity. However, these values are important for the magnetic spin quantum number (m_S). The values of m_S=±1, 0 corresponds to three sub-state of a triple state and m_S= 0 for singlet states [74]. At this stage, the PS achieves a new state that can interact with molecular oxygen and yield cytotoxic species or ROS that can cause cell harm [75].

Photochemical Mechanism

The key points for generation of ROS in PDT are photochemical reactions in the triplet state. The PS could return to singlet state losing energy. Possible processes to return the PS to a single state are by: light emitting which is known in terms of phosphorescence, non-radiative relaxation or also known as internal conversion. However, in presence of molecular oxygen, the PS can react by different pathways, defined as Type I and Type II. Type I implicates the reaction of PS with the solvent or cellular substrate. Type I is subdivided into two ways. In the Type I (a) reaction, the cellular substrate or solvent transferred one electron towards the PS, then the interaction between them produces a highly reactive radical such as superoxide anion. Additionally, this radical can undergo a reaction sequence with molecular oxygen to develop other ROS. Similarly, in the Type I (b)

reaction, the cellular substrate or solvent lose one hydrogen atom or proton and this last is trapped by the PS, so it can react rapidly and produce free radicals after it reacts with molecular oxygen through a series of reactions to finally produce ROS, even peroxides. Hence, the ROS generation could break the proteins, similarly the lipids, and so induce cellular damage to then destroy the cancer cell [40, 47, 76, 77]. In the type II pathway, the PS directly transfers its energy (photons) to the molecular oxygen and brings it to an excited level known as SO. The formation of SO involved the transition of the two excited singlet states of O_2 from the ground triplet state of $^3O_2$. The first form of SO ($^1\Sigma_g$) has a high energy due to its formation, which is obtained by inverting the spin of the electron at the electronic cloud's outermost layer, which violates Hun's rule. Then this form immediately loses energy and is converted in a more stable SO in which both electrons are paired in one of the orbitals [73]. Other important factor is the amount of energy applied from triplet state of PS to molecular oxygen, energy less than 94 KJ/mol or equivalent in wavelength and energy (1270 nm, 0.98 eV) cannot excite the molecular oxygen. Thus, a new oxygen highly reactive is formed only if the PS is in a triplet state and hosts enough energy to form SO. Few molecules exhibit triplet state like molecular oxygen and water (average percentage composition, hydrogen =11. 11% and oxygen = 88.89%). On the other hand, the lifetime of SO is short due to its reactivity. Table 3 summarizes the lifetime of SO in different media. In the case of the cell inner zone the PS lifetime is very short due to the highly reactive nature of SO in presence of biomolecules [40], furthermore another important feature is that it can penetrate the thickness of a cellular membrane until 20 nm [60]. At the end of the process, the PS returns to S_0; the cycles of absorption and emission can be repeated until the PS undergoes either photo-bleaching or degradation [75, 78].

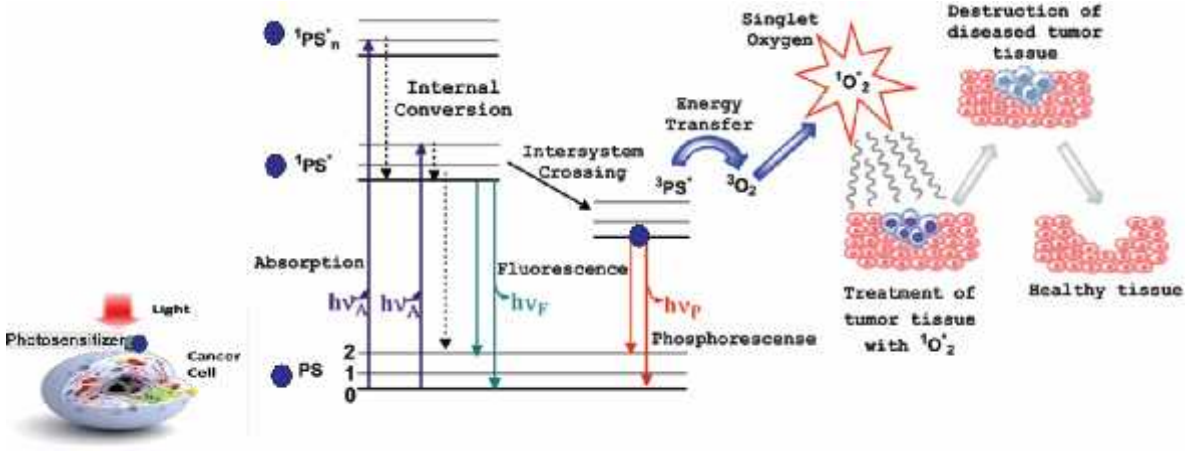

Figure6. Simplified Jablonski's energy diagram. In the presence of molecular oxygen in a triplet state ($^3PS^*$), the photosensitizer excited state ($^1PS^*$) transfers electrons or energy to molecular oxygen to yield SO species. [79]

2.5 Nanomaterials for biomedical applications

Nanoparticles in cancer treatment

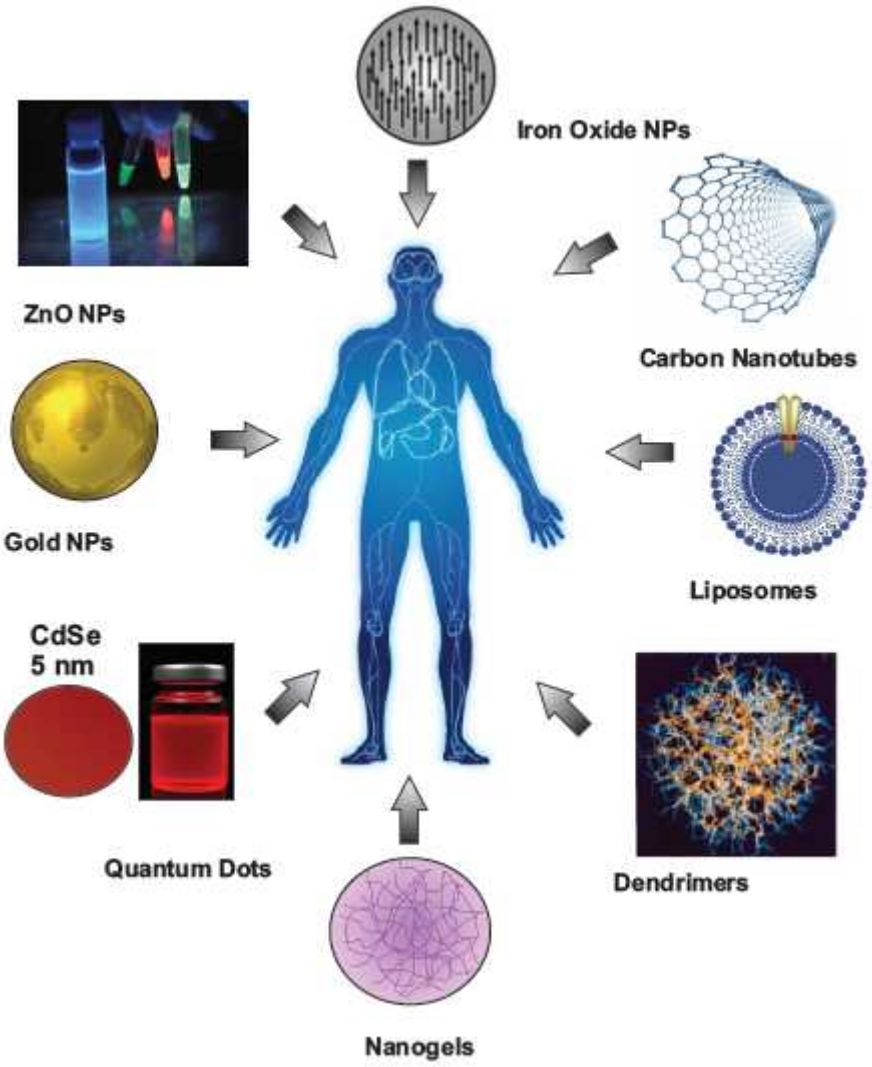

Figure 7. Nanoparticles and cancer treatment. [80-84]

Liposomes

Liposomes are spherical nanostructures with an approximate diameter of 100 nm and composed by a lipid bilayer in an aqueous medium. The liposomes are able of incorporating different types of molecules or drugs in its core. Equally important, each lipid bilayer contains a distinct fatty acid chain segment that permits to obtain specific physicochemical properties that are sensitive under some stimuli such as temperature, pH, enzymatic and mechanic release drug in the biological target. Some drugs hosted by liposomes are used in cancer treatments such as chemotherapy in the case to ovarian,

metastatic breast and Kaposi´s sarcoma with anthracyclines doxorubicin and daunorubicin, respectively [80, 81].

Dendrimers

Dendrimers are other kinds of hydrophilic NPs with a polymeric nature based in polyamidomine (PAMAM) and polyethylene glycol (PEG), with a size around of 1 to 100 nm. They exhibit a structure consisting of a hydrophobic core, which allows the incorporation of some type of hydrophobic drug, and many hydrophilic branches surrounding the core. The effectiveness of liposomes as a drug delivery in cancer treatment relies on their low polydispersity, high aqueous solubility, small toxicity, good biodegradation capacity and ability to carry drug. Dendrimers exhibits better mechanical stability than the liposomes due to covalent bond between the drug and the internal core of the dendrimer [82-84]. Some *in vitro* studies of PDT using dendrimers have been carried out; dendrimers modified with protoporphyrin, PAMAN and PEG have shown increased phototoxicity when compared to single protoporphyrin [83]. PAMAM dendrimers have reported limitations associated to the electrostatic interaction with blood components causing a minimum retention time and weak targeting effectiveness [84].

Nanogels

A hydrogel is represented as a hydrophilic network polymer in three dimensions that has the capacity of absorbing water and physiological liquid in high amounts but keeps their internal structure to encapsulate biomolecules for instance: drugs, DNA, and proteins. Nanoscale hydrogels, so-called nanogels, are receiving strong interest in the biomedical and nanomedicine field due to their high stability in biological environment. Nanogels have dimensions of less than 200 nm allowing an easier penetration than hydrogels. Nanogels present excellent features like low buoyant density, biodegradability and the more important feature, it can wrap either fragile compounds or heavy molecules due its hydrophilic properties. Moreover, presence of chemical or Van der Walls bonding are essential for the formation of the nanogels. In the last years, the modification on the surface of nanogels with pH-sensitive ligands have permitted the development of more selective nanogels for cancer cell, where the nanogel is not stable in organs with an adequate

physiological pH (> 7). This instability makes the bonds to break and thus, releasing the encapsulated drug to cancer cells while decreasing side effects to healthy ones [85-88].

Carbon Nanotubes

Carbon nanotubes are 2-dimensional nanomaterials that are composed by a hexagonal closely packed arrangement of carbon atoms to that form nanotubes with a single-wall or multi-wall of graphene in their structure. The carbon nanotubes lengths are in the range from nanometers to microns while the diameter is in nanometers. Additionally, carbon nanotubes display great physicochemical properties such as high mechanical strength (10 times more than steel), high electrical and thermal conductivity, ultralight weight, photoluminescence and large surface area as well as affinity towards some biomolecules such as nucleic acids and enzymes [1, 80]. The disadvantage is that it presents poor solubility in biological medium; under this circumstances are functionalized with distinct chemical groups to improve their efficiency [19]. Carbon nanotubes have been evaluated in image analysis *in vivo* and *in vitro* as a contrast agent in photo-acoustic therapy [1].

Gold Nanoparticles

Gold NPs have been applied as a drug delivery substrate in theranostic applications of some diseases such as Diabetes, Parkinson, cancer therapy, arthritis, cardiovascular illness and teeth implants due to its attractive physicochemical and optical properties, nontoxic, chemical inertness, and easy synthesis at moderate-cost [89]. Gold nanoparticles exhibit plasmon resonance that arises from their interaction with light. As a result of this interaction, electrons on the metal surface strongly oscillate at a certain resonant frequency with a characteristic wavelength and consequently, increases the scattering, which is showed as an intense absorption band [1, 90]. Illuminating gold NPs with visible light or NIR light source causes the surface electrons to oscillate achieving the electrons excitement and strongly resonates, then after the electrons return to its equilibrium state emitting energy in terms of heat. However, also, gold NPs have been used in photo-thermal therapy to destroy tumors through heat, the high temperatures transfer towards the tumors is the main mechanism to kill the tumor [91].

Silver NPs

Silver (Ag) NPs have attracted considerable interest due to their optical, chemical and bactericidal properties. In addition, Ag NPs also exhibits localized plasmon resonance with an adsorption band in the visible range that depends of different factors such as size, shape, inter-particle interactions and their dielectric constant [92]. Silver at small concentrations are relatively nontoxic to human cells but harmful for most of bacteria as well as viruses; this effect is attributed to the generation of ROS and free radicals destroying the bacterial membrane as a result of oxidative stress generation which leads to the deterioration of DNA and proteins [93]. Ag NPs are being applied in food storage, coating of medical catheters, textiles settings and in clothing for diabetic patients since the NPs promote the increment of capillaries at the wounded zone [80, 94, 95].

Quantum Dots (QDs)

QDs are semiconductor (SC) NPs with a size varying from 1 nm to 10 nm. These QDs can be composed by atoms from groups III and V (e.g. InP and InAs) or groups II and VI (e.g. CdTe and CdSe) of the periodic table. QDs are considered as a novel fluorescent nanomaterial due its excellent optical properties. They exhibit a broad band excitation in the visible range, narrow emission wavelength from the range near- ultraviolet (for example: ZnSe QDs) to NIR (for example: CdTe QDs). Quantum dots do not experiment photo-bleaching, are highly fluorescent, and also can emit light with different wavelengths according to their nanometric sizes. Compared with organic dyes or other commercials PSs used in PDT, QDs are more photo-stable and brighter allowing functionalization for biomedical applications due to their big surface area to volume ratio [96]. With these extraordinary properties, QDs combined with PSs such as Rose Bengal and Phthalocyanine have been frequently researched in PDT as cancer models *In Vitro* under one photon and two-photon excitation for the increase of SO production [97]. Others applications of QDs include fluorophores, direct PSs, cellular imaging [80, 94, 97, 98]. Although this may be possible, certain materials used in the production of QDs such as Cadmium have an intrinsic toxicity and show inadequate bio-degradability [80, 98, 99].

Magnetic NPs

Nowadays, magnetic NPs are quite studied due to their easy mobility to specific sites within of the organism. Magnetic NPs exhibited unusual features such as large superficial area, biocompatibility, stable in physiological conditions (pH= 7) and tunable magnetic properties due to high magnetic susceptibility [100]. Under a magnetic field, the electron spins within a NP achieved to align with the field applied creating a magnetic dipole or magnetic moment, where the total sum of each particle with a single domain magnet reached the maximum value of magnetization known as saturation magnetization, thereupon the NPs are aligned in the same direction of the magnetic field applied. However, if the external magnetic field is removed the NPs returns to their nonmagnetic state. These peculiar behavior of magnetic NPs enable them to be used in living systems [101]. Nowadays, magnetic NPs are used in biomedicine, e.g. contrast agent in MRI for cancer cells detection, separation of cells, drug delivery, and hyperthermia for cancer treatment against prostate and glioblastoma brain cancer, among others. The hyperthermia treatment consists in the intravenously injection of magnetic NPs that are heated afterwards under the action of an Alternating Magnetic Fields (AMF, i.e. the capacity to periodically change directions between parallel and antiparallel) in form of electromagnetic waves with adequate intensity (between the range of radio-frequency to near infrared). During this process the temperature in the pathological region is increased approximately 40-45 °C destroying the malignant cells or inhibit their growth [19, 102-104]. However, this treatment produces some few side effects like burns, or pain in the tissue [104]. **Figure 8** shows the mechanism of hyperthermia therapy.

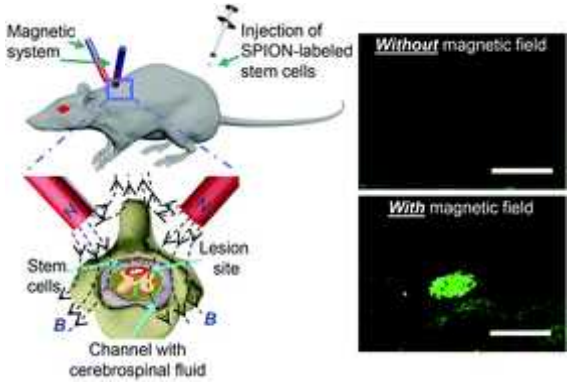

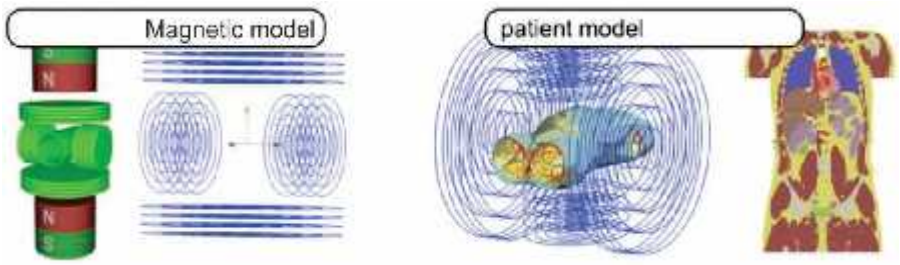

Figure 8. Hyperthermia treatment using magnetic nanoparticles to generate heat by induction [105, 106].

Besides, few magnetic NPs have been approved by the FDA and EMA (European Medicine Agency). One of these is Iron Oxide due to their good magnetic properties and minimal intrinsic toxicity according to *in vivo* and *in vitro* tests. On the contrary, Magnetic NPs like FePt, cobalt and nickel exhibit uppermost magnetic response and high saturation magnetization but this drawback is they are considered toxic [107].

Titanium Dioxide NPs

Titanium dioxide (TiO_2) is considered a photocatalytic semiconductor with a band gap around 3.2 eV. It is stable, inexpensive, capable to generate ROS and has been approved as a non-toxic material. TiO_2 NPs are used commercially in sunscreens, pharmaceutical, cosmetics due to their transparency and capacity to absorb ultraviolet light. It is also used in wastewater treatment and construction materials like cement to clean and remove of organic pollutants using ultraviolet light. When TiO_2 is exposed to ultraviolet light with a similar energy as its band gap, its electrons can be moved from the valence band (VB) to the conduction band (CB). Consequently, the positive holes react with water and the electrons react with molecular oxygen to produce hydroxyl radicals and superoxide radicals, respectively [107-110]. For these reasons, TiO_2 can find promising applications as antibacterial, antifungal material and a source of ROS for cancer treatment. *In vivo* testing of TiO_2 NPs has suggested their accumulation in peripheral lymphoid organs and affecting immune cells due to effect ROS cytotoxic effect and therefore causes oxidative stress conducive to cellular damage [94].

ZnO

ZnO is considered as a safe material and is approved by the US FDA. It is used in products like sunscreen, cosmetic products, clothes, lotions, piezoelectric and optoelectronic devices, antifungal (for instance: fungicides in agriculture) and as anti-bactericidal agent [111-114]. Moreover, Zinc is considered an indispensable mineral for human health [115]. ZnO is being further investigated due to its low cost, biocompatibility, biodegradable, high photo-stability, chemical and thermal stability, capacity to absorb ultraviolet (UV) light and to produce cytotoxic ROS, and photo-oxidative ability towards chemical and biological [16, 17, 114, 115]. In addition, ZnO NPs show low toxicity in human cells but high toxicity to pathogens or bacteria [116, 117].

Certain semiconductor nanomaterials are considered good candidates as direct PSs for PDT due to their excellent optical properties and photo-toxic effect in aqueous medium [118]. Similarly, ZnO have been investigated as a promising material for cancer treatment and imaging diagnosis opening new expectations in biomedicine applications [119-121]. Previous cytotoxic studies *in vitro* of ZnO NPs against MCF-7 (one type of breast cancer cell), and HepG2 (cells associated with carcinoma cancer) cells as well as different bacteria indicated that ZnO NPs inhibit the growth of the bacteria's due to the NPs small size compared with the microorganism; the NPs can adhere to surface membrane of the microorganism and enter to the inner microorganism to attack and destroy the bacteria due to NPs oxidative stress induction. Similar effect was observed in evaluated cancer cells, where the NPs promote ROS to decrease the cell proliferation and death cancer cells by apoptosis. The production of ROS is an important factor for the toxicity of ZnO NPs [111].

Similarly, the same apoptosis effect was observed *in vitro* for different cells lines, including glioma cells (is a type of brain tumor), breast cancer, prostate cancer and their respective normal cells lines; cytotoxic effect in cancer cells were observed due to an increase in ROS generation caused by ZnO NPs (with diameter around 60nm) while in normal cell lines it was not observed, suggesting the selectivity of ZnO NPs as cytotoxic agent towards the treatment of cancer cells [121]. The difference between cancer cells and healthy cells is that cancer cells have small pores of approximately 20μm. Then the NPs stay either in the cellular surface or break through the cellular membrane due to chemical

stability and high surface area of NPs, consequently it interacts with the biological medium to produce ROS damage the mitochondria, protein, enzyme, endoplasmic reticulum (it organelle is important to protein assembly, biosynthesis of lipid and cell survival) and DNA, therefore it destroys the cancer cell by apoptotic responses [17, 76, 122].

In other *in vitro* studies, ZnO nanorods were activated with UV light for 3 min in presence of hepatocarcinoma and human lens epithelial (HLECs) cells; the cell viability tests revealed the drop in cell viability by promoting the yield of ROS [120]. Irradiation by sunlight may cause some eye disease due to the exposure to UV-B (in the range 290-320nm), in which the UV light provokes the abnormal growth of HLECs and induce the formation of cataracts. ZnO NPs at high concentrations in presence of UV light inhibited the growth of HLECs due to high production of ROS and subsequent damage to the cellular membrane, DNA and proteins of HLCEs [123].

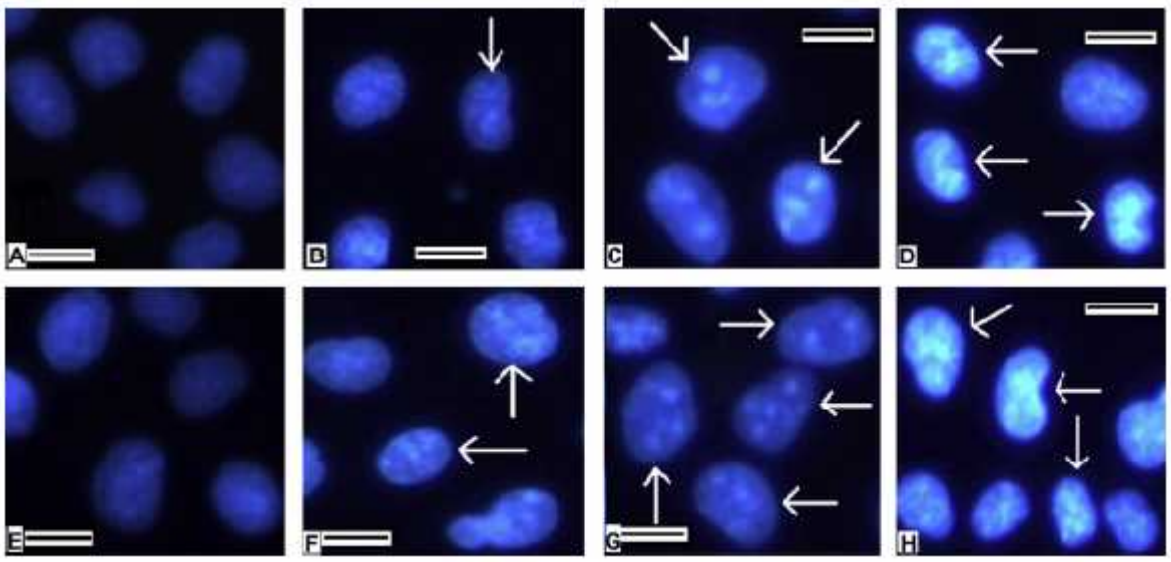

Figure 9. Morphological changes in the HLCEs, at different concentrations of ZnO NPs in presence and in absence of UV light. (a) Untreated cells, (b-d) cells treated of less at high concentration of ZnO NPs in absent of light, (e) cell after UV irradiation, (f-h) cells treated of less at high concentration of ZnO NPs in presence of UV light. Figures reproduced from [123].

ZnO NPs also have been studied in combination with certain anticancer drugs, e.g. doxorubicin, to improve the yield ROS against *E.Coli* and *HeLa Cells* (cells related with

cervical cancer) under ultraviolet light irradiation. Doxorubicin on the surface ZnO NPs in presence of ultraviolet light generated more oxidative stress, SO, and DNA damage than in the dark. As a result, it increases the efficiency as a therapeutic agent [124].

Regarding the use of ZnO against bacteria, *Escherichia Coli* is one of the most investigated. This bacterium is located in the gastrointestinal tract; some strains of these bacteria play an important role in health; however, other strains, such as *E.Coli* O157:H7, can cause dangerous diseases related to diarrhea, kidney failure, and urinary tract infections due to the production high toxins [125]. This pathogen E. Coli O157:H7 can be found in humans or animal feces, food contaminated with feces, and foods washed inappropriately. Additionally, ZnO NPs were applied on *E.Coli* O157:H7 in absence of light, in which ZnO NPs showed intrinsic toxicity towards the bacteria due to its attraction mechanisms and generation of ROS [126]. Also, a similar effect was observed when ZnO NPs were evaluated in the same previous bacteria in presence of visible light (400nm). Moreover, it was indicated that the ZnO NPs without irradiation are less toxic. The physical damage of the bacteria membrane by ZnO nanoparticle, has also been reported, [127].

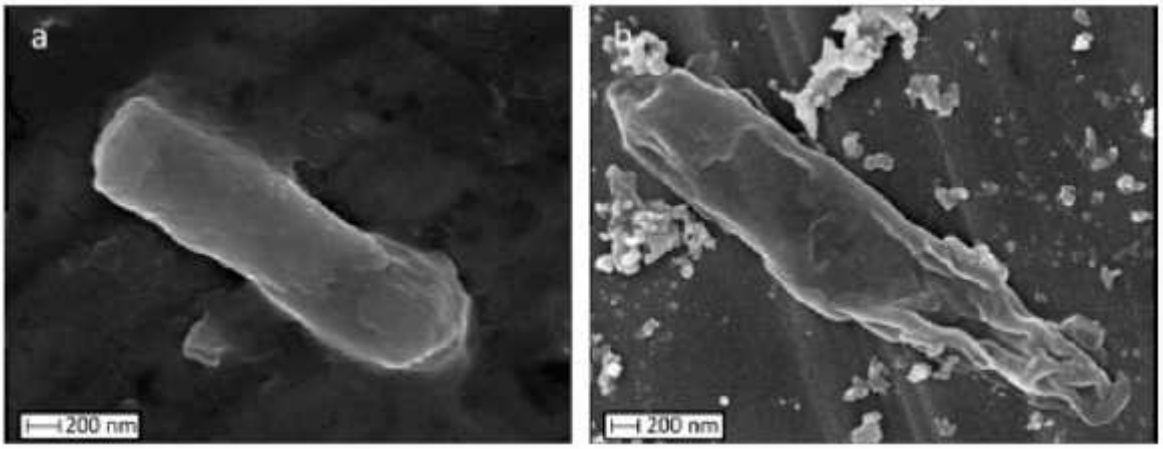

Figure 10.SEM images of *E.Coli*. (a) Bacteria alone, (b) ZnO NPs photo-activated at 400 nm and contacted for one hour with *E. Coli*. Figure (b) reveals the contraction and membrane damage of the bacteria. Images reproduced from reference [127].

The selective *in vitro* cytotoxicity of ZnO NPS towards cancer and bacterial cells is one of the advantages in biomedical applications and can be attributed to electrostatic interactions between the NPs surface and the cell membrane. Generally speaking, positively

charged ZnO NPs surface will favor the electrostatic interaction with negatively charged cancer cells. In physiological medium, i.e. aqueous medium with pH higher than 7, healthy cells exhibit a net positive charge that explains their electrostatic repulsion with ZnO NPs. On the other hand, the external membrane of cancer cells hosts large amounts of anionic phospholipids, which induce the development of a net negative surface charge. Accordingly, the attractive interactions between ZnO NPs and unhealthy cells will favor the NPS uptake by cancer cells [126-128].

Another key point related to the use of nanoparticles in biomedical applications is their size. NPS with sizes of less than 200 nm are able of penetrate above biological barriers and achieve an interaction with the cancer cells or microorganism inside or on its surface [81]. After administration of the NPs in the body, subsequently the NPs can pass by vascular endothelium through blood Bessel to then penetrate the damaged tissues and tumors because of its enhanced permeability in the tumor, and finally renal excretion is released from target tissues. Nevertheless, experimental proof shows that the QDs (NPs less than 10 nm) can pass quickly by the vascular endothelium, but can return outflow into the blood and be quickly cleared by the kidney, and thus decreasing their cytotoxicity toward cancer cells. On the contrary, NPs in the range between 100-200 nm have improve opportunity to accumulate in cancerous tissues due to it avoids leak into tumor interstitium across passive targeting mechanism [33, 129]. Meanwhile, in the body also exists cells that protects the organism and have the capability of ingesting strange particles specifically larger NPs than 200 nm in diameter and can be captured by the macrophages to finish in the liver and then scavenge NPs with this size, which not permit the cellular uptake of the NPs [130, 131].

The main limitation to use metal oxides NPs (TiO_2 and ZnO) in medicine is their photo-catalytic activity under UV light to generate diverse kind of ROS (hydrogen peroxide, superoxide, and singlet oxygen) [119]. The use of UV light represents a serious limitation to the clinical use of these nanoparticles in PDT. This is due to the poor penetration, and the promotion of irritability towards tissues. The alternative to open actual application in the biomedical field relies on the capability of exciting ZnO-based nanomaterials using 2-photon excitation approach [132-134].

2.6. Two-Photon Excitation Photodynamic Therapy (TP-PDT)

Although PDT has been approved clinically and shows less side effects compared with other therapies, it still shows some disadvantages such as the damage to adjacent tissues in the treated area [135] and limited penetration [136]. The two-photon excitation of PS can overcome these drawbacks.

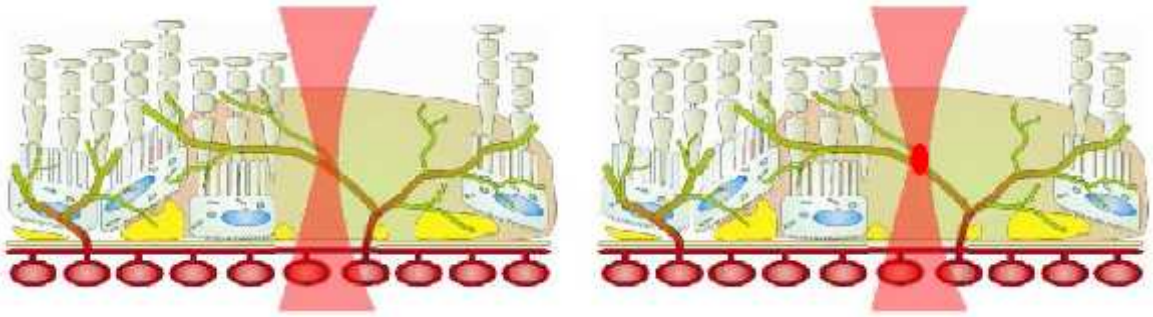

Figure 11. Schematic representations of PDT (left) and TP-PDT (right) in the retinal neovasculature. In TP-PDT the activation of a PS occurs only at the laser beam focus, while the PDT acts all over the path of the laser beam; therefore, this TP-PDT could cause fewer side effects. [137]

TP-PDT is a new technique developed in the last years and makes use of NIR light (690-1000 nm) to excite the PS and produce ROS [138]. TP-PDT consists in the simultaneous absorption of two photons with twice the wavelength, or half energy, of one photon excitation by the PS to reach excitation into high energy states and produce ROS. To achieve an effective simultaneous absorption, it is required that the light pulse must be less than 100 fs. The first photon excites the PS from a low energy state (i.e. VB or also ground single state) to a virtual intermediate excited state that is within the band gap. Simultaneously, a second photon provides energy to the PS in this virtual state and promotes the transition to a high energy state (i.e. CB or also excite single state) [139, 140].

The two-photon absorption is a nonlinear process; moreover, the probability that this event occurs simultaneously is very small in comparison with one-photon absorption implying that its probability is proportional to the square of the light excitation beam

intensity. Therefore, the experimental measurement of this two photon excitation is very complex. The Two-Photon Excited Fluorescence (TPEF) is based on the simultaneous absorption of two photons with lower energy or large wavelength to emit light. The benefits of two-photon absorption are that it uses a focused ultra-short laser beam and act only in small zones at the focal point of the laser, and also the longer excitation wavelength diminishes the scattering enabling better tissue penetration. Second Harmonic Generation (SHG) is other non-linear optical process similar to two-photon absorption, in which two photons within of a small virtual lifetime and both at same frequency interacts with non-linear material to lead to virtual states and generate new photons with twice the frequency (or twice the energy or half the wavelength) of the initial photons, instead of making an energy transition from band to band (fluorescence process). Additionally, SGH mainly depends of the material crystalline structure and only occurs in materials with non-centrosymmetric structures [141]. Accordingly, a non-centrosymmetric material at some wavelengths can present SGH [142]. In addition, the external source that excites the PS in the TP-PDT is a pulsed laser, which permits focused excitation in small zones.

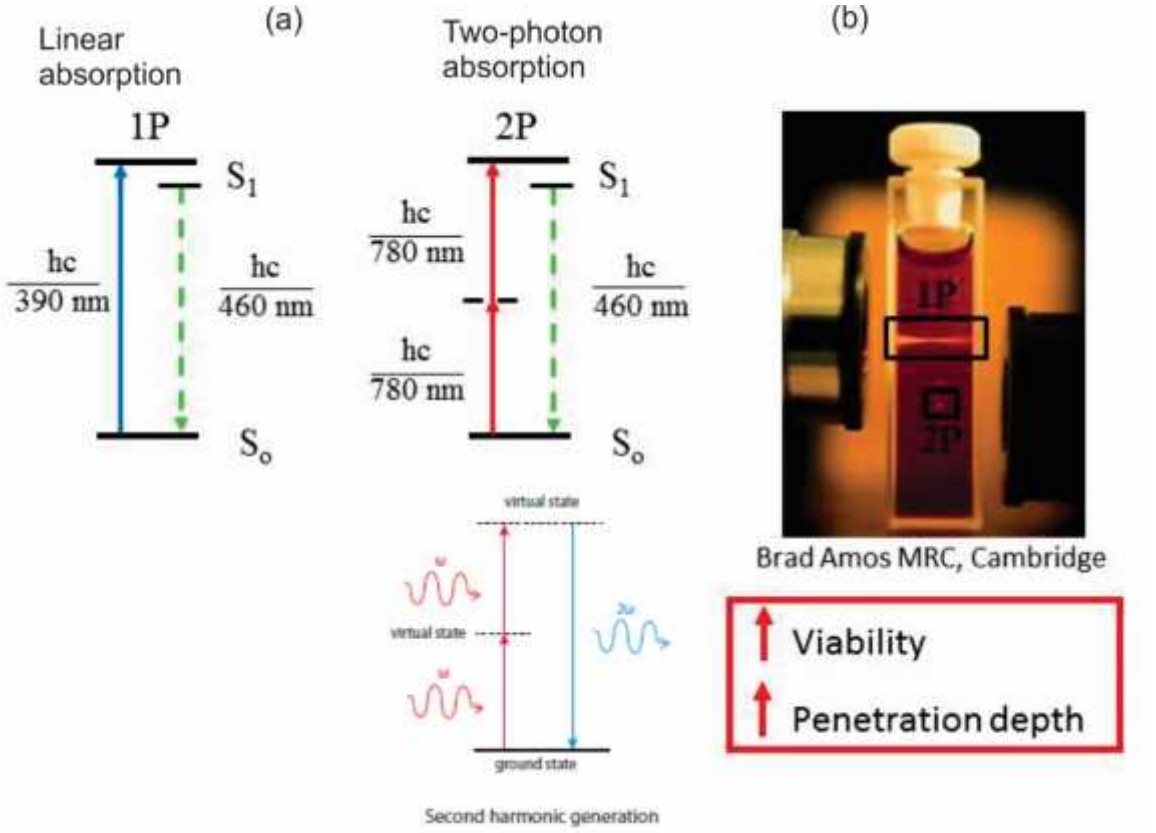

Figure 12. (a) Simplified scheme of one and two photon absorption and second harmonic generation, and the presence of virtual state for simultaneous excitation of second photon. (b) Activation of PS in a confined volume using two-photons [143].

Furthermore, ZnO is widely known due to its lineal optical properties because of it has a wide band gap, which is excellent to applications with short wavelengths. Whereas, non-linear properties of ZnO, until the moment are little to known [144]. For instance, ZnO crystals and specifically thin films display non-linear optical properties, allowing considerations such as an important PS and a good material for non-linear optical devices [145]. In a previous report by Sreeja´s group, they synthesized ZnO NPs by wet chemical method at different sizes and they found that the coefficient of two-photon absorption increased with respect to particle size increment. The corresponding results are summarized in Table **5** [146].

Table 5. Effect of the particle size in the coefficient of two-photon absorption and band gap of ZnO NPs at different NaOH concentrations [146].

Particle size (nm)	Band gap (eV)	Concentration of ZnO (M)	β (cm/GW)
2.79	3.72	0.141	21.1
2.89	3.7	0.133	109.3
3.17	3.65	0.131	210.7
3.37	3.62	0.118	448.5
3.61	3.59	0.116	475.8
3.81	3.56	0.081	567
6.83	3.43	0.051	622
10.25	3.41	0.038	682

Besides, S. Abed *et al* synthesized ZnO doped with Ni thin films to evaluate the electrical and non-linear optical properties, in particular SGH. In this report, they suggested the increment of the free carriers' concentration and its conductivity in the thin films which was due to the presence of defects, mainly V_O or Zn_i (zinc atoms in an interstitial site on the lattice). On the contrary, Ni-doped thin films exhibited a decrease in the conductivity [147].

NPs SC like ZnO-based nanostructures are considered a promising material for diagnosis and cancer treatment, due to their fluorescence and the capacity to generate ROS. Another excellent reason is that ZnO-based nanostructures have discrete energy levels in the same way that organic fluorophores have, in a range 1-5 eV [148]. In turn, Lithium (Li) is used in medicine for bipolar treatment disorder and is not toxic if used in appropriate amounts; the level of Li in serum (blood) should not exceed 11.1 mg/L Li. Also TiO2 has been approved by FDA as a safe material thus their Ti^{4+} ions are not toxic [145]. Li^+ has an ionic radius of 0.60 Å, which is smaller than Zn^{2+} (0.74 Å), therefore this would facilitate its incorporation into the ZnO host lattice. This incorporation would also be conducive to the increase of the photoluminescence intensity when compared to un-doped ZnO [148].

2.7. Materials Properties

ZnO

Between the different semiconductor (SC) materials, ZnO is an excellent example due to its direct wide band gap (3.3 eV at room temperature) in the UV region. ZnO shows intrinsic defects such as interstitial zinc (Zn_i) and oxygen vacancies (V_0), and also exhibits a large exciton binding energy (60 meV) at room temperature that allows the excitonic emission, responsible for its diverse applications such as optoelectronic applications in devices in the UV and blue region of the electromagnetic spectrum such as semiconducting laser, light-emitting diodes (LEDs) and piezoelectric devices [149]. The presence of defects in ZnO nanostructures depends of the synthesis method. Additionally, ZnO possess a hexagonal crystalline structure, non-symmetric that is stable at room temperature known as wurtzite structure. Because of this structure, ZnO has good nonlinear optical properties, achieving excited materials based in ZnO with multi photon at larger wavelengths [141]. On the other hand, ZnO have the following properties: is a non-toxic material, biodegradable, exhibits a high thermal conductivity, chemical and thermal stability, luminescent at ambient and high temperatures, its biocompatible and can react with water for the production of free radicals under the activation of the light at certain wavelengths [150]. ZnO can absorb visible light (UV) which is used in lotions and confirms the fact that is biocompatible with the human body. Hence, many investigations have been developed to study the luminescence of nanoparticles as a light source for cancer therapy. This kind of treatments needs the illumination of NIR light to reduce the toxicity of the surrounding healthy tissues. Therefore, they focus on the development of photosensitizers and nanoparticles to reach an optimize production of free radicals over the absorption of NIR light [151]. These features are important to design and develop optoelectronic devices and nanomaterials for cancer treatment based on ZnO nanomaterials.

Table 4. Physical and chemical properties of wurtzite ZnO [152-154]

Molecular weight	81.37 g/mol
Appearance	White or milky
Melting point	1975 °C
Stable crystal structure at 300 K	Wurtzite
Lattice parameters at 300 K	
a	3.2495 Å
c	5.2069 Å
Band gap at room temperature	3.370 e V
Band gap at 4 k	3.437 e V
Exciton binding energy	60 meV
Thermal conductivity	0.6, 1-1.2 $Wcm^{-1}°C^{-1}$
Density	5.606 g/cm^3
Static dielectric constant	8.656

GENERAL PROPERTIES

Crystal Structure

ZnO is one of the most important inorganic binary compounds that belong to the group II-VI of the periodic table in semiconductors (SCs) materials. ZnO crystallizes in three different crystalline structures: cubic rocksalt, cubic zinc blende and hexagonal wurtzite. In the structure rocksalt, each cation (O^{2-} ion) is surrounded to six anions (Zn^{2+} ions) at the vertices of an octahedron. In contrast, the structures of Hexagonal wurtzite and cubic zinc blende, each anion (Zn^{2+} ion) is surrounded by four cations (O^{2-} ions) and in the same way each anion is interconnected by four anions at the corners of a tetrahedron. Despite that its tetrahedral arrangement of atoms covalent bonding with sp^3 hybridization is characteristic, and also the Zn-O bonds show ionic behavior. This is due to electronegative difference between Zn and O (to Zn is 1.65 and to O is 3.44), moreover according to the scale of Philips ZnO have an ionic factor of 0.616 [155]. However, ZnO is known to have iconicity in the frontier between covalent and ionic character [156]. These three crystalline

structures of ZnO are represented in the **Figure 13**. Under the thermodynamic stability criteria in the ZnO structure, both structures cubic zinc blende and cubic rocksalt are metastable, whereas the wurtzite structure is thermodynamically stable at ambient temperature [156]

Wurzite ZnO structure possess a hexagonal unit cell, and two lattice parameters ¨a¨ (3.2 Å) and ¨c¨(5.2 Å) for the ideal wurtzite structure, with an space group C_{6V}^{4} according to Schoenflies' notation. This structure can be described as two sub-lattices of hexagonal closed-packed (HCP) O^{2-} ions and HCP Zn^{2+} ions interconnected [157]. The structure of ZnO wurtzite is constituted basically by alternating planes that contains Zn^{+2} and O^{-2} ions and are stacked following the packing sequence AaBbAaBb along the c –axis. In particular, ZnO wurtzite possess a tetrahedral coordination (where each cation is surrounded by four anions, and vice versa). This tetrahedral coordination results in a non-central symmetry structure with polar alternating ions planes located in the top and bottom base of the lattice with opposite charges and where the Zn ions are in the basal plane (001) and the O ions are in the basal plane (00-1). Under the effect of an external pressure, the center of the negative and positive charges can be displaced inducing distortion in the lattice. This displacement produces a local dipolar moment and finally creates a macroscopy dipolar moment and a polarity in these surfaces over all the crystal. These also produce a spontaneous polarization along the c-axis. Therefore, the lack of central symmetry in wurtzite ZnO structure and the described polarization are attractive to the application of ZnO in piezoelectric devices and sensors [145, 156, 158]. Others non-polar planes commonly observed in the ZnO lattice such as (110) and (100), are less energetic than the (001) plane [153].

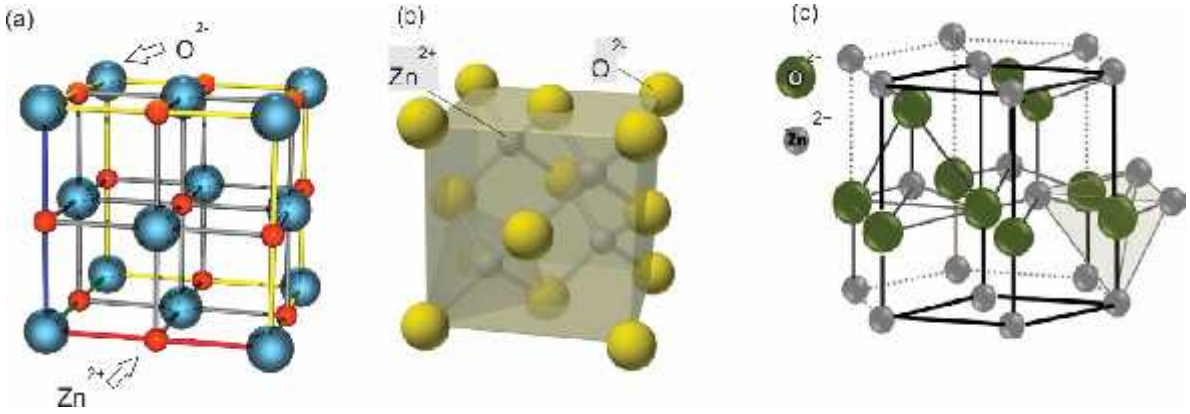

Figure 13. Representation of ZnO crystal structures. (a) cubic rocksalt, (b) cubic zinc blende, (c) hexagonal wurtzite [159-161]

Lattice Parameters

The precise values of the lattice parameters in ZnO have been investigated for a long time. These parameters usually can be affected by the following factors [156].

a.) Free- electron concentration that causes the increment in the lattice parameters due to the deformation potential of the conduction band minimum occupied by these free electrons.

b.) Concentration of strange atoms and the incorporation of defects: the difference of ionic radius between the impurity and the substituted ion can also promote the cell expansion, and hence the increment of the lattice constants. Both point defects (e.g. zinc anti-sites and oxygen vacancies) and linear defects (e.g. threading dislocations) can modify the lattice parameters. Zinc anti-sites are another type of defect that occurs when Zn^{2+} ions exchange position with some kind of anion.

c.) Induced strains, as those generated when the ZnO is deposited onto a substrate.

d.) Temperature.

Based on the above consideration, it can be understood the variation in the lattice parameters reported in the literature: from 3.2475 Å to 3.2501 Å for ¨a¨ parameter and 5.2042 Å to 5.2075 Å for ¨c¨. Therefore, the c/a ratio is affected by slightly varying from 1.593 to 1.6035; this change of value in the ratio is due to ionicity and lattice stability [156].

Electronic Band Structure

ZnO exhibits a direct and large band gap estimated at 3.37 eV at room temperature. The band gap is the necessary energy to move an electron from the valence band (VB) to conduction band (CB) and this located between VB and CB. However, in the semiconductors exists a theory that describes the energy of these electrons known as band structures [157]. A direct-band gap semiconductor obeys two main principles: 1) the conservation of energy, i.e. the difference of energy between CB (final state) and VB (initial state), should be identical for incident energy produced by the photons; 2) The conservation of momentum, that implicate that the difference of both states (final and initial) must be identical to the momentum of the incident light [156].

These principles can be expressed as [156]:

$$E_i + h\upsilon = \left(\hbar^2/_{2m^*}\right)k_i^2 + h\upsilon = E_f = \left(\hbar^2/_{2m^*}\right)k_f^2 \qquad (1)$$

$$\hbar k_i + \hbar k_{photon} = \hbar k_f \qquad (2)$$

Above, k_f and k_i are the final and initial wave vectors, υ is the frequency of the external source to excite the electron to final state and m^* is the mass of each particle in their respective state. Also, is clearly observed that the phonon momentum is much bigger than the photon momentum, due to following equations:

Photon momentum

$$\hbar k_{photon} = \hbar.2\pi/\lambda_{photon} \qquad (3)$$ to λ=1000 Å in IR (infrared), k_{photon} ~ 10^6 m^{-1}

Phonon momentum

$$\hbar k_{phonon} = \hbar.\pi/a \qquad (4)$$ a ~ 2-5 Å, k_{phonon} ~ 10^{10} m^{-1}

Where ¨a¨ is the lattice parameter

For this reason, the photon momentum can be neglected compared with phonon momentum, which is caused by lattice vibrations. As a result, the optical transitions occur only vertically between the CB and VB at same wave vector *k* or momentum on the energy dispersion curve [156].

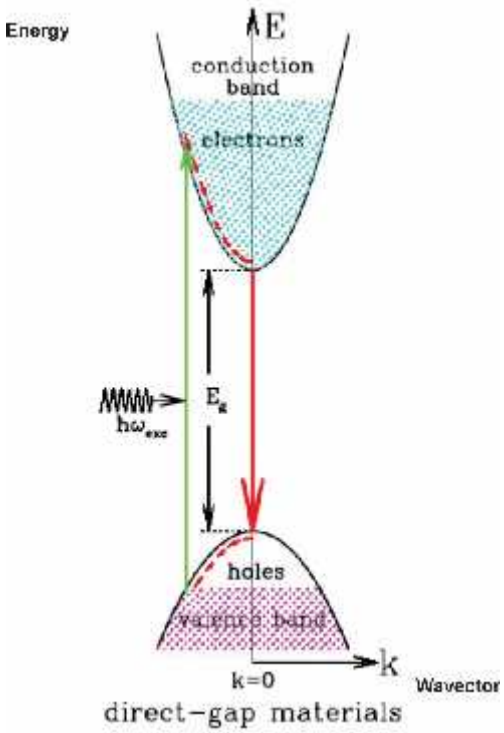

Figure 14. Diagram of an electron excitation under incident energy towards CB from VB at the same wave vector k [162].

Allowed and forbidden transitions and the corresponding energies are highly related by the electronic band structure E(k), where the energy depends of ¨k¨ (quasi momentum) established by boundary conditions. However, the symmetric properties of a semiconductor crystal and chemical bonding between its constituent elements will determine the features of the band structure. A diversity of theoretical studies have been proposed to calculate the band gap of wurtzite ZnO; these theoretical methods basically studied the energy of semiconductors and their transitions into the electronic levels. The methods based on green functions used by Rössler, the local density approximation (LDA), the density functional theory (DFT), Hartree-Fock approach, and the generalized gradient approximation (GGA),

are among the most accepted ones. However, they show shortcomings that provide an underestimated value of the band gap for ZnO [153, 163].

The hybrid functional method consists in the study of ZnO in the point Γ of the Brillouin zone [145]. The Brillouin zone is represented as a unit cell in the reciprocal space or wavenumber (k=2π/L, L is the distance between atoms), in which the reciprocal space describes the motion of electrons [164]. Where the VB arises mainly of the O^{-2} states together with the 3d levels of Zn^{2+} states as well as the CB of 4s levels of Zn^{2+} states [165]. The high position of 3d levels of ZnO in the VB generates a meaningful hybridization of O_{2p} and Zn_{3d} levels as well as a complex structure different to other compounds II-VI [156]. A typical representation of the results with LDA calculations and hybrid functional methods are shown in the **Figure 15**.

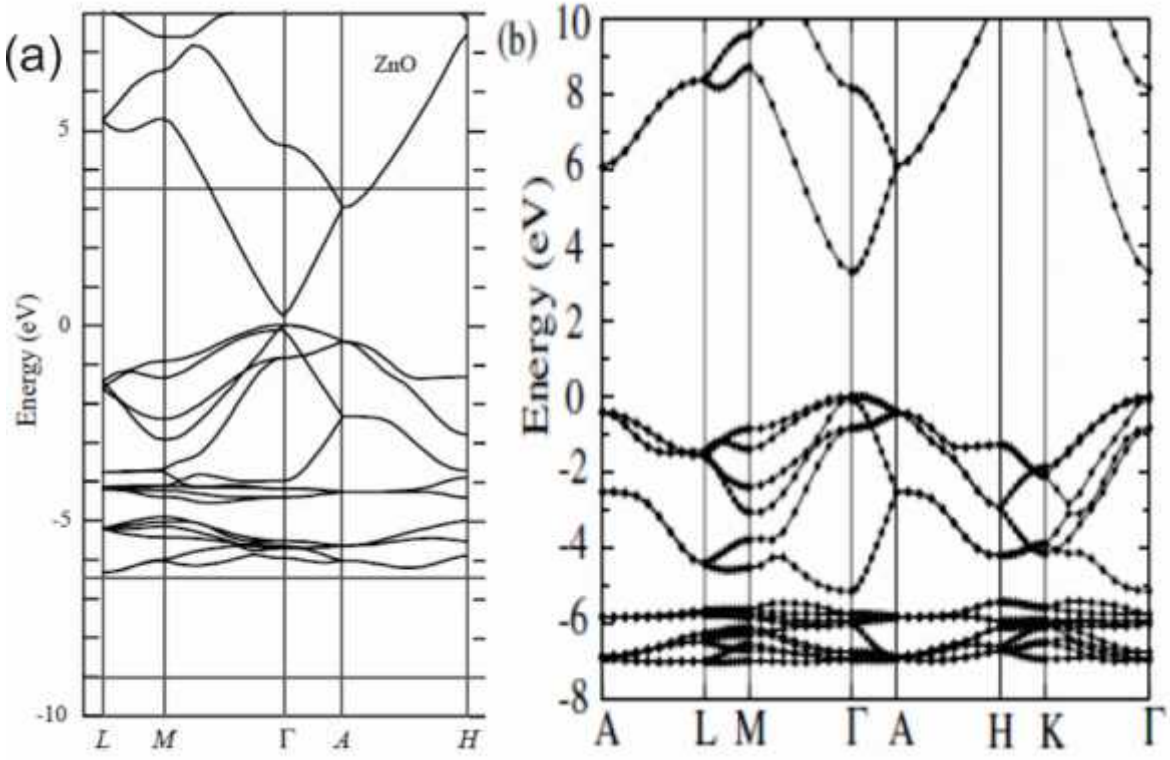

Figure 15. Band structure of ZnO calculated using: (a) LDA (left), and (b) hybrid functional method (right) [145, 156].

At 0 K, all the bands below band gap are occupied with electrons and the located above the band gap are empty. But when applying an extern factor (e.g. temperature or

radiation) to ZnO crystal, some electrons, relatively a few, are excited from the VB to the CB achieving to be gather in the CB [164]. Generally, the top of VB is the energy zero, known as valence band edge and the energy minimal point in CB is the conduction band edge. In the case of ZnO, both the maximum of VB and the conduction band edge coincide at the same Γ point in the Brillouin zone or occur at same k = 0 values. Because of these features, ZnO is classified as a direct band gap semiconductor [166]. The band gap can change by different factors such as: particle size, synthesis temperature, and doped [167, 168]. However, the value most accepted to ZnO is 3.37 e V, makes the material attractive and versatile for many optoelectronic and electronic applications [157].

Optical Properties

Absorbance

ZnO has been an important inorganic material with high demand in the research due to unique optical properties compared with others SCs, for example: GaN and CdSe [169, 170]. ZnO is a transparent SC in the visible spectra due to its large band gap at 300 K, for this reason is considered a transparent conductive oxide [169]. Apart from, ZnO is able to absorb UV light in the range 280-400 nm but it strongly absorbs below 365 nm [150, 171]. However, when the SC is irradiated by photons with an energy equal or more that band gap of the SC, they are capable of exciting an electron from the VB to the CB. In other words, the electron absorbs the energy given by photons and is promoted to a high energy state (the CB) leaving a hole positively charged in the VB. The binding of this excited electron with the hole is the so-called exciton [170-172].

An exciton can travel through all the crystal and transport energy and keep its neutral electric charge (i.e. negative by electron and positive by the hole). Due to the separation distance between electron and hole, two kinds of exciton can exist: (a) Frenkel exciton: is a tightly – bound exciton that will move as a wave all through the crystal, but the electron is near the hole; (b) Mott-Wannier exciton: the average distance of separation in the exciton is higher compared with the lattice constant, obtaining thus a weakly bound exciton. However, both Frenkel and Mott-Wannier exciton are unstable and then electron drop into the hole [173].

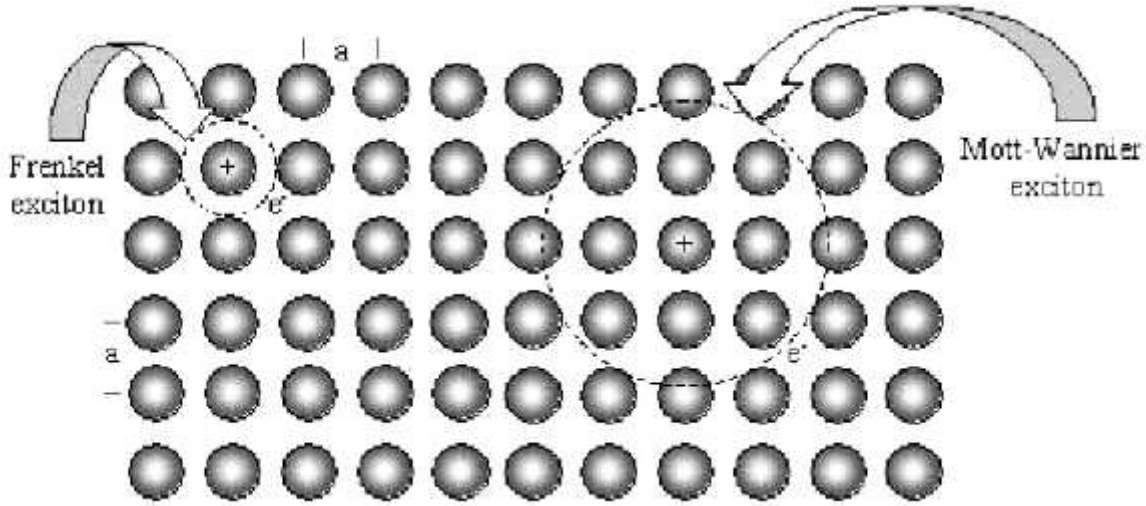

Figure 16. Illustration of two class of excitons [174].

According to the direct band gap semiconductors theory, the excitons can be generated at same wavenumber (*k=0)*, in which both electrons and holes group velocities become equal ($\frac{\partial w_e}{\partial k} = \frac{\partial w_h}{\partial k}$, where *w* is the angular velocity and *k* is the wavenumber) and due to their opposite electric charges which consequently, are attracted. Thus, the hydrogen atom is similar to an exciton (i.e. the electron orbit around of the hole). Then the binding energy of exciton can be calculated [156]:

$$E_{ex} = \frac{-m_r^* e^4}{32\pi^2\hbar^2\varepsilon^2 n^2} \qquad (5)$$

Where m_r^* is the reduced mass is the dielectric constant of SC, e is the charge of electron, both π and are constants, and n represent quantum number which determine the state level and take values n = 1,2,3, successively.

To values of: n =1 is the state with low energy.

n → ∞ is the state located in the conduction band minimum.

However, when the exciton is recombined, it emits energy as a narrow spectral line with an energy given by:

$$\hbar w = E_g - E_{ex} \qquad (6)$$

Where E_g is the band gap, the recombination process and exciton level are displayed in **Figure 17**. Although this might be true, the emission intensity in a direct transition can be weak due to the emission of one or more phonons, and then now the new energy emitted by photon is

$$\hbar w = E_g - E_{ex} - mE_p \qquad (7)$$

Where *m=0, 1, 2, 3…..*; and represent the number of phonons emitted in for every transition.

According to equation (5), semiconductors with reduced masse greater show large binding energy that is comparable with thermal energy (K_BT), where K_B is Boltzmann constant and T is the temperature. Therefore, Coulombic effects are important and should not be neglected [156]. Moreover, the binding energy of the ZnO exciton is 60 meV that is higher than GaN (25 meV) [145]. Therefore, the high exciton binding energy of ZnO demonstrates that at room or higher temperatures the excitonic emission can persist [145].

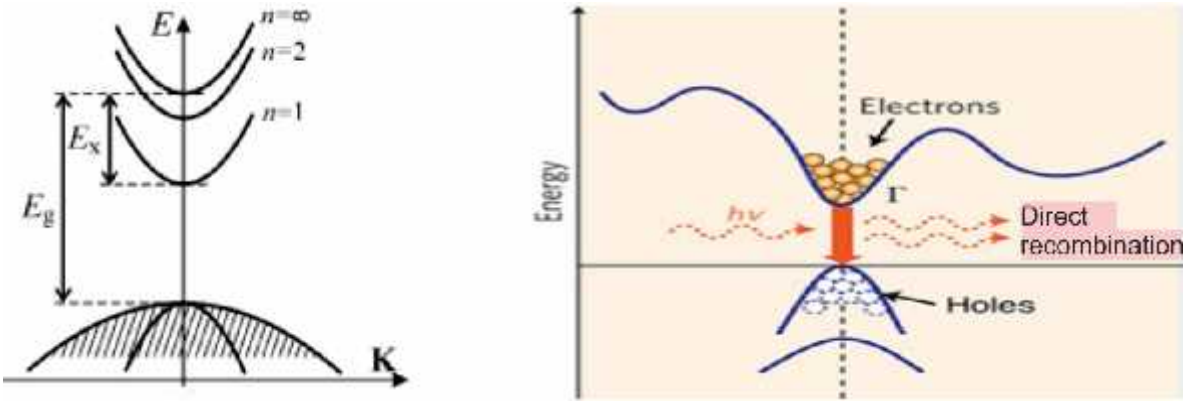

Figure 18. Representation of: (left) exciton within the energy band at same wavenumber k=0 with their respective levels, (right) recombination process, excitons can undergo translational kinetic energy and are unstable in this process therefore the electron return to VB emitting energy (photons) in the diagram energy vs Γ [156].

Photoluminescence

The optical phenomenon of energy absorbance is essential to understand the photoluminescence phenomenon (PL). PL measurements are a useful tool to study light emission; this phenomenon involves absorbing light at a suitable energy, which is needed to excite the electrons of the material. These electrons can be relaxed returning to the VB emitting photons of a specific energy. Although the electron can return through a direct transition to the VB, also known as fluorescence or radiative exciton recombination, it can also be captured by energy levels located within band gap, emit light and go back to its initial position in the VB, a process known as phosphorescence. Moreover, the energy emission depends of the kind of material and the corresponding particle size [175]. In addition, the impurities and defects are responsible of the light emission characteristics or act as activators of PL.

In PL measurements the excited electron with high energy can relax towards the VB by means of radiative or non-radiative transitions. Non-radiative transition is a process of electron relaxation without photon emission, in other words the energy is interchanged with the lattice by means of heat due to thermal vibrations via phonons emission by ways of trap states, it happens to a direct band gap SC. Furthermore, also is important to consider for the same process, the next points: not all defects may be done as recombination centers to achieve that the carriers be able to recombine in a radiative way. Other point is that the energy lost due to the captured carriers can excite another close carrier in the crystal to then increase the non-radiative transition. In radiative transition, the electron relaxes releasing energy in way of photons [175]. Exists different kinds of radiative transitions: a) direct transition from CB to VB, also known as electron-hole recombination; b) transition between CB and acceptor shallow impurity state, or the transition of donor shallow impurity state toward VB; c) transitions between donor and acceptor deep states.; (b) and (c) are trap states related to the capture of the electron [175]. Figure 19 shows the representation of these states.

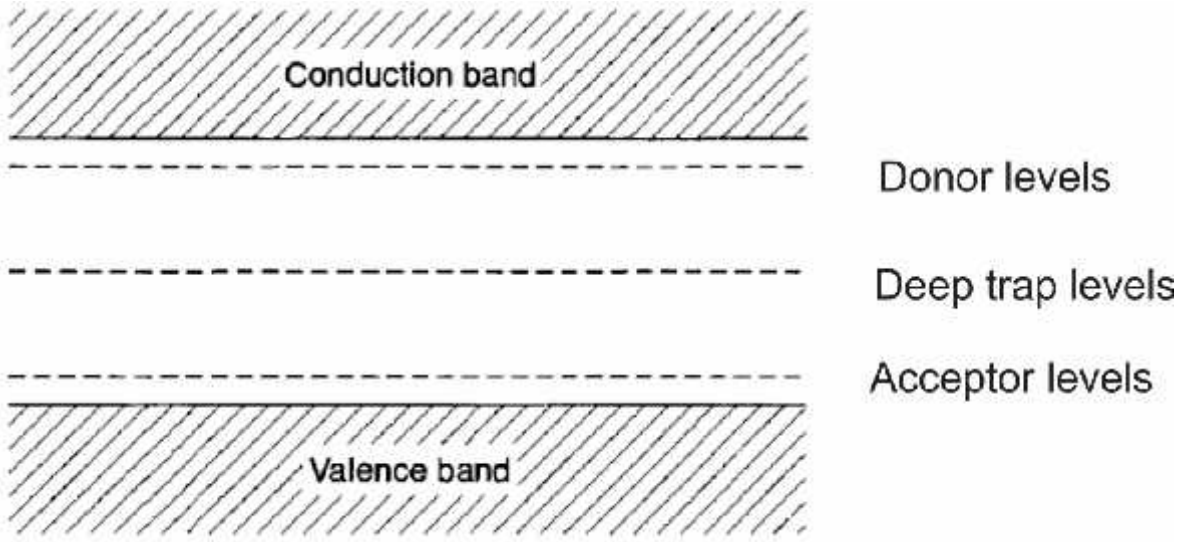

Figure 19. Scheme of band gap level showing donor levels below of the CB edge, acceptor levels site above the top of VB, and deep trap levels close to the half of the band gap energy [164].

Intrinsic PL

There are three distinct process involved with intrinsic PL. The first is the transition from band to band, and occurs when electrons in the CB are recombined with holes of VB to emit light; this process is commonly observed in crystal of high purity at room and high temperature. The second kind of process is the exciton luminescence in which an electron of the CB and a hole interacting between they move within of the crystal; as a consequence, the material emit light due the recombination both electron and holes. The last one is the cross-luminescence route where an electron is recombined with a hole of the outer core of the VB and then emits light. It will take place when the energy difference between VB and the core VB is less or equal than the corresponding band gap energy [156, 176].

Extrinsic PL

Is another common PL kind and is characterized for the presence of foreign atoms or impurities than are incorporated to host matrix achieving change the energy level, and in particular these foreign atoms do as activators of PL in the material structure. This phenomenon is categorized in two different ways: a) localized luminescence, which is attributed to excitation and emission process confined in center localized, and b)

unlocalized emission, this emission is related with isoelectronic traps and has an important function in SCs of indirect band. Example of Isoelectronic traps is bound states (e.g. Donor-acceptor level) [156, 175, 177]. As mentioned, the incorporation of impurities of dopant is an important factor to in the creation of energy state like luminescence centers. The choosing of dopant atom is crucial to optical property; in the next part a brief description of them is explained.

N-type doping

In this type of doping, the dopant atom fills the space leave for the pattern atom in the lattice. Due to the dopant atom possess more electrons that pattern atom, these electrons additional generate non-bonding electrons which create donor energy levels near of the CB, this facility the promotion of electrons to CB [178].

P-type doping

In this case, the dopant atom originates an electronic deficiency in the electronic levels of material, creating empty acceptor energy level just up of the VB. This acceptor level is capable of accepting an electron from the VB and leaving a hole in this latter band [178]. In a donor level the electron can passes easily to the CB, as well as in the acceptor level can accept an electron from VB, leaving thus a hole in the high part of VB; these is due to the excitation energy required to add electrons to the acceptors levels and achieve ionize donors levels which are much smaller than the energy produced to the heat at ambient temperature. Hence, the particular consideration under ambient conditions (T=300 K), all acceptors is negatively ionized and all donors are positively ionized; even both acceptor and donor levels are also known as shallow traps holes and electrons, respectively. Others trap states can exist within the band gap and are located in the top or bottom of the half band gap known as deep trap levels, these deep traps are not widely ionized, due to the energy required to excite or ionize are large; in particular defects related with broken bonds, or displacements of atoms induce by a strain are example of these deep traps [164]. **Figure 20** shows both, p and n type doping.

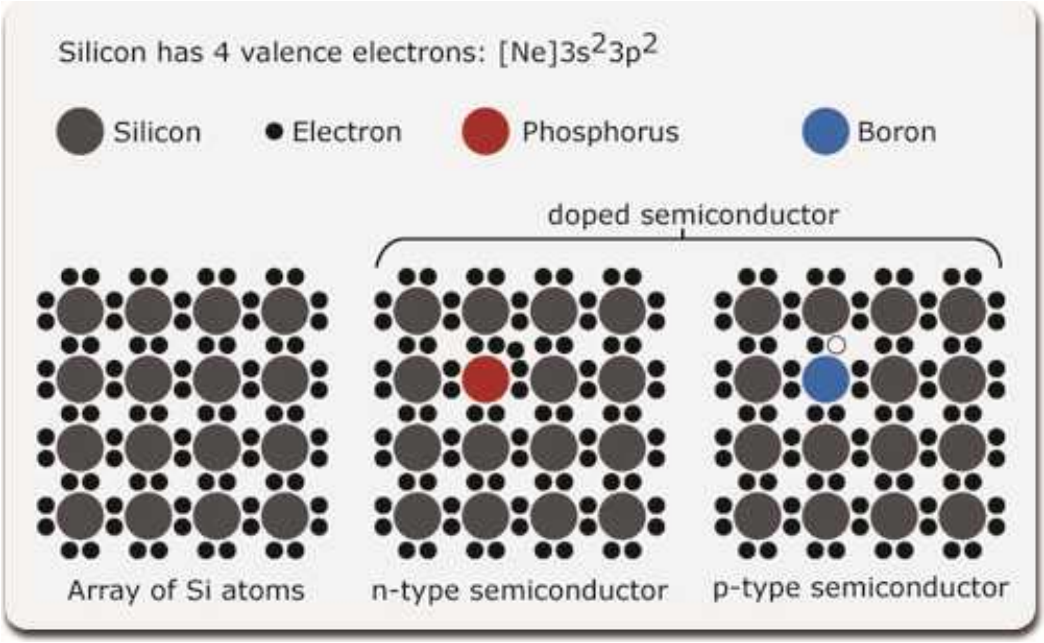

Figure 20. n-type and p-type SC configuration of doping in the Silicon atom [179].

Wurtzite ZnO is an intrinsic n-type SC because to nonstoichiometric amounts of Zn and O in the crystal structure as result of naturally presence of defects such as: interstitial zinc (Zn_i) and oxygen vacancies (V_O) with a high electron concentration around of 10^{16}-10^{17} cm^{-3}, despite, the origin of this intrinsic behavior has not been totally understood, without any clear evidence [145, 180]. Earlier studies realized by Look *et al* suggested that Zn_i are the dominant, predominant shallow donors at comparison of V_O, with ionization energy in the range of 30 to 50 meV. On the other hand, theoretical studies also were evaluated for example in the growth of ZnO films exposed at H, in which the H acts as a shallow donor in ZnO film with ionization energy around of 30 meV. This is possible due to H which possesses a large mobility and can readily fit into ZnO [156]. Although, it has been checked experimentally that intentional n-type doping with group III elements (e.g. Al, In and Ga) are adequate substitutional elements on the Zn sites as well as group VII elements (e.g. Cl, I, Br) on the O sites [181]. To the particular case of Ga doped ZnO films, Park *et al* revealed that this material had low electricity resistivity of $8.12 \cdot 10^{-5}$ Ωcm, this result is due to an excessive electrons generation on ZnO when doped with Ga element [181]. On the contrary, p-type doping in SCs with wide band gap is rather challenging. The drawbacks of p-type doping in ZnO can be for some factors such as: (i) acceptor dopants

could be compensated by the native defects (i.e. Zn_i and V_O) and background H impurities, (ii) the poor solubility of the acceptor dopant in the host material, and (iii) the existence of acceptor in a deep impurity level with high activation energy [182]. The elements likely to p-type doping in ZnO are group IA (e.g. Li, Na, Ag, K, Zn vacancies and Cu) and group V (N, Sb, P and As). In addition, it has been demonstrated that the incorporation of these dopant acceptors in ZnO causes self-compensation between interstitial and substitutional sites in the ZnO structure [183]. Equally important, the ionic radii of dopant atom and host atom as well as the size of interstices, interstitial sites are important to that cations occupied these interstitials sites. Ions with largest radius can expand the unit cell length [184].

In fact, diverse efforts have been realized to improve its structural and optical properties of ZnO NPs by improving the method of synthesis or by incorporating dopant or impurities in the host lattice. However, most of the works on ZnO nanostructures have been focused in the PL spectra [185-187]. The strong emission peak of PL in the UV zone (below of 390 nm to 100 nm) at 360 nm is attributed to the exciton transition or also known as transition of electron emission from the CB to VB and this emission is characteristic of ZnO bulk [188]. Albeit, in the same cases reported the absent of this emission peak. The reasons for this absence of emission to happen is due to: first, the energy of excitation applied is less than the optical band gap of ZnO nanostructure and the other possible reason is the increment of the defect density associated with the rise of intensity in the visible emission [189, 190]. However, the emission in the visible range is related to defect states, mainly interstitial zinc and oxygen vacancies. The defect states can be located in shallow levels as well as deep levels within of band gap. The violet emission is associated to the transition from shallow donor levels close at the CB to the VB, and is related to the existence of Zn_i in the ZnO lattice. Another important PL band in ZnO is the green emission band and is represent the V_O. The green emission band was associated to loss of oxygen atoms which generates empty places in the lattice. These results reveal the intrinsic defects of ZnO are consistent with those of bulk ZnO [191].

Different efforts have been carried out to improve the properties of ZnO NPs, but in some cases were not achieved. Yu-Chih Tseng *et al* [10] investigated the incorporation of Ti in ZnO and the effect done in the structural and optical properties by a chemical process

called sol-gel. Were it was observed that when the concentration of Ti increases, the intensity of the diffraction peaks in the wurtzite structure decreases significantly, suggesting a weakened crystallinity in the nanoparticle when incorporate Ti on the ZnO lattice. The study of its optical properties such as Photoluminescence was done with Ti and the UV emission band increase adding Ti was observed. They suggested that the reduction of V_O is due to incorporation of Ti increasing the energy formation of V_O; and to corroborate this, Raman Spectroscopy measurements were made in which the peak associated to defects (around 576 cm^{-1}) also decreased at higher concentrations of dopant as well as in multiple peaks around of 440 cm^{-1} indicating the poor crystallinity of Ti-doped ZnO NPs [192].Whereas in Ti doped ZnO nanorods, the green emission intensity associated with V_O increases and the UV emission peak (related to free excitons) intensity increases too when Ti is incorporated on the ZnO host, this behavior is attributed to a shift in the band gap of ZnO nanorods doped [193]. Ti-doped ZnO NPs can change the band gap, an increment of band gap involves a size reduction of NPs; for instance a band gap from 3.37 to 3.6 eV with a size from 25 to 6 nm [194]. However, Ti^{4+} could also be incorporated in interstitial sites and act as the scattering site, this is due to ionic radii of Ti^{4+} (0.68 Å) is less than Zn^{2+} (0.74 Å); also high concentrations of doped Ti^{4+} could generate large electrons and increase scattering centers [195].

Lithium (Li) is also used to dope ZnO. Li^+ has an ionic radius of 0.60 Å that is smaller than Zn^{2+}, which would facilitate its incorporation into the ZnO host lattice. This incorporation would also lead to the rise of the photoluminescence intensity when compared to un-doped ZnO [196]. The optical properties of Li doped ZnO has been widely studied in thin films, in which the PL spectra display a high intensity in the emission peak at 397 nm when incorporated Li into wurtzite ZnO structure as well as weak intensity in both emission region at 433 nm and green emission band; where the band in the violet region is attributed to transitions between interface traps (in this case, grain boundaries) and the VB, and the remaining emission band associated to intrinsic defects (e.g. Zn_i and V_O) [197]. Besides, the impurities of Li can be incorporated on the ZnO lattice in different sites, for example: replace the Zn sites, fill the Zn_i, or occupy interstitials sites; inclusive due to that Li^+ possess a smaller ionic radius than Zn^{2+}, this allows best diffusion of Li impurities in the ZnO structure [198]. The majority of the works reported for the singlet oxygen

measurement use fluorophores or photosensitizers such as porphyrin, “thermofin” between others applied *in vitro* and *in vivo* [46]. On the other hand, Y. Collantes and O. Perales [150] worked with pure ZnO nanoparticles doped with Fe and Mn. She observed an increase in the SO (O_2) production when the concentration of the dopant in the ZnO nanoparticles was increased. When the ZnO nanoparticles are doped with 2% Mn^{2+}, they generated a larger amount of SO, indicating that this behavior can be attributed to the majority of defects found because of the confinement of electrons in trap states. Similarly, Bailon and Perales worked with QDs and observed a greater production of SO in CdSe QDs covered with thioglycolic acid [199].

On the above basis, it becomes evident that introduction of dopant atom into a ZnO NP lattice could promote the formation of carriers as well as trap states necessary to trap the electron that in turn, can give energy to molecular oxygen to generate SO. Therefore, ZnO-based NPs can be a promising material as anti-carcinogenic and anti-bactericidal agent capable to be used in PDT. Accordingly, the main focus of the present research will be the proof-of-concept related to the direct effect of defect incorporation and generation of SO species, using UV light, and assess the possibility to consider pure and doped-ZnO as direct PSs. Additionally, a preliminary study on the 2-photon excitation of these nanomaterials will also be presented.

CHAPTER 3. Experimental

3.1. Materials

All chemicals were analytical grade reagents and used as bought without any further purification. Zinc acetate dehydrate (ZnAceD) [Zn(OOCCH3)2·2H2O, 98%] was used as the precursor salt, titanium (IV) isopropoxide [$Ti(CH(CH_3)_2)_4$, 99%] and lithium acetate dehydrate [$Li(CH_3COO) \cdot 2H_2O$, 99%] were both used as synthetizing dopant element in two separate experiments, whereas triethyleneglycol [TREG, $C_6H_{14}O_4$, 99%] was the solvent. All synthesized NPs experiments had a total concentration of 0.08 mol/L.

3.2. Synthesis of pure and doped ZnO NPs.

All NPs were synthesized under size-controlled conditions using a modified version of the polyol method proposed in our earlier works [150], and described as follows.

3.2.1. Synthesis of ZnO NPs

ZnAceD (0.08 mol/L) was dissolved in TREG in a three-neck spherical flask and heated to reach 180 °C using a heating mantle to start the nucleation process of ZnO NPs. The solution was constantly stirred for 30 min at this temperature under reflux conditions. At the end of the contact period, the suspension was quenched at 4˚C to avoid any additional crystal growth. Produced NPs were coagulated by centrifugation, washed using ethyl acetate and ethanol and dried at 60°C for 24 hours.

3.2.1. Synthesis of Ti- and Li-doped ZnO NPs

Suitable amounts of zinc acetate and titanium or Lithium precursors were dissolved in TREG in a three-neck spherical flask and mixed under reflux conditions. The total ions concentration was kept constant at 0.08M for different dopant concentrations of 0, 5 and 9 at%, respectively. The solution was vigorously stirred and heated up to 180°C for 30 min

using a heating mantle. Subsequently, the solution was quenched in a bath cold at 4˚C. Lastly, the nanoparticles were coagulated using ethyl acetate and ethanol, and dried at 60°C for 24 hours.

3.3. Materials Characterization

The crystalline structure of pure and doped ZnO NPs was investigated by X-Ray Diffractometer (XRD) Siemens D500 with Cu-Kα radiation (λ= 0.1542 nm). The average crystallites were calculated using Scherrer's equation [200] without correction by instrumental error. The powders were also characterized by Fourier-transformed infrared (FTIR) Spectroscopy using a Shimadzu IR-Affinity spectrometer to identify the presence of functional groups on the surface of the NPs and confirm the functionalization of ZnO by polyol functional groups. The study of structural nature and the defects in the samples were carried out by Raman Spectroscopy (Confocal Raman Microscope XploRA, Horiba). The morphology and size of synthesized NPs were determined using a Scanning Electron Microscopy (SEM) (JEOL JSM-7500F). The optical properties were measured in a DU 800 Spectrophotometer and Shimadzu RF-5301PC Spectrofluorometer with a 150W continuous ozone-free Xenon lamp. As-synthesized NPs were excited using Multiphoton Excitation Fluorescence Microscopy (ZEISS LSM 880) with a Chameleon Ultra II NIR laser fully tunable between 690 and 1040 nm.

3.4. Generation of Singlet Oxygen Species (SO)

The capacity for ROS generation, specifically SO, was determined using a Singlet Oxygen Sensor Green (SOSG) reagent kit from Life Technologies. SOSG is a commercial fluorescent detection reagent of SO. SOSG is highly selective for SO and does not show sensitivity to other ROS such as superoxide, hydroxyl radicals or other ROS type I. Initially this SOSG displays a weak blue fluorescence, but only when SO species are present emits a green fluorescence (excitation/emission maxima ~ 504/525 nm) [201]. The main component of the SOSG is 9-[2-(3-Carboxy-9,10-dimethyl)anthryl]-6-hydroxy-3H-xanthen-3-one (DMAX), which reacts with generated SO to give fluorescent DMAX-endoperoxide (DMAX-EP). Besides, DMAX is more efficient compared with other existent molecular probes which identify SO, this is due to its high sensibility and fast detection

[202, 203] (**Figure 20)**. Both DMAX and DMAX-EP have the same excitation/emission wavelengths (492/525 nm); however, DMAX display a small fluorescence while DMAX-EP highly increases the fluorescence when SO species are present; i.e. the larger the 525nm peak intensity, the higher the generation of SO [201]. The corresponding protocols (detailed in the following paragraphs) were followed to assess the capability of pure and doped ZnO as direct generators of SO under UV-illumination.

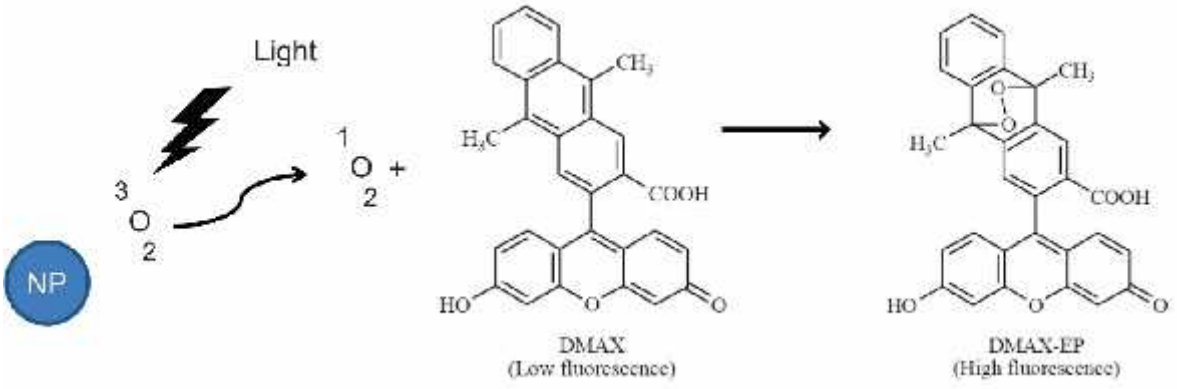

Figure 20. Reaction of SO produced by the excitation of NP with 9-[2-(3-carboxy-9,10-dimethyl)anthryl]-6-hydroxy-3H-xanthen-3-one (DMAX) to generate DMAX-EP. [202]

Protocol to determine the generation of SO

- Preparation of Stock Solution

The stock solution was prepared with sensor green (that contained 10 µg of DMAX), methanol HPLC grade ≥99.9% and deuterated water at 50%. The sensor green was dissolved in 33µL methanol HPLC and add 297 µL of deuterated water. The final concentration of DMAX was 0.5 mM.

- Solutions Preparation

Preparation of blank solution A (without nanoparticles):

a. In small vial add 1447 µL of deuterated water at 50% and 3 µL of the stock solution.

b. Add 50 μL of deionized water and measure the fluorescence (baseline information).

Preparation of the suspension containing the nanoparticles (Solution B)

The solution was prepared in the same way as the blank. The only difference is the addition of the deionized water containing suspended nanoparticles (333.33 μg/L). The fluorescence of this suspension (without UV illumination) was also measured.

3.5. Measurement of Singlet Oxygen

The corresponding fluorescence measurements of the nanoparticles suspended in the SOSG solution were carried out in 30- second periods with 30-second intervals between each measurement. Figure 21 shows the corresponding experimental sequence. Then to start the measurements: (a) the suspension was excited with 488 nm light (slit 3-3) and the PL spectrum was recorded as a T0 (PL spectrum without excitation of nanomaterial), (b) after 30 seconds, the solution was excited at 345 nm (slit 5-5) to generate SO. Similar cycles were repeated every 30 seconds by duplicate.

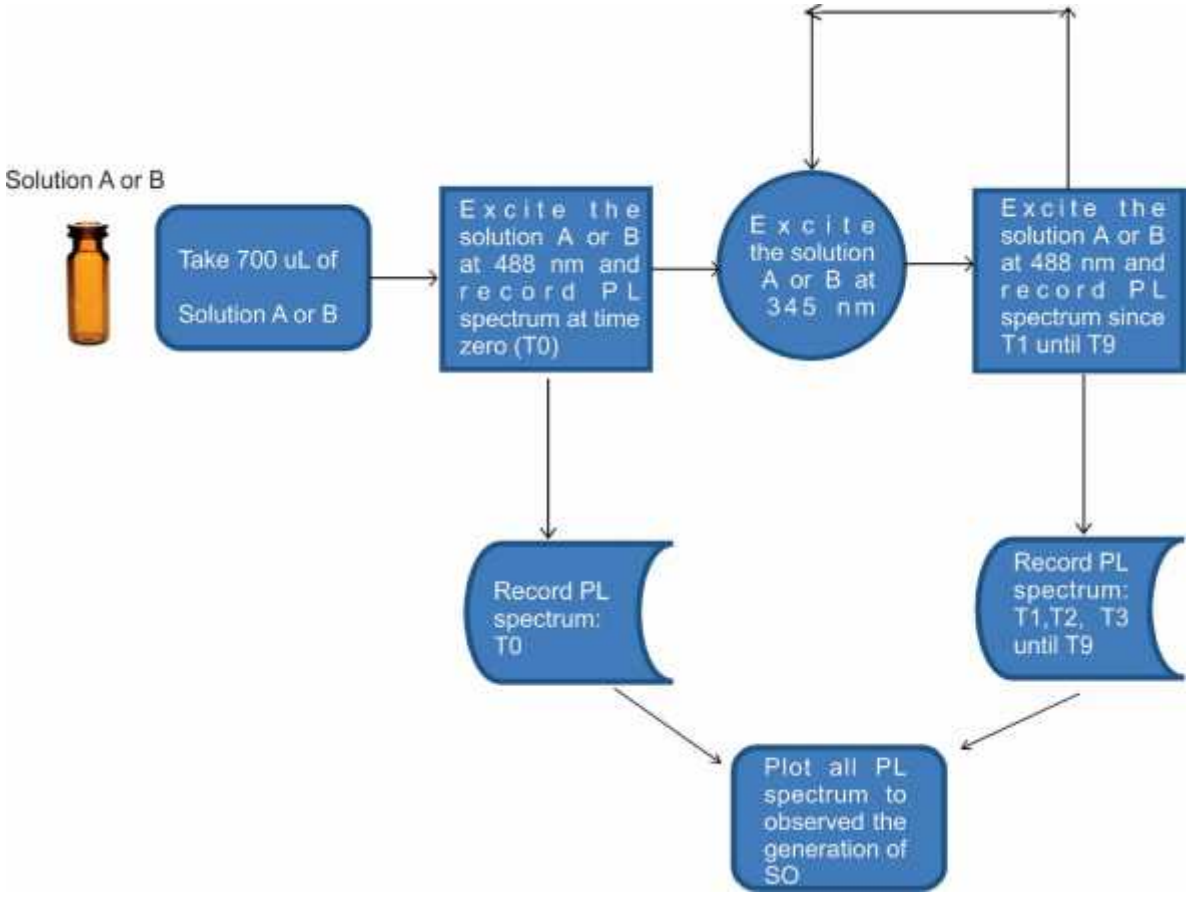

Figure 21. Experimental sequence to determine SO generation in the blank and the nanoparticles-containing sensor green solution. T0 until T9 represent the measurements of the emission intensity at 525nm, which corresponds to the fluorescent DMAX-EP compound (formed only when SO is present). An excitation wavelength of 488 nm was used.

Chapter 4. Results and Discussion

4.1. Pure ZnO NPs

4.1.1 Structural Characterization

4.1.1.1 X-Ray Diffraction (XRD)

The XRD patterns of as-synthesized ZnO NPs by the modified polyol method and the corresponding information for bulk ZnO (JCPDS No.800075) are shown in **Figure 22**. The angular location and relative intensity of the diffraction peaks confirmed the formation of hexagonal wurtzite in ZnO NPs. The average crystallite size was estimated using the Scherrer's equation (14.3 ± 1.03nm) [200]:

$$D = \frac{0.89\,\lambda}{\Delta B_{hkl}.cos\Theta_{hkl}}$$

Wherein ΔB_{hkl} is the width of the XRD peak at half height (FWHM), λ is the wavelength of X-rays, Θ is the Bragg diffraction angle and D is the average crystallite size.

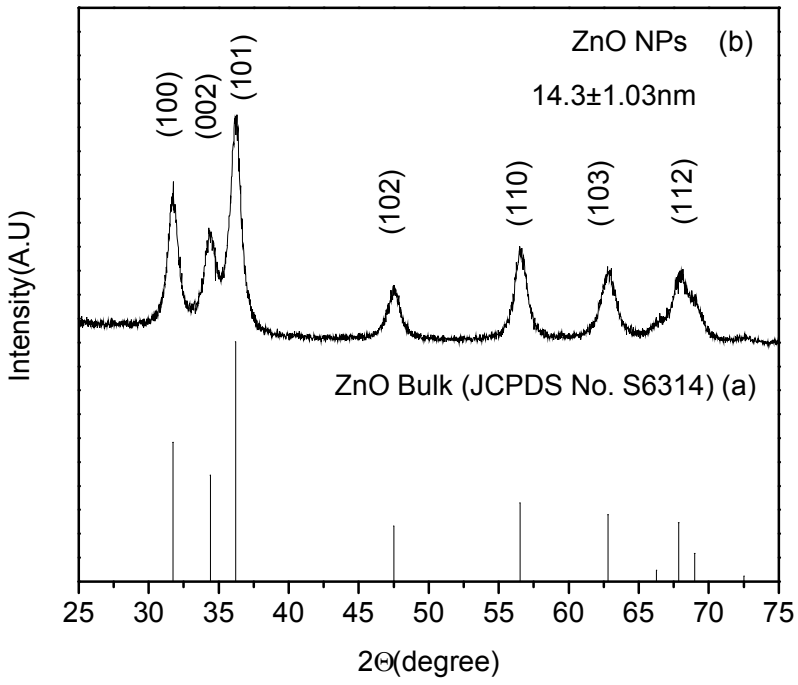

Figure 22: XRD patterns for (a) Bulk ZnO material, and (b) synthesized ZnO NPs. The average crystallite size was estimated at 14.3 nm.

4.1.1.2. Fourier Transform Infrared Spectroscopy (FTIR)

The FTIR spectrum of ZnO is shown in **Figure 23**. The broad band in the 3500 cm^{-1}-3100 cm^{-1} range is assigned to O-H stretching vibrations of hydroxyl groups, whereas the 1400cm^{-1} band can be assigned to C–O stretching modes of alcohol and acetate groups [203]. The band at 1630 cm^{-1} is attributed to the presence of remaining water [204]. In turn, the weak band at 901 cm^{-1} is characteristic of the C-O bonds in the alcohol group of the polyol (TREG). The strong band centered at 554 cm^{-1} is characteristic of the Zn-O bond in the ZnO phase [205]. These functional groups located in the surface of nanomaterial should avoid some agglomeration by means of electrostatic repulsion forces, leading to the formation of monodisperse NPs [203].

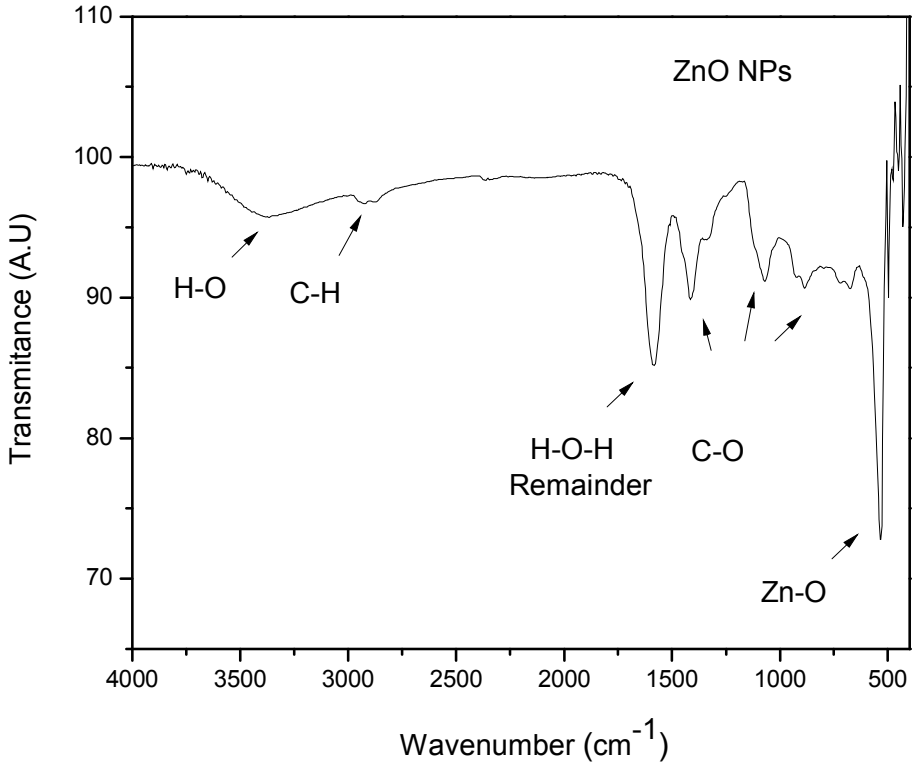

Figure 23. FTIR Spectra for ZnO nanoparticles synthesized by a modified polyol process.

4.1.1.3. Raman Spectroscopy

Figure 24 shows the Raman modes related to vibrational modes in ZnO at room temperature. The E_{2H} mode is observed at 447cm^{-1} and is associated to the crystalline arrangement in wurtzite structure, confirming XRD results. Besides, this Raman mode can also be associated to the vibration of oxygen atoms [206]. The band at 571cm^{-1}, also known as E_1(LO), is attributed to structural defects (i.e. mainly V_O and Zn_i) in the ZnO structure [207]. The small band at 393cm^{-1} is associated to A_1(TO) mode, while the band at 655cm^{-1} corresponds to the intrinsic mode of in ZnO, [207], which is characteristic of the transverse optical (TA) and longitudinal optical (LO) modes [208].

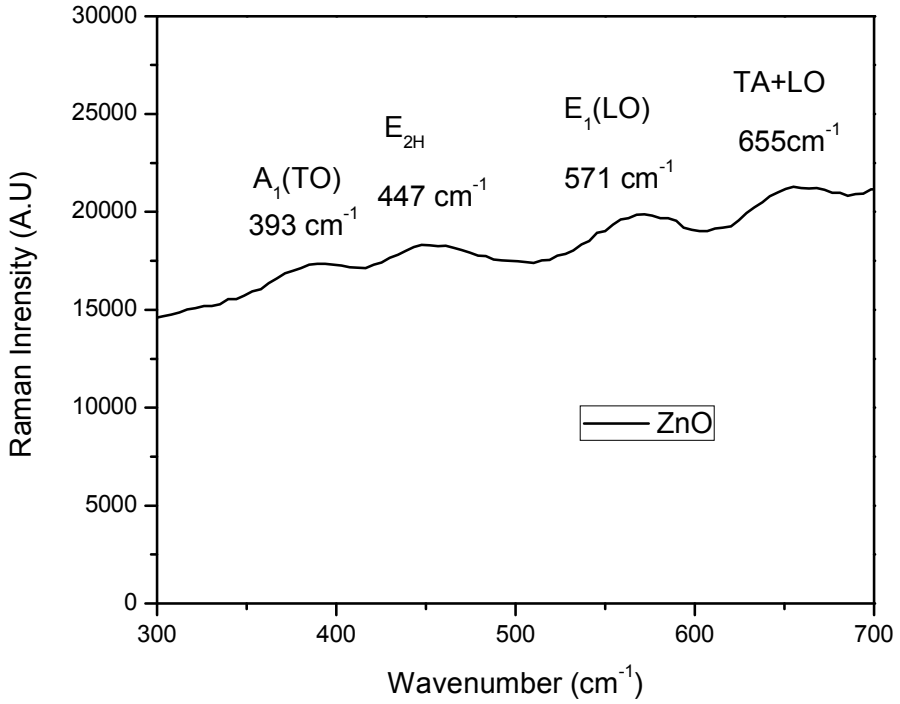

Figure 24. Raman Spectra of as-synthesized ZnO. The sample was excited at 638nm.

4.1.2. Morphological property

4.1.2.1. Scanning Electron Microscopy (SEM)

The ZnO NPs surface morphology was observed using SEM as shown in **Figure 25**. The results from SEM analyses (**Figure 25**), evidenced the formation of sub-micrometric secondary particles conformed by tiny crystallites in the 14-15 nm range. The ZnO particles exhibit a size of 131 nm and a good monodispersity.

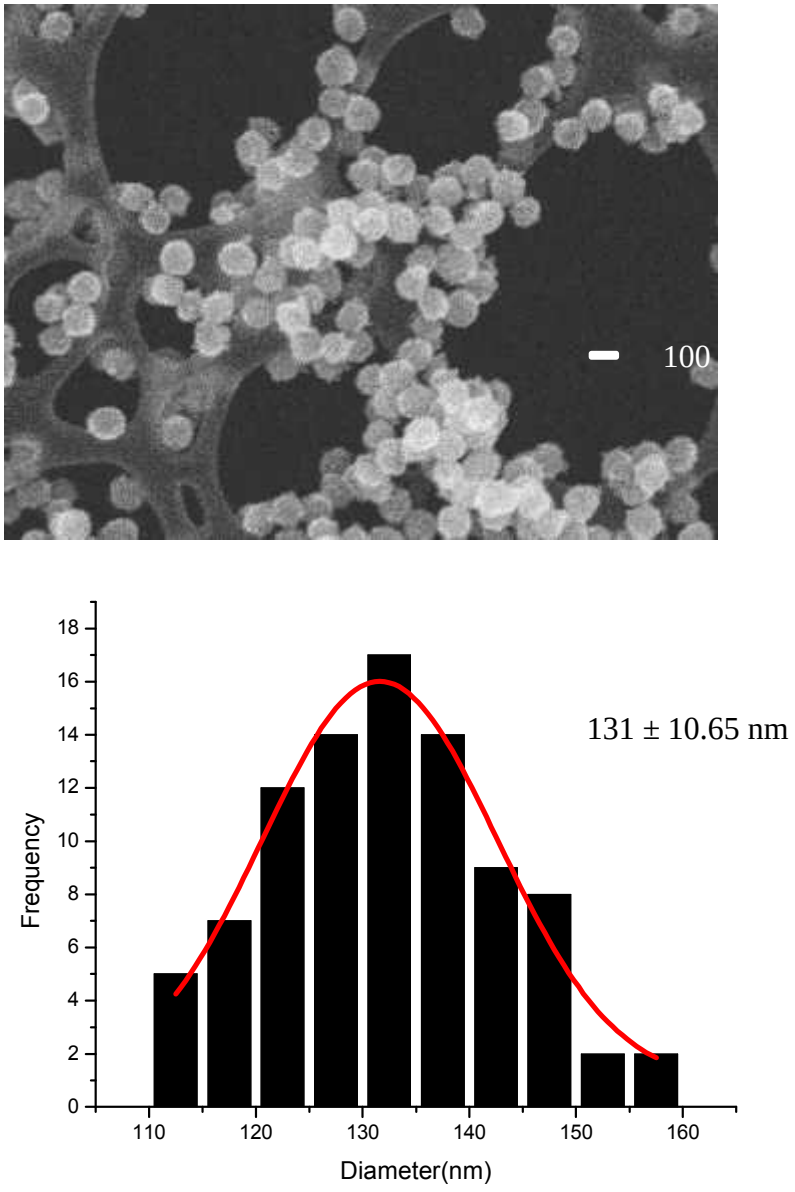

Figure 26. (Top) SEM image of ZnO nanoparticles synthesized by polyol method at 180°C; (Bottom) Size distribution for ZnO NPs. The size was estimated at 131 ± 10.65 nm.

The merits of the polyol-based approach, when compared to others (e.g. laser ablation, sol gel, and thermal decomposition of precursors), relies on the feasibility to produce crystalline, monodisperse nanoparticles. Besides, it can be easily scaled-up using commercial equipment [209]. In the polyol method, the oxide precursor reagent undergoes hydrolysis and subsequent dehydration [210, 211]; the hydrolysis takes place because of the salt precursor which contains water molecules [212]. The polyol works as both, the solvent and the surfactant agent that prevented particle for excessive aggregation and uncontrolled growth. [213, 214]. **Figure 25** shows ZnO NPs with a quasi-spherical shape. The polyol solvent (TREG) plays the role of stabilizer agent that prevent the agglomeration of NPs, obtaining NPs with good crystallinity and monodispersity [10].

4.1.3. Optical Properties of ZnO NPs

4.1.3.1. Absorbance (UV-Vis Spectroscopy)

The room temperature UV-vis absorption spectrum of ZnO nanoparticles synthesized by polyol method at 180°C dispersed in deionized water is shown in **Figure 27.**

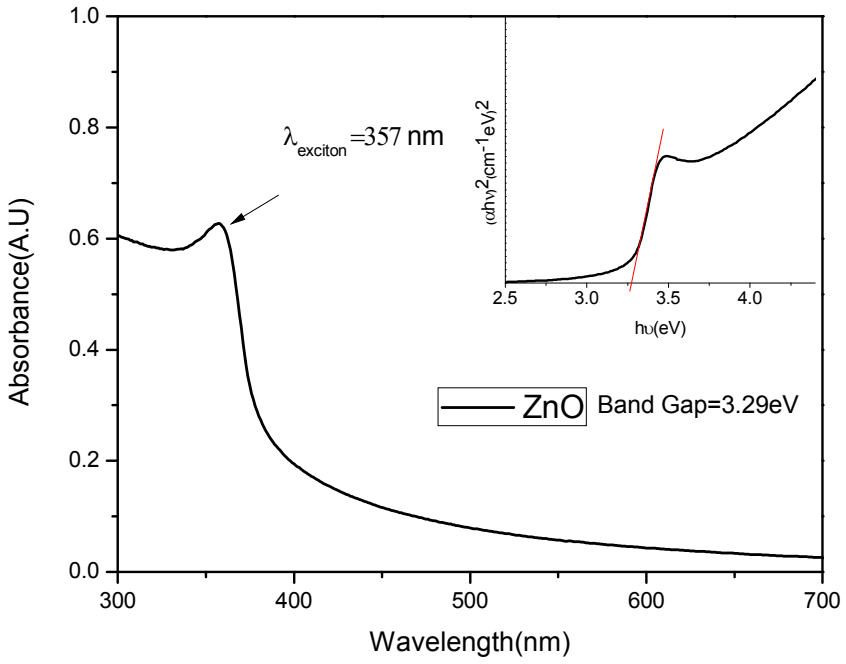

Figure 27. Absorption spectra of prepared ZnO NPs synthesized by polyol method at 180°C. The inset shows determination of the band gap energy by the extrapolation method of the curve $((\alpha h\upsilon)^2$ vs $h\upsilon)$ for ZnO NPs.

The absorption spectra revealed the presence of a strong exciton peak at 358nm which is typical of ZnO. The band gap energy was estimated following the Tauc's relationship at 3.29eV (inset of **Figure 27**). The estimated value was in agreement to reported values [188].

4.1.3.2. Photoluminescence (PL) Spectroscopy

The room temperature PL spectrum of ZnO NPs monitored at an excitation wavelength of 345nm is shown in **Figure 28**. This spectrum clearly shows two emission peaks at wavelengths of 361nm and 392nm. The PL peak at 361nm corresponds to the main emission peak of ZnO and is associated with the exciton recombination (i.e. the electron returns from CB to VB occupying the hole that leaved under the excitation). The second emission is attributed to Zn_i shallow donor levels, in which the electron relaxes from the CB and is captured by a trap state located within a band gap level to finally release photons [188-190, 215].

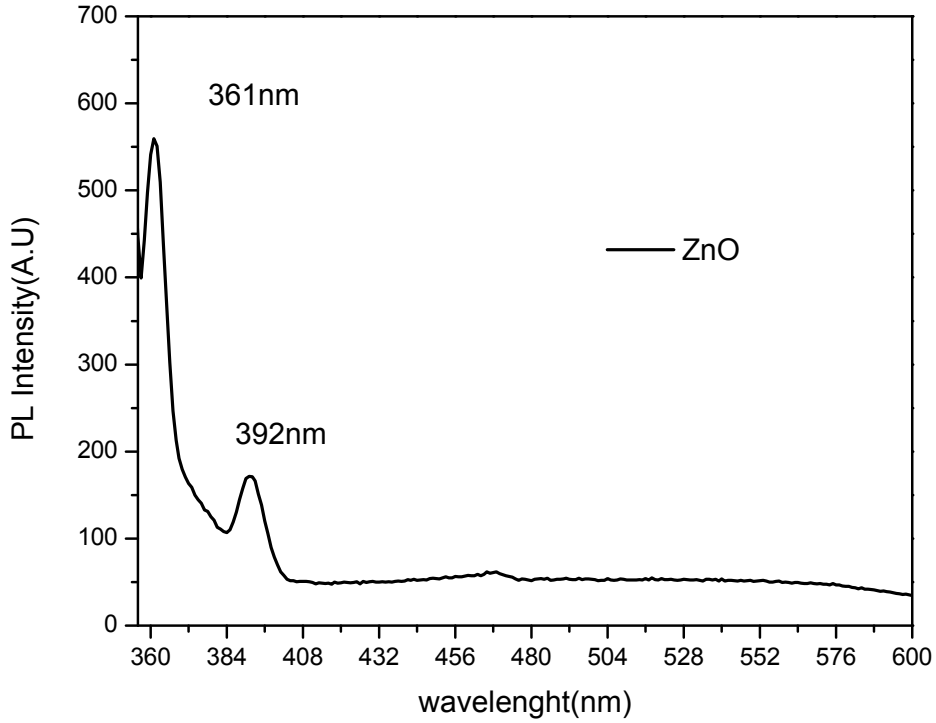

Figure 28. Room temperature PL emission spectra of ZnO NPs excited at λ_{ex}=345nm.

The presence of the emission band at 390nm is attributed to the presence of trap states. These trap states are associated with structural defects, due to incorporation of Zn ions in interstitial sites of host lattice [188].

Concluding Remarks

XRD measurements confirmed the development of well-crystallized Wurtzite-ZnO structure without presence of secondary phases, with an average crystallite size of 14nm. ZnO NPs displayed a good chemical stability with the presence of relatively small residues according to FTIR spectroscopy. SEM analyses evidenced the formation of spherical, highly monodisperse particles averaging 131nm in diameter. However, the size of these particles are adequate to attach the cancer cell.

UV-VIS confirmed the presence of a very strong exciton peak at 357nm, which suggested that ZnO nanoparticles exhibit a high absorption of UV energy. The presence of intrinsic defects in ZnO nanoparticles was suggested by both, Raman and Photoluminescence spectroscopy measurements. The emission peaks observed at 390 nm is attributed to the generation of trap states due to interstitial Zn in the host oxide.

4.2. Effect of Doping in ZnO Nanoparticles

4.2.1. Effect of Dopant Level in Ti-Doped ZnO Nanoparticles

4.2.1. 1. Structural Characterization

4.2.1.1.1. X-Ray Diffraction (XRD)

Figure 29 shows the X-ray diffractograms for pure and Ti-doped ZnO. The diffraction pattern of TiO_2 is presented for comparison purposes only and supports the apparent absence of secondary phases. Also in this case, all peaks correspond to wurtzite ZnO suggesting the actual incorporation of Ti species into the oxide lattice.

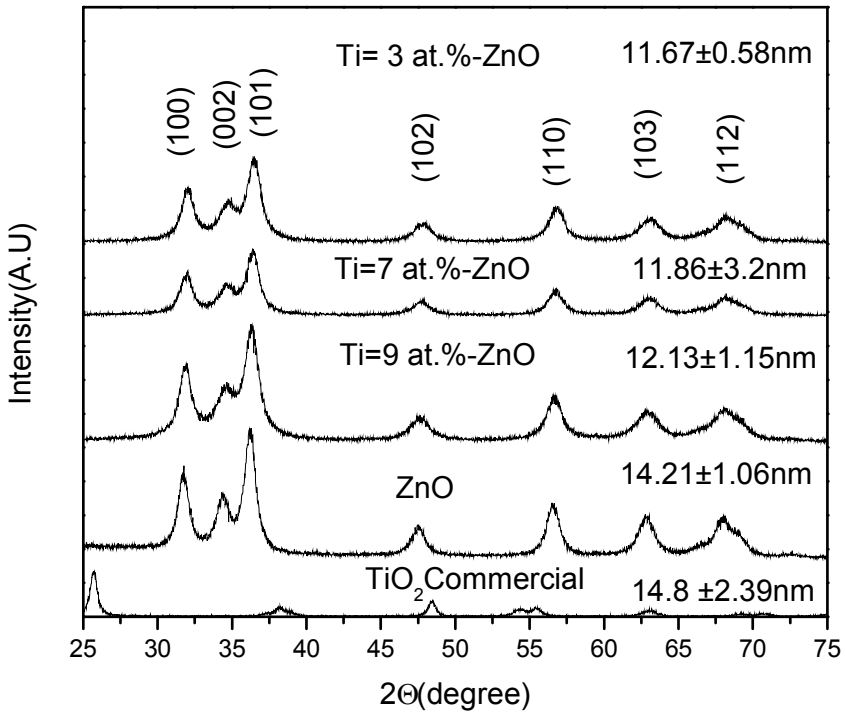

Figure 29. XRD patterns of pure and Ti-doped ZnO NPs synthesized by polyol method at different doping levels (at. %). The pattern for commercial TiO_2 is also included for comparison purposes.

The average crystallite size was estimated by using the Scherrer's equation and varied in the 14.2nm-11.7nm range. Also in this case, this estimation does not include the correction by the instrumental broadening. It became evident the decrease in the average crystallite size by Ti-doping. It can be considered that incorporation of Ti species into the ZnO lattice somehow inhibit the crystal growth stage probably due to some distortion in the ZnO unit cell. **Figure 30** shows the details of the diffraction peaks in the angular region 45° - 65°; a minor but noticeable shift of the XRD peaks towards larger 2θ values was observed, which suggested the incorporation of Ti^{4+} (ionic ratio 0.68 Å) into ZnO lattice (Zn^{2+} ionic ratio 0.74 Å) host producing the distortion in the lattice.

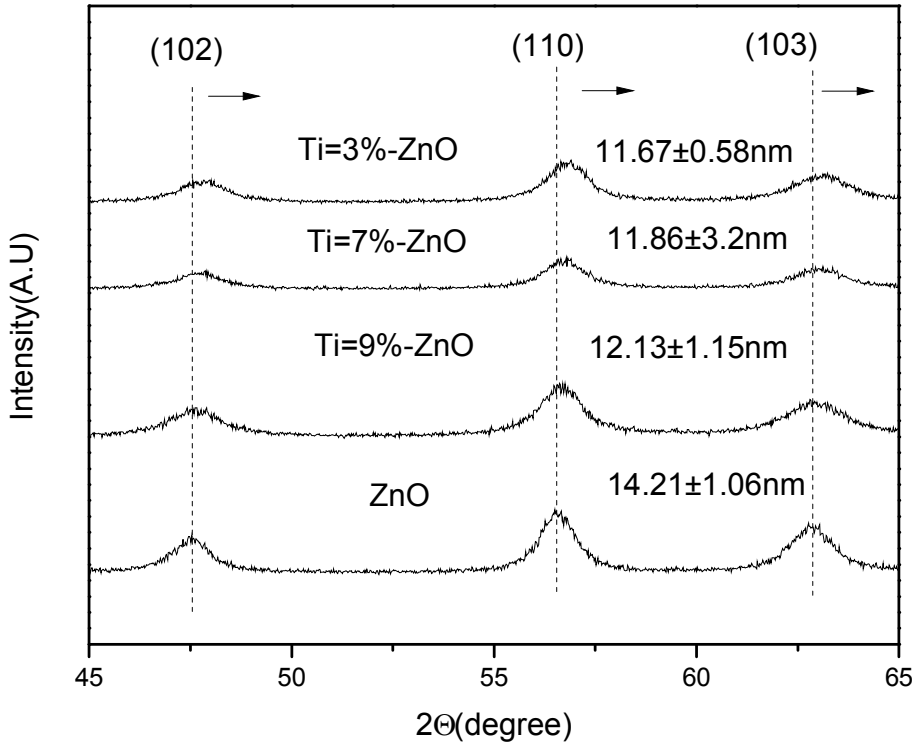

Figure 30. Detail of the XRD-patterns of pure and doped ZnO NPs in the region 45°≤ 2θ ≤ 65°. The shift of the XRD peaks in Ti-ZnO nanoparticles became evident.

Consequently, the observed XRD peaks shifts also suggest the variation of the lattice parameter values. In this regard, F**igure 31**. In addition to Zn ions substitution by Ti, smaller Ti^{4+} ions could also occupy interstitial sites in the ZnO lattice. These two events can explain the variation in the 'a' and 'c' parameter observed ion the mentioned figure.

A decrease in the lattice parameter values, with respect to pure ZnO, was observed when the Ti doping was at the 3% level; it could be due to the substitution effect of Ti^{4+} ion by Zn^{2+} that caused a compaction of the unit cell. The increase of the lattice parameters values at Ti concentrations higher than 3 at. % may indicate the expansion of the unit cell probably due the incorporation of Ti or Zn species in the interstitial sites.

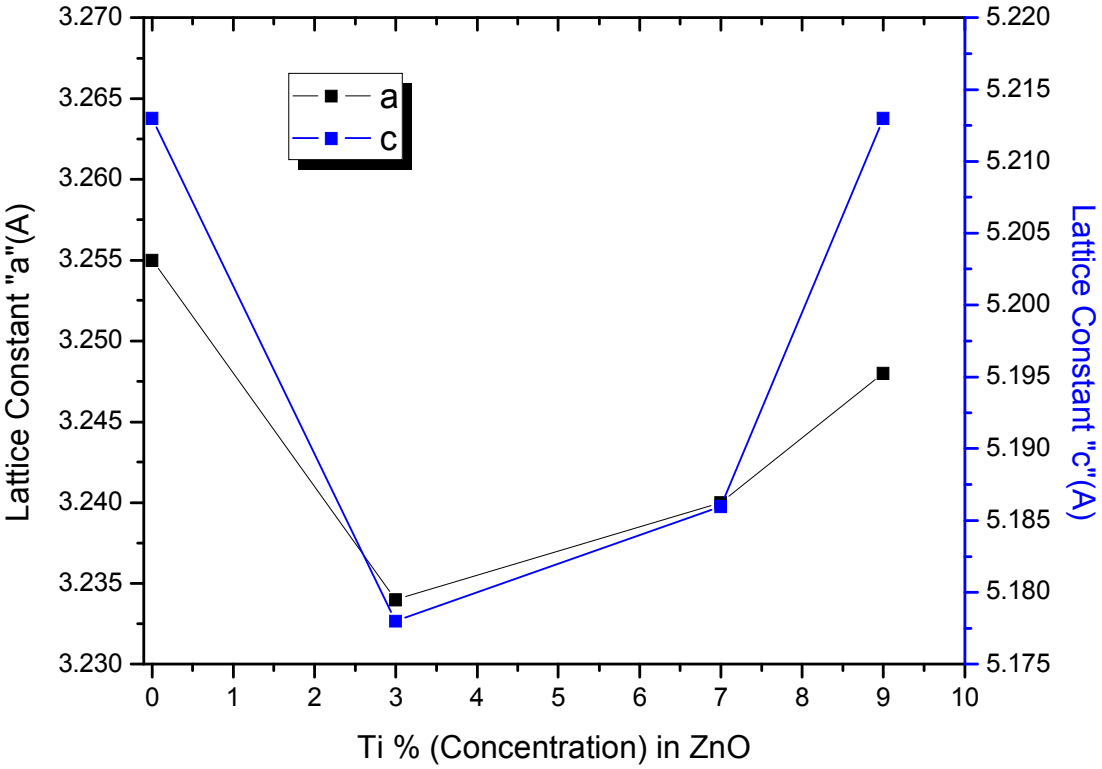

Figure 31. Variation in lattice parameters “a” and “c” as a function of Ti concentration in pure and Ti-ZnO NPs.

4.2.1.1.2. Fourier Transform Infrared Spectroscopy (FTIR)

The FTIR spectra corresponding to triethyleneglycol (TREG), TiO_2 NPs, pure and Ti-doped ZnO NPs, are presented in **Figure 32**. The weak band at 1630 cm^{-1} in pure and Ti-doped ZnO is attributed to the O-H bond in water. In turn, the bands at 1400 cm^{-1} and 1100 cm^{-1} are assigned to C–O vibration modes of the polyol functional group [203] and acetate groups absorbed on the surface of the NPs, respectively, which coincides with previous results [205]. The strong band at 554 cm^{-1} is characteristic of the Zn-O bond in the wurtzite structure. Those bands associated to polyol and acetate functional groups would be

related to the development of a negative surface charge that prevented excessive particle aggregation due to inter-particle electrostatic repulsive interaction.

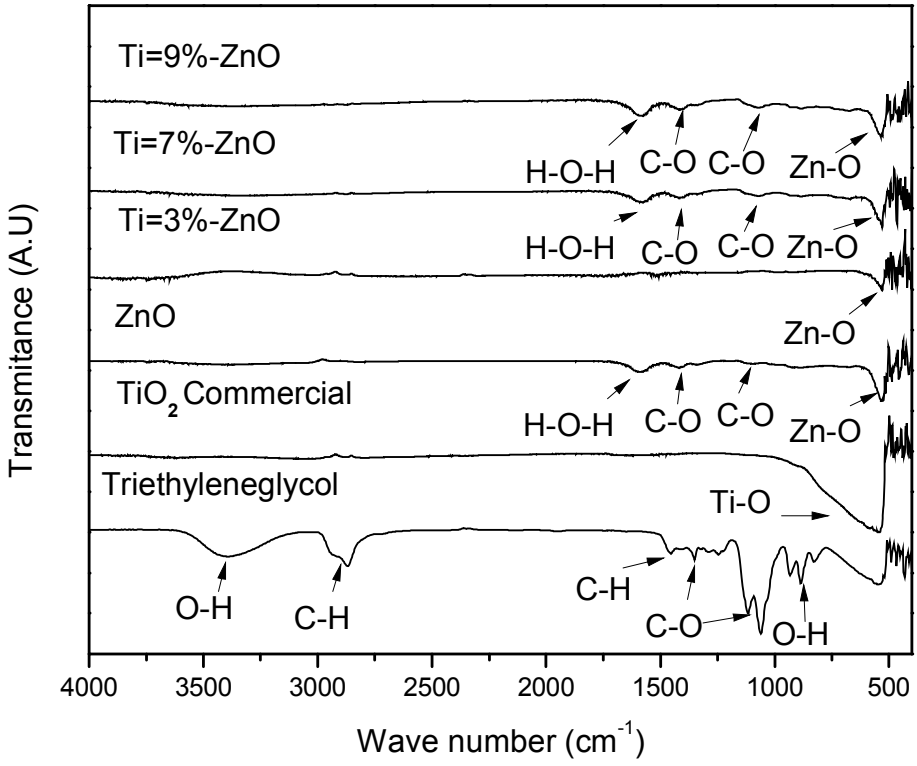

Figure 32. FTIR spectra of TREG, TiO_2 and pure and Ti-doped ZnO NPs.

4.2.1.1.3. Raman Spectroscopy

Figure 33 and 34 show the Raman spectra of the pure and Ti-ZnO NPs synthesized at different concentration of Ti species. The band at approximately 447cm^{-1} can be assigned to E_{2H} mode of ZnO, which corresponds at typical Raman mode of the hexagonal wurtzite structure. The optical mode centered on 571 cm^{-1} is attributed to structural defects in the lattice, e.g. oxygen vacancies or Zn interstitials [216]. The shift of the main vibrations modes can be attributed to the distortion in the lattice caused by the incorporation of dopant ions. Also, the enhanced intensity of the mode at 571 cm^{-1} may suggest the increase of the structural defects by Ti doping [217].

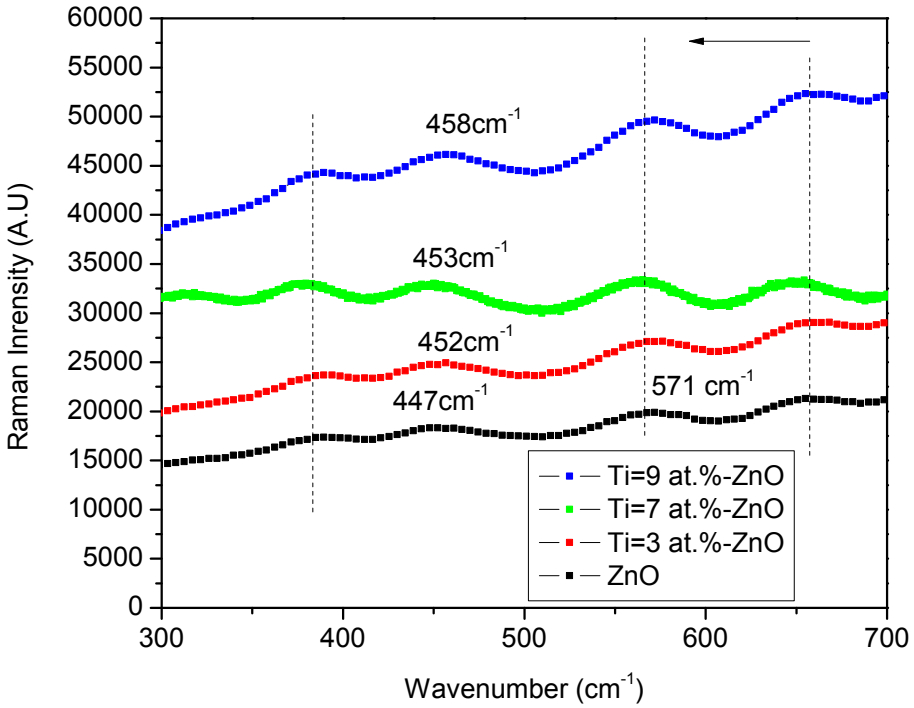

Figure 33. Room temperature Raman spectroscopy spectra of pure and Ti –doped ZnO NPs.

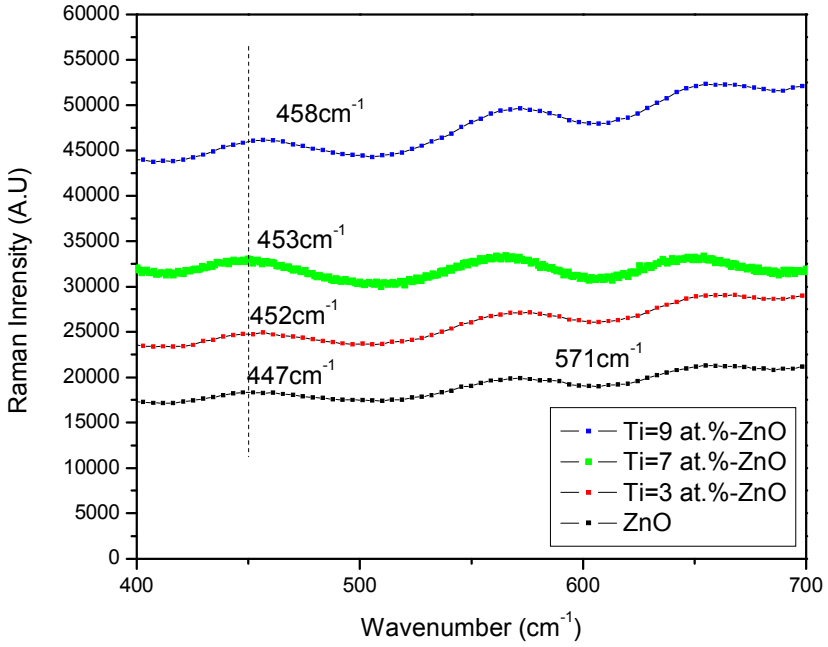

Figure 34. Detail of the Raman spectra of pure and doped ZnO NPs in the 400-700 cm^{-1} region

4.2.1. 2. Morphological property

4.2.1.2.1. Scanning Electronic Microscopy (SEM)

Figure 35 shows the SEM images of pure and Ti-doped ZnO. Figures 33(b- evidences the formation of spherical and highly monodisperse nanoparticles in the 100nm range. The fact that the SEM size is larger than the XRD one, would suggest the formation of polycrystalline primary particles containing tiny crystallites in the 11-15 nm range.

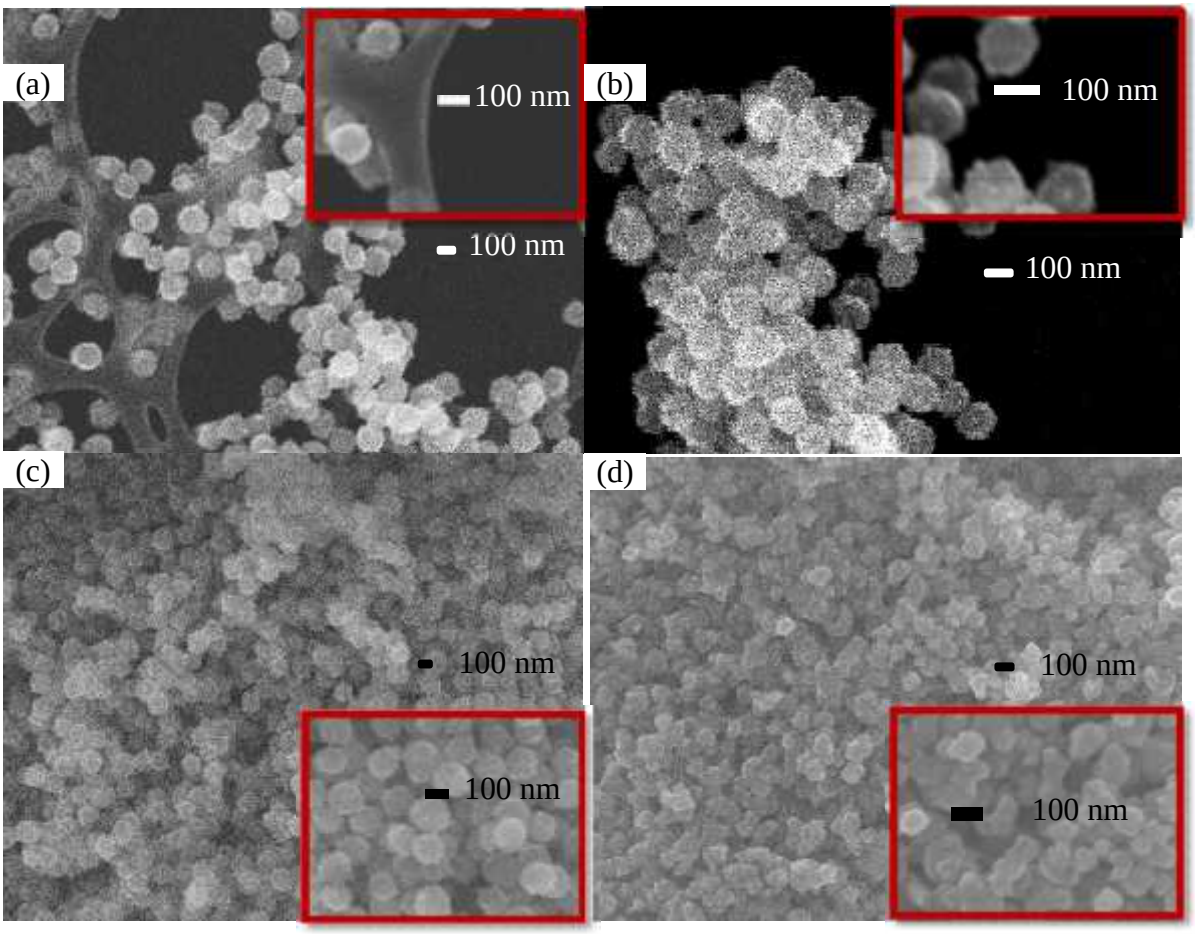

Figure 35. SEM images of the as-synthesized samples by polyol method: (a) ZnO NPs, (b) Ti= 3 at. % ZnO, (c) Ti=7 at. % ZnO and (d) Ti=9 at. % ZnO. The bar scale in the SEM images is 100 nm. The inset shows a magnification of each image.

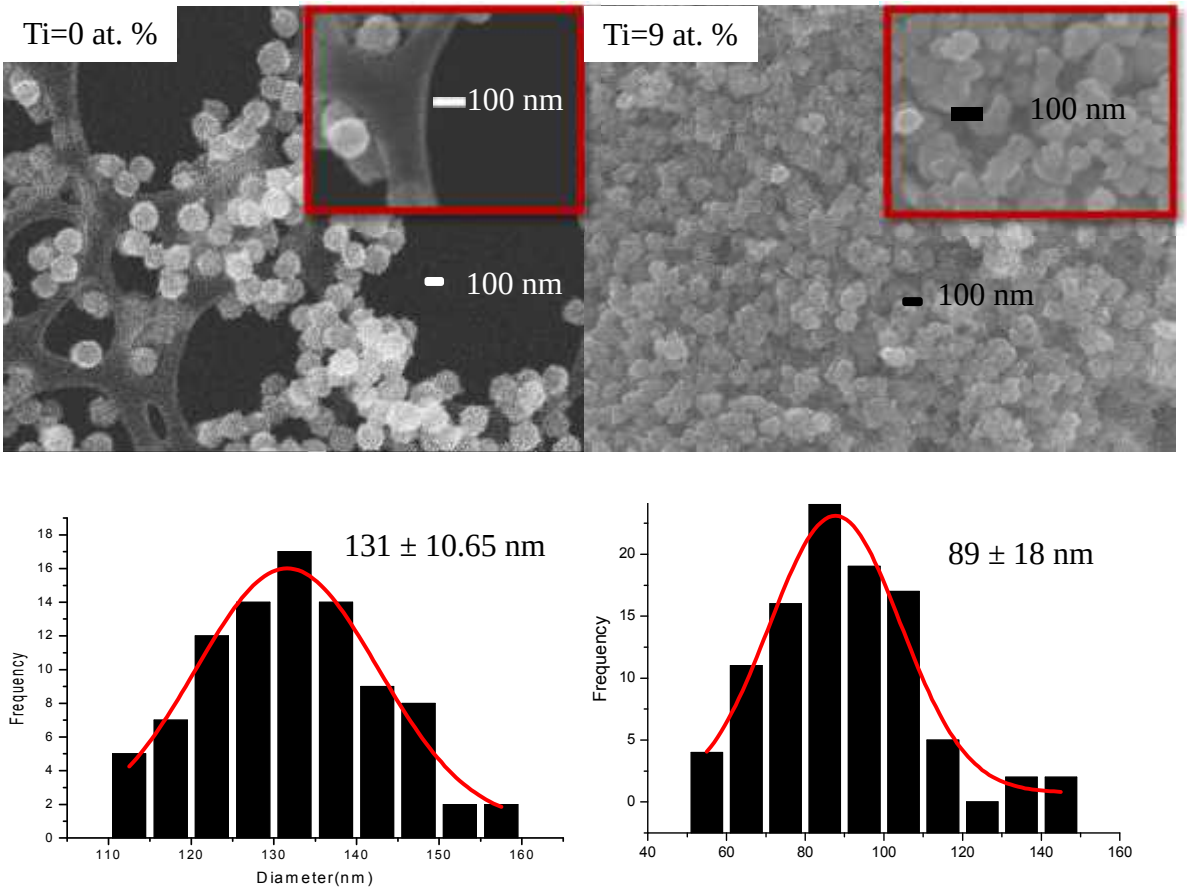

Figure 36. SEM images and size distributions of the as-synthesized samples by polyol method: (Top) ZnO NPs and Ti=9 at. % ZnO NPs and (bottom) their respective histogram of size. The inset shows a magnification of each image.

Figure 36 shows the image of pure ZnO and Ti= 9 at. %-ZnO NPs; the insets correspond to the magnification of the previous images. The particle size distributions have been calculated by analyzing the SEM images to get average particle size, to which the average particle size to Ti=9 at. %- ZnO is less than that of pure ZnO. As seen, an increase in the Ti concentration was conducive to the loss of the quasi-spherical shape in the particles; probably, the incorporation of Ti species would have affected the nucleation and growth rates associated with the terminal size of the particles, and the surface free energy of the particles that defines the equilibrium shape of each particle.

4.2.1.3 Optical Properties

4.2.1.3.1. Ultraviolet-Visible Spectroscopy Measurements

UV-Vis absorption spectra of pure and Ti-doped ZnO at different atomic percentage (at. %) of Ti are shown in **Figure 37**. All these samples exhibited a well-defined absorbance spectrum between 345-357 nm, which correspond to the exciton. UV-Vis absorption spectra show a shoulder around 357 nm that is characteristic of the excitonic peak of ZnO. This peak was blue shifted when ZnO was doped; it can be attributed to the size reduction of the NPs, which in turn will cause the band gap energy to increase. The small but noticeable increment of the band gap energy (from 3.28eV for pure ZnO up to 3.37 eV for Ti(3%)-ZnO), estimated by using Tauc's relationship, supports this interpretation.

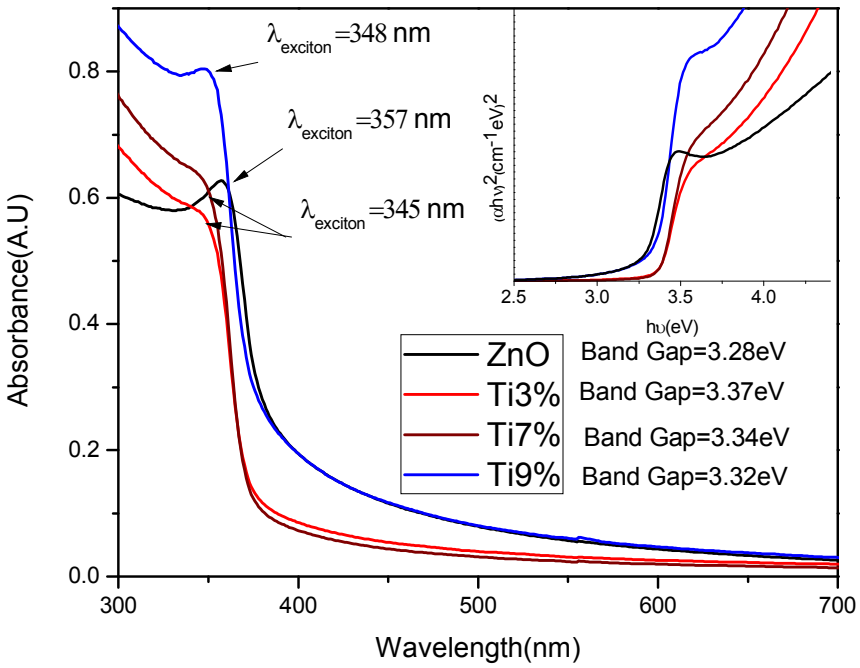

Figure 37. UV-vis spectra and Optical Band Gap determination (upper inset) for pure and Ti-doped ZnO. The exciton was blue-shifted with the incorporation of Ti species. The estimated band gap varied from 3.28 (pure ZnO)-3.37 eV (Ti-ZnO).

4.2.1.3.2. Photoluminescence Spectroscopy Measurements

Room temperature PL measurements were carried out with an excitation wavelength of 345nm (**Figure 38)**. The spectra look very similar with the presence of two strong emission peaks; the PL emission peaks centered on 361nm and 390 nm are attributed to the exciton emission and transition of shallow donor levels near of the conduction band to valence band, respectively. According to Chen's [218] work on thin films, the incorporation of Ti^{4+} ions would lead to an increase of the concentration of interstitial Zn. On this basis, it can be suggested a similar effect in the Ti-ZnO NPs; the incorporation of Ti species should have fostered the increase of defects of the interstitial Zn type associated to the 390nm emission peak.

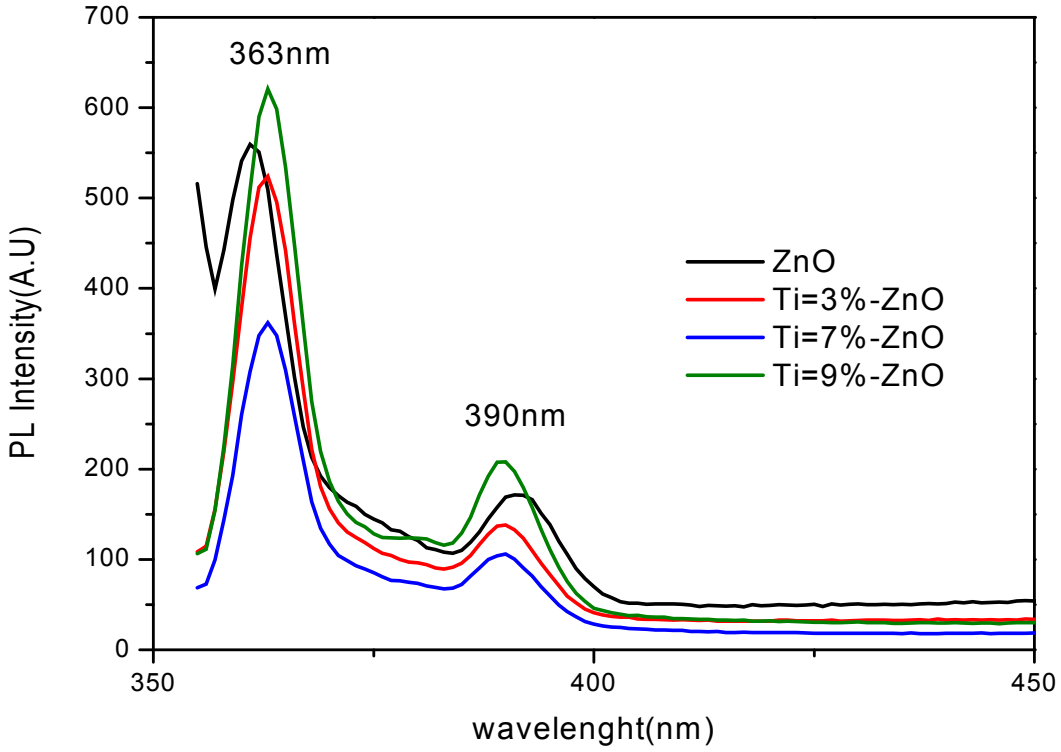

Figure 38. PL Spectra of pure ZnO and Ti-ZnO NPs, under an excitation wavelength of 345 nm. Doping could have enhanced the intensity of the main emission peak (363nm) as well as increased the intensity of the band around 390 nm associated with interstitials defects.

In order to improve the discussion level, it is always better to compare the variation in the relative intensities of these two emission peaks. For this purpose, the variation in the intensity ratio of these 2 peaks (I_{363}/I_{390}) with the level of Ti doping is presented in **Figure 39**. For pure ZnO this ratio was around 3.3 and was increased up to 3.8 for Ti (3%)-ZnO. This trend may suggest the promotion of the recombination processes associated to the 363nm emission peak by the substitution of Zn^{2+} ions by Ti^{4+} ions in the host lattice. This ratio decreases when the concentration of Ti is above 3%, suggesting that the 390nm peak intensity started to increase with respect to the one at 360nm. This relative increment in the 390nm peak intensity may suggest the increase of the concentration of trap states associated to the incorporation of Zn^{2+} in interstitials sites (zinc interstitials). The promotion of the generation of these kind of defects is pretty important since they should favor the mechanisms related to the generation of singlet oxygen (SO) when we irradiate this material with a suitable source of light.

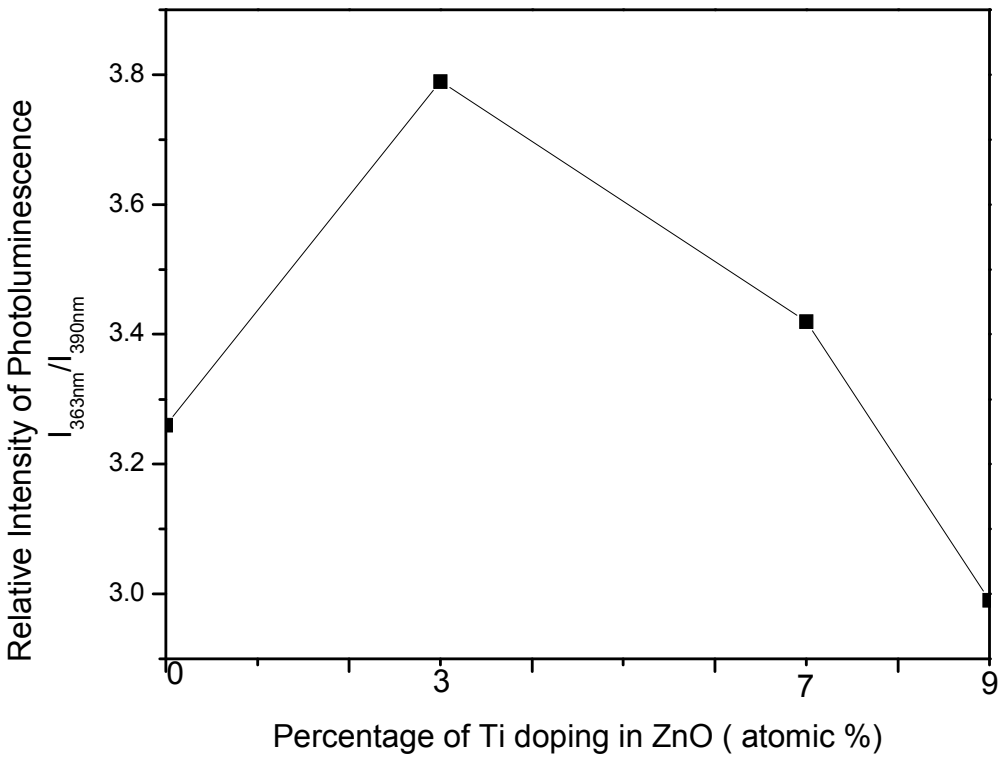

Figure 39. Variation of the ratio between the intensity at 363nm and 390nm ratio for pure and Ti-doped ZnO NPs.

Concluding Remarks

ZnO doped with Ti in the 3-9 at. % range was successfully synthesized using the modified version of the polyol process. XRD measurements confirmed the development of well-crystallized Wurtzite-ZnO structure with an average crystallite sizes ranging between 11 and 15 nm. A slight shift of the diffraction peaks in doped samples suggests the incorporation of Ti species in the oxide host.

Infrared spectroscopy measurements confirmed the chemical structure of the ZnO and also the presence of functional groups associated to polyol and acetate compounds. These surface groups may have induced the development of a negative surface charge that may have prevented particles from excessive aggregation explaining the monodispersity in our synthesized samples. SEM images confirmed the particles monodispersity and also revealed that doping with Ti caused a decrease in the particle size. Additionally, Raman spectroscopy confirmed the hexagonal wurtzite structure and verified the effect of Ti doping on the increment of structural defects in the ZnO host.

UV-Vis spectroscopy evidenced the typical excitonic peak of ZnO that was blue shifted by Ti incorporation in the oxide lattice. This shift can be attributed to the crystal size reduction and the incorporation of Ti ions in the ZnO structure. The small but noticeable increment of the band gap energy, estimated by using Tauc's relationship, supported this interpretation. Photoluminescence measurements revealed the strong effect of Ti doping on the relative intensity ratio of the emission peaks at 363nm and 390nm. It is suggested that the incorporation of Ti species into the ZnO structure would favor the increase of structural defects of the types trap states and zinc interstitials.

4.2.2. Effect of dopant level in Li-doped ZnO nanoparticles

4.2.2. 1. Structural Characterization

4.2.2.1.1. X-Ray Diffraction (XRD)

Figure 40 shows the XRD patterns of Li-ZnO (Li = 0, 3 and 5 at. %) powders. All diffraction peaks belong to the ZnO wurtzite structure [149]. The well-defined diffraction peaks suggested the samples have good crystallinity without the presence of isolated secondary phases, even in presence of the dopant species. Also, a slight displacement of the peaks towards greater 2θ values was observed that can be attributed to cell distortion caused by Li incorporation into the ZnO lattice.

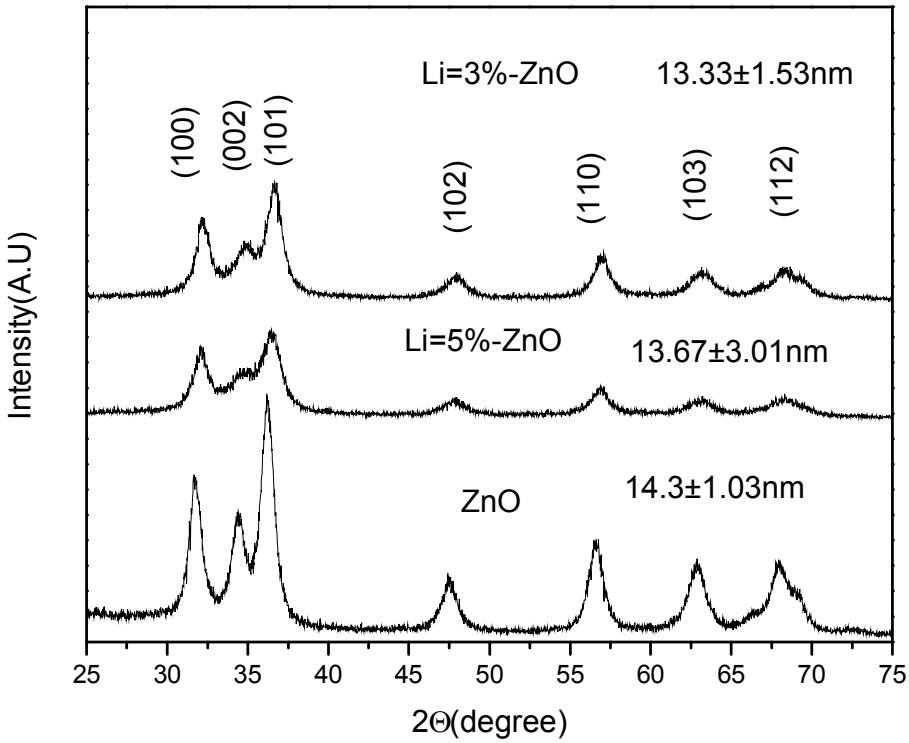

Figure 40. XRD patterns of pure and doped ZnO synthesized at different Ti-doping levels.

Figure 41 shows the detail of the XRD patterns in the 45°-65° range. The diffraction angles were slightly shifted that can be due to the actual incorporation of Li in the oxide host structure. Li^{+1} ionic radius (0.60Å) is quite small compared with Zn^{+2} ion (0.74 Å) and could easily enter the structure of ZnO; this feature will cause a contraction of

the unit cell and the corresponding shift of the diffraction peaks towards large 2θ values. The slight increase of the peaks broadening with doping suggests the reduction of the average crystallite size. The estimated average crystallites sizes varied in the 14.3nm-13.3nm range.

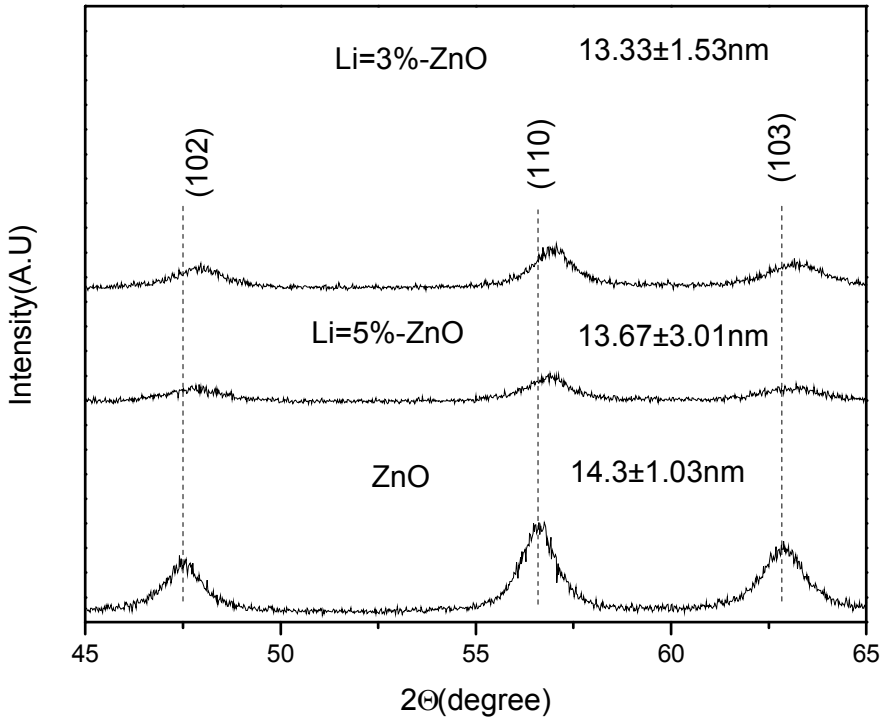

Figure 41. Detail of the XRD-patterns of pure and Li - doped ZnO NPs in the region 45°≤ 2θ≤65° . The dash line is a guide to the eyes to observe the shift in the diffraction peaks.

Generally speaking, and as **Figure 42** evidences, the decrease in the values of the lattice parameters with Li doping (a=3.25-3.22Å and to c=5.21-5.16Å) may be indicative of the contraction of the unit cell due to the incorporation of small Li species substituting the larger Zn species.

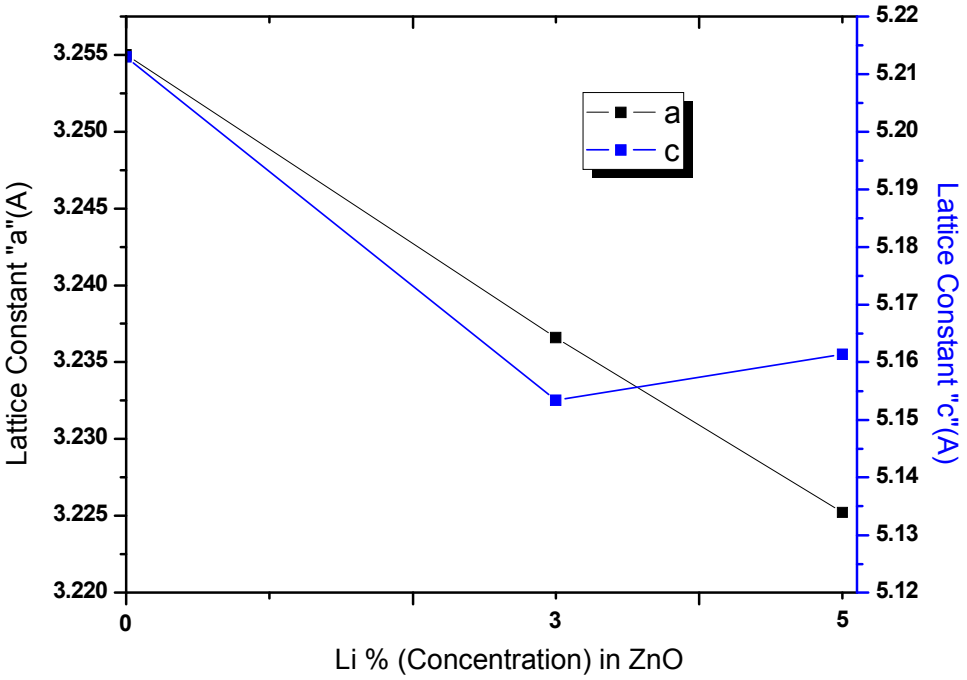

Figure 42. variation of the lattice parameters “a” and “c” as a function of Li content in pure and Li-ZnO NPs.

4.2.2.1.2. Fourier Transform Infrared Spectroscopy (FTIR)

The weak band at 1630 cm^{-1} can be assigned to H-O-H bending vibrations due to the presence of some amount of water adsorbed from the environment. Meanwhile, bands around of 1400 cm^{-1} and 1100 cm^{-1} can be assigned to C–O vibration modes from the polyol or acetate groups [203]. In turn, the intense band at 554 cm^{-1} is typical of the Zn-O stretching vibration modes in ZnO. Despite, incorporation of Li into ZnO host lattice not observed any additional band associated with isolated Li-phases.

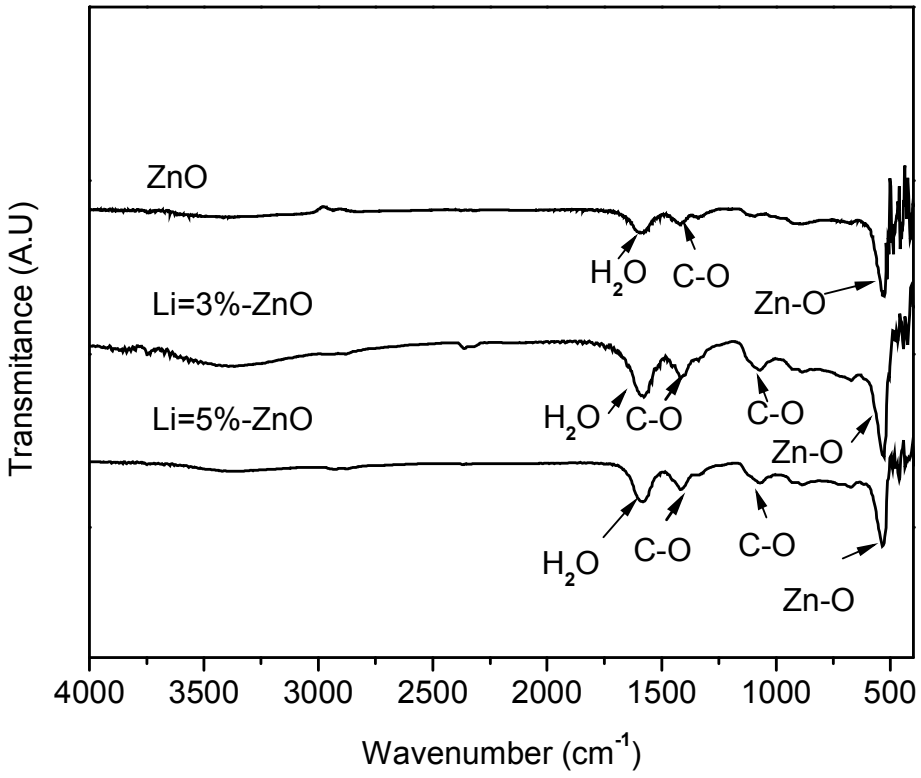

Figure 43. FTIR spectra of pure and Li-doped ZnO NPs synthesized at different Li concentrations.

4.2.2.1.3. Raman Spectroscopy Measurements

All measurements were done at room temperature with an excitation wavelength of 638nm. The 447cm^{-1} vibration mode, associated to the wurtzite crystal structure, was shifted towards higher wavenumbers in presence of Li dopant. It can be attributed to the distortion (contraction) of the lattice due to the substitution of large Zn by small Li ions. This vibration mode can also be related to vibration of oxygen atoms; therefore, the observed shift would indicate that oxygen atoms vibrate with more energy due to the presence of substituting Li species. Besides, the increase in the intensity of the band at 571 cm^{-1}, which is associated to defects (V_O and Zn_i), may suggest the increase of the structural defects by Li doping. Finally, vibration modes localized at 393cm^{-1} and 655cm^{-1} associated with A_1(TO) mode, [207], and mode intrinsic of ZnO, (TA+ LO modes) [208], did not evidence any change by incorporation of Li species.

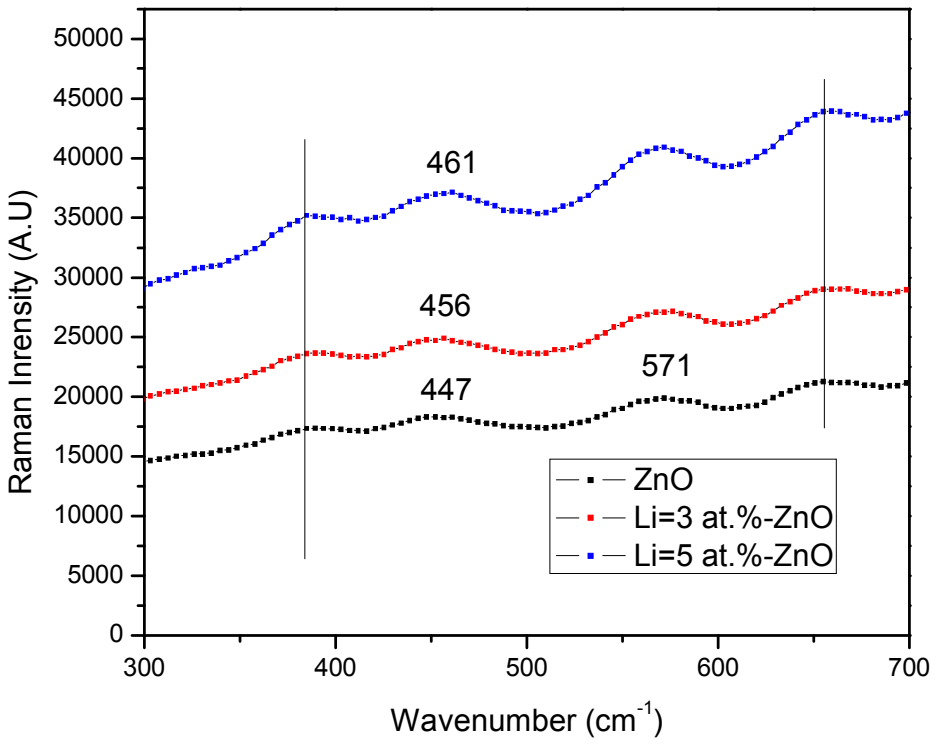

Figure 44. Room temperature Raman spectroscopy spectra of Li –doped ZnO NPs for different concentrations of Li.

4.2.2. 2. Morphological property

4.2.2.2.1. Scanning Electron Microscopy (SEM)

Figure 45 shows the surface morphology of pure and Li-doped ZnO NPs. Both ZnO and Li= 3 at. % -ZnO NPs consisted of quasi-spherical particles (**Figure 45-a and b**) with a size around of 100 -130 nm. Higher Li concentrations affected the particle shape and monodispersity; agglomerated individuals were observed. However, all particles are still in the 100nm range that is still suitable for the envisioned PDT applications.

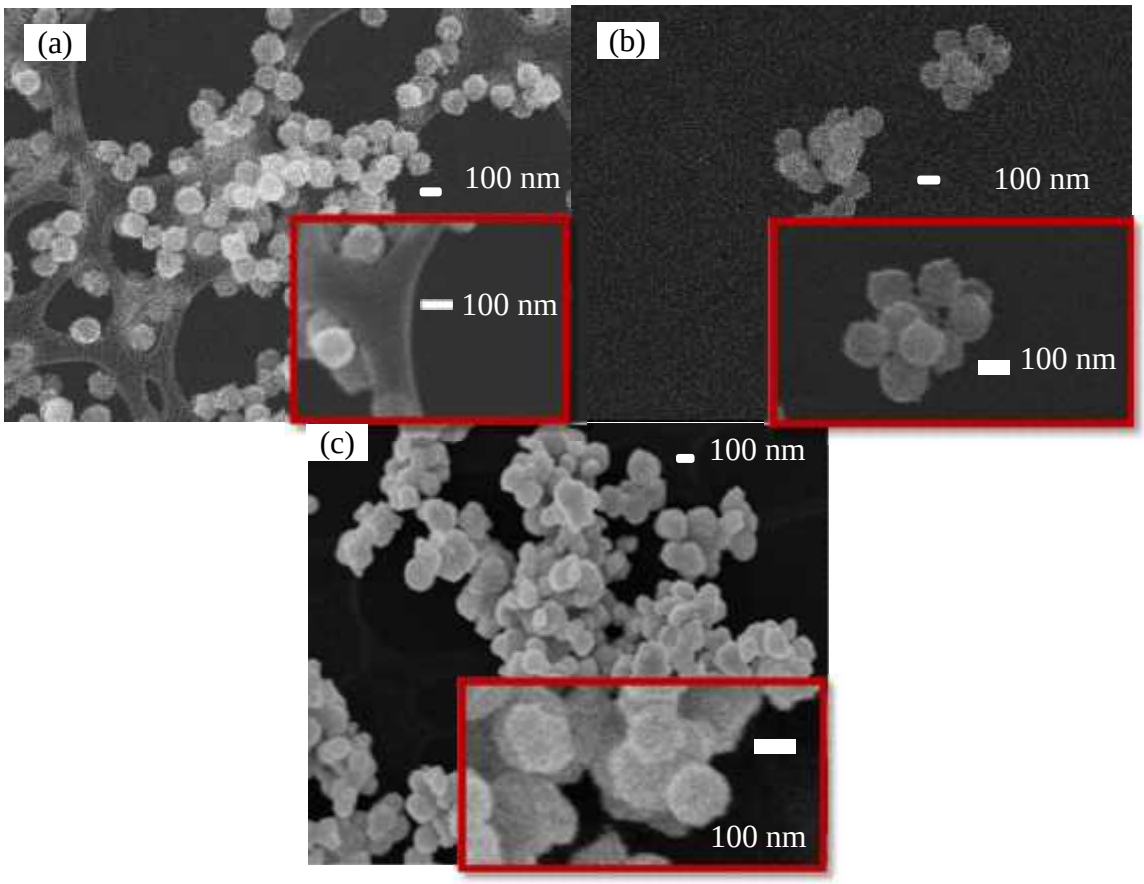

Figure 45. SEM images of samples synthesized: (a) ZnO NPs, (b) Li=3 at. % -ZnO NPs and (c) Li=5 at. %-ZnO NPs. After the incorporation of Li= 5 at. % into ZnO the shapes of the NPs changed from quasi-spherical monodisperse to irregular and polydisperse ones.

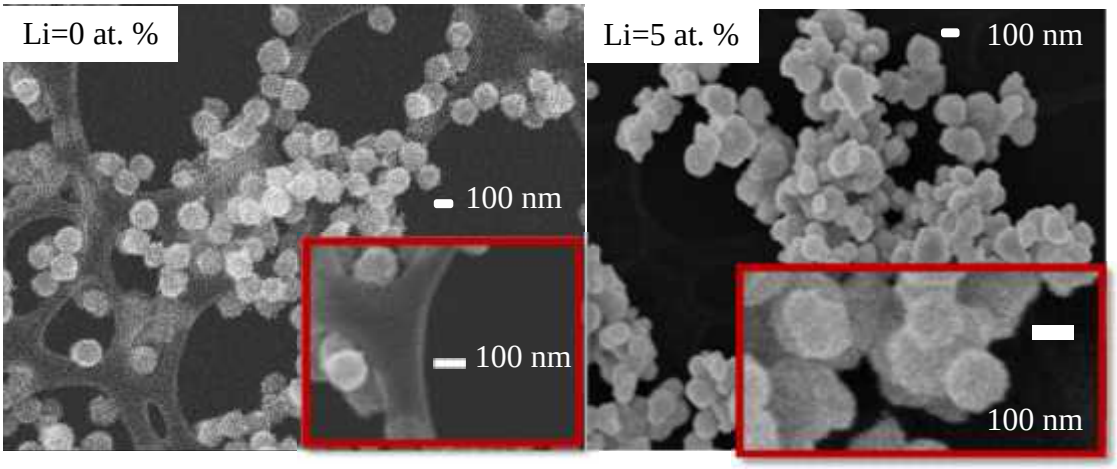

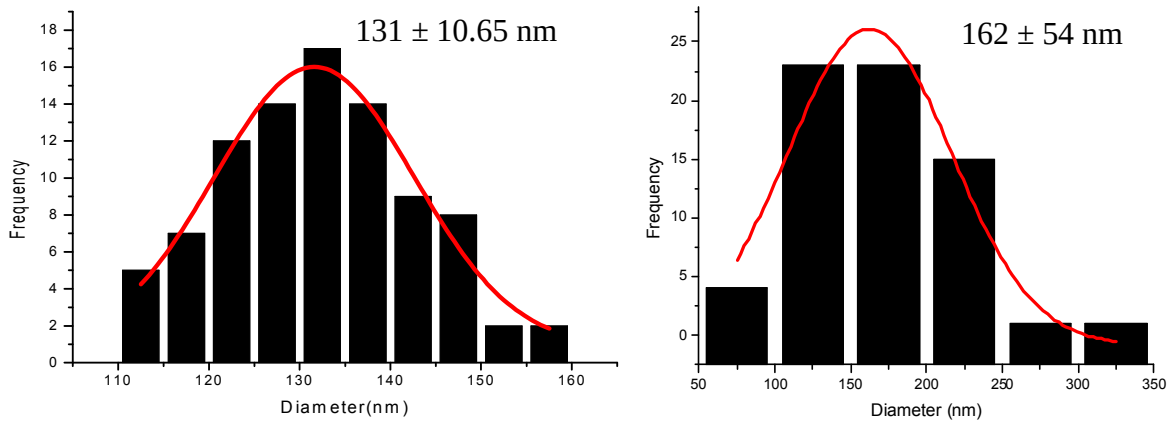

Figure 46. SEM images and size distributions of the as-synthesized samples by polyol method: (Top) ZnO NPs and Li=5 at. % ZnO (bottom).

4.2.2.3 Optical Properties

4.2.2.3.1. Absorbance (UV-Vis Spectroscopy)

Figure 47 shows the UV-vis absorption spectra of all samples synthesized at different Li-doping levels. The UV-Vis spectra clearly revealed the exciton peak in the 347 nm-360 nm range. The exciton was slightly blue-shifted by doping, which could be attributed to the particle size reduction, although SEM analyses did not support this interpretation. However, the broad particle size distribution in Li-ZnO NPs could be related to this trend; smaller sizes would be responsible of the blue shift in Li (5 at. %)-ZnO samples. exp. but is not evidenced to this case due to discrepancy of the size obtained by SEM. The corresponding band gap energy values, which were estimated by using Tauc's relationship [219], are very similar and varied in the 3.27-3.30 eV.

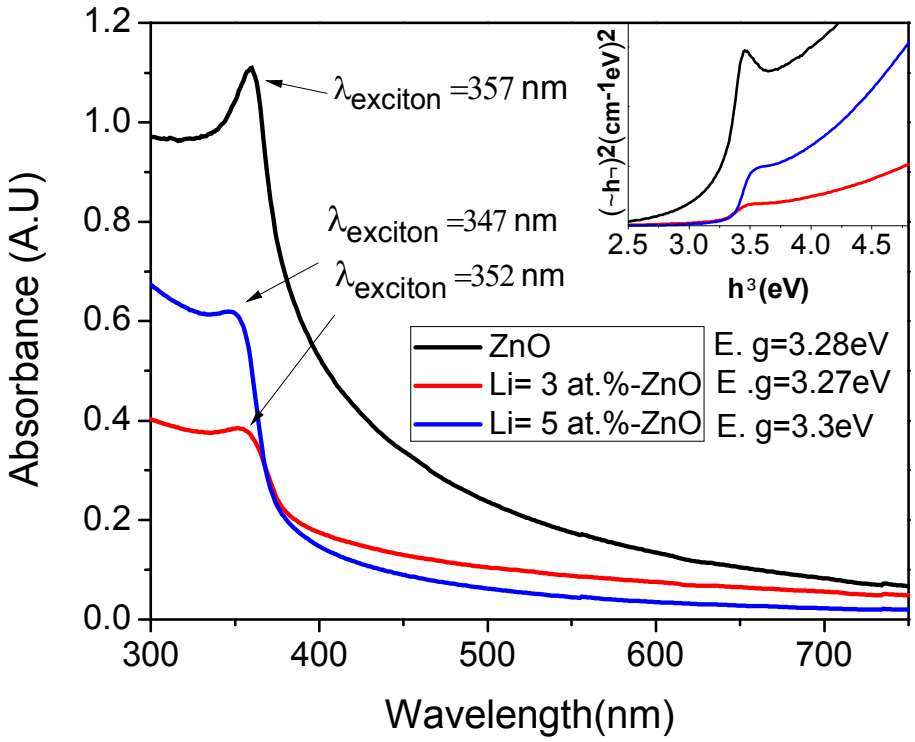

Figure 47. UV-Vis spectra for pure and Li doped ZnO. The exciton was slightly blue-shifted with the incorporation of Li species. The estimated band gap energy (E.g.) varied in the 3.28-3.3 eV range.

4.2.2.3.2. Photoluminescence Spectroscopy

Figure 48 shows the PL Spectra of pure ZnO and Li doped-ZnO NPs for an excitation wavelength of 345 nm. Three peaks centered on 363nm, 390nm and 556 nm were observed. Two prominent bands are clearly observed: one in the ultraviolet region at 363nm and the other at 390 nm. The emission peak at 363 nm is associated by the recombination of free exciton transition from the localized level bottom of the conduction band to the valence band, whereas the emission peak at 390 nm is attributed to the presence of Zn interstitials where the electron makes a transition from this interstitial level to the top of valence band or trap states. The increased PL intensity at 556 nm suggests the presence of oxygen vacancies that could have been promoted due to the incorporation of Li+ (i.e. for each 2 Li^{+} ions entering into the oxide lattice, two Zn^{2+} and one O_2^{-} should leave the

structure).

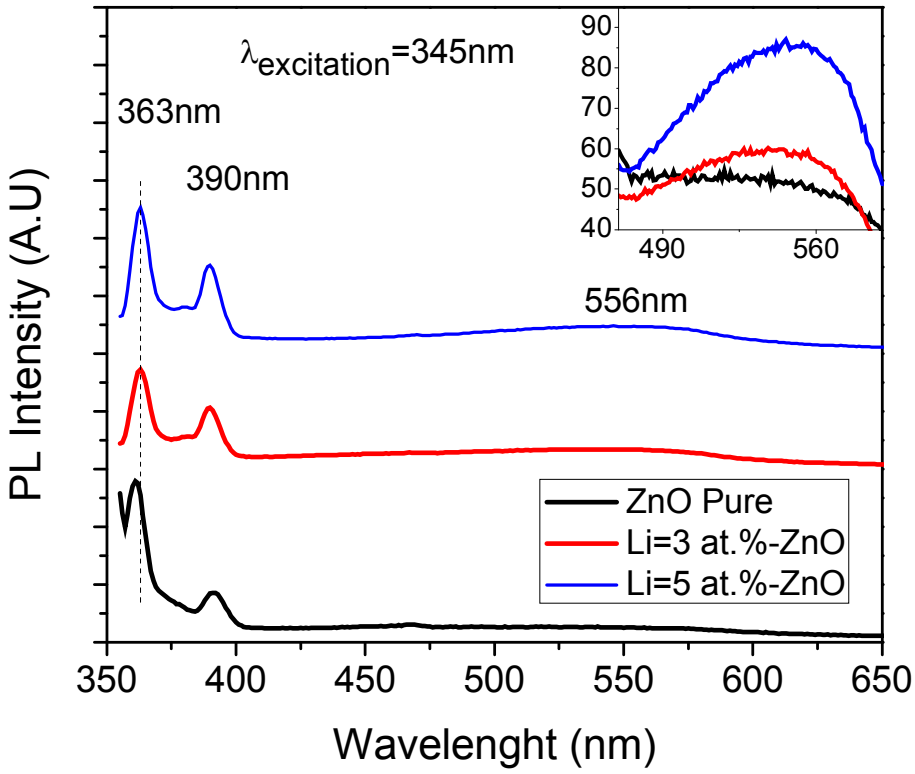

Figure 48. PL Spectra of pure and Li-doped ZnO NPs. The inset shows the PL spectra in the green region (around 550 nm).

In order to assess better, the information provided by PL measurements, the intensity ratio for those 2 peaks (I_{390nm}/I_{363nm}) was plotted as a function of the dopant level (**Figure 49**). The increase of this ratio in the 0-5 at % Li range indicates the relative increase of the 390nm-peak intensity, with respect to the 363 nm one, that could be attributed to the increase of the concentration of trap states or zinc interstitials defects. In turn, because of the relatively small size of Li^+ species and its compatibility with interstitials size in the hexagonal ZnO lattice, the interstitial incorporation of Li^+ species cannot be ruled out [220].

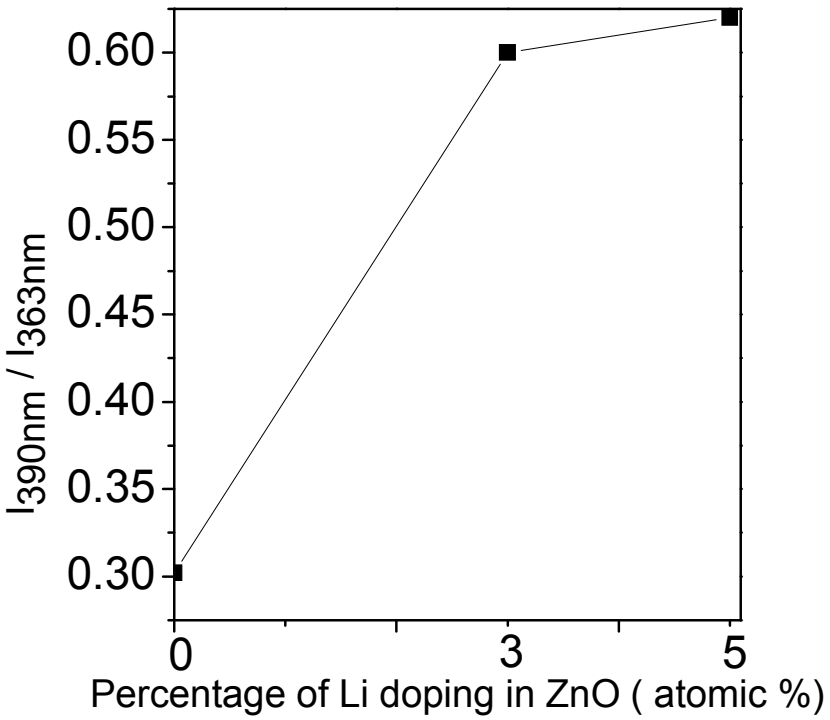

Figure 49. Variation of the relative intensity I_{390nm}/I_{363nm} with the level of Li doping.

Concluding Remarks

Li-doped ZnO NPs (Li = 0 at. %, 0.03 at. % and 0.05 at. %) were successfully synthesized by our modified version of the polyol method. Synthesized NPs exhibited a ZnO Wurtzite structure without secondary phases according to XRD measurements. The average crystallite sizes ranged between 13.3nm and 14.3 nm. Raman spectroscopy measurements corroborated the formation of wurtzite structure and also evidenced the increment of structural defects by the incorporation of Li^{1+} ions into the ZnO host lattice. Meanwhile, FTIR spectroscopy reveals a suitable chemical stability of pure and Li-doped ZnO NPs.

UV-Vis measurements evidenced a clear blue shift of the exciton peak with Li doping, which was attributed to the change in NPs size. The corresponding band gap energy values, estimated from UV-vis measurements, decreased from 3.33 to 3.27 eV. On the other hand, the observed increase in the emission intensity of the 390 nm emission peak, relative

to the intensity of the main emission peak at 363nm, was attributed to the promotion of trap states due to interstitial Zn or Li-incorporation into the host oxide lattice. The emission at 556 nm increased for all the doped samples suggesting that increment of these band could be due rise in oxygen vacancies promoted for the substitution of Li $^{1+}$ by Zn $^{2+}$ ions.

4.3 Singlet Oxygen (SO) Generation

4.3.1. SO Generation by Pure and Ti-doped ZnO Nanoparticles

As described in the experimental section of this work, the generation of SO was detected using a sensor green kit. This method is based on the increase in fluorescence intensity of the fluorescent DMAX-endoperoxide at 525nm under illumination by a light of 488 nm was used. This fluorescent compound is formed only after the original DMAX react with SO; in other words, the more intense the signal at 525nm the larger the generation of SO. As **Figure 50** shows, a very clear increase in the intensity of the 525nm peak was attained even I presence of ZnO alone; the photo-excitation of ZnO due to the presence of interstitial defect, could be related to its capability to produced SO.

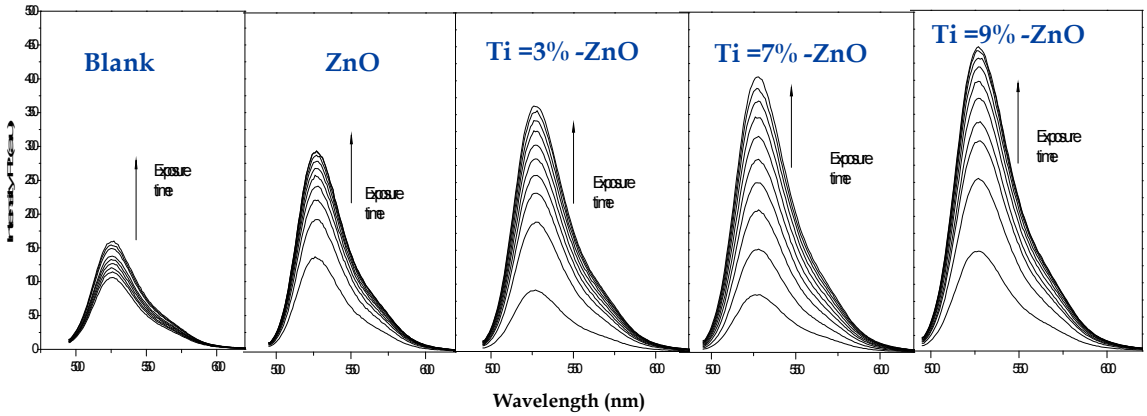

Figure 50. PL spectra of the SO-sensor green irradiated by UV light (blank), and in presence of pure ZnO and Ti-doped ZnO nanocrystals. The enhancement on the emission intensity at 525nm in presence of doped ZnO evidenced the improved generation of SO by Ti doping

This 525nm intensity was increased even further, meaning an enhanced generation of SO, when ZnO was doped by Ti species. This rise in the generation of SO can be

attributed to the promotion of Zn interstitials concentration and trap states in ZnO, as suggested by PL measurements.

In order to visualize better the net effect of Ti on the capacity of doped ZnO to generate SO, the intensity of the 525nm emission peak for the blank (UV illuminated sensor green only) was subtracted to the same signal but in presence of the NPs **(Figure 51).** From these results, a faster and large generation of ZnO at higher Ti doping levels became evident. Therefore, the sample with high concentration of Ti (9 at. %) was the most effective to generate SO. Also, these results would suggest that ZnO-based NPs can be considered as a convenient Photosensitizer, i.e. a direct generator of SO.

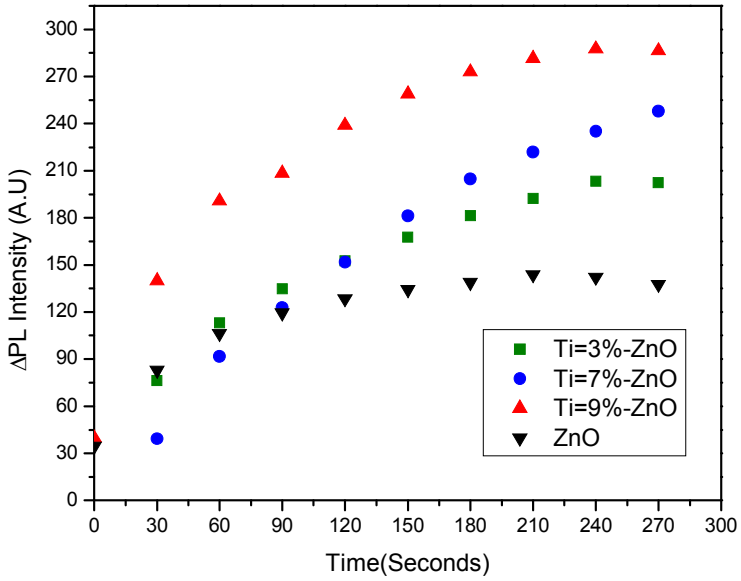

Figure 51. Net increase of PL intensity of SO with pure and Ti - doped ZnO NPs as a function of the exposure time under UV light.

4.3.2. SO Generation by Pure and Li-doped ZnO Nanoparticles

Also in this case, the increment of the emission peak at 525nm was associated to the generation of SO species. **Figure 52** shows the variation with UV-irradiation time of the blank, pure ZnO and Li-ZnO NPs. Each emission was recorded at 30 seconds interval. The maximum concentration of Li used in these measurements was 0.049 mg /L, which is below its toxicity limit. In turn, the net variation of the 525 nm-emission peak intensity with irradiation time is summarized by **Figure 53.** Evidently, Li=5 at. %-ZnO shows greater UV induced generation of SO than pure ZnO and a higher rate. These results can be attributed to the formation of structural, defects such as interstitial zinc (trap states), promoted by the incorporation of Li ions into the ZnO structure. As noted, the addition of Li promoted the generation of SO species, a fact that can be explained in terms of the increase of those structural defects involved with the inter-systemic crossing and subsequent energy transfer to molecular oxygen to give SO species.

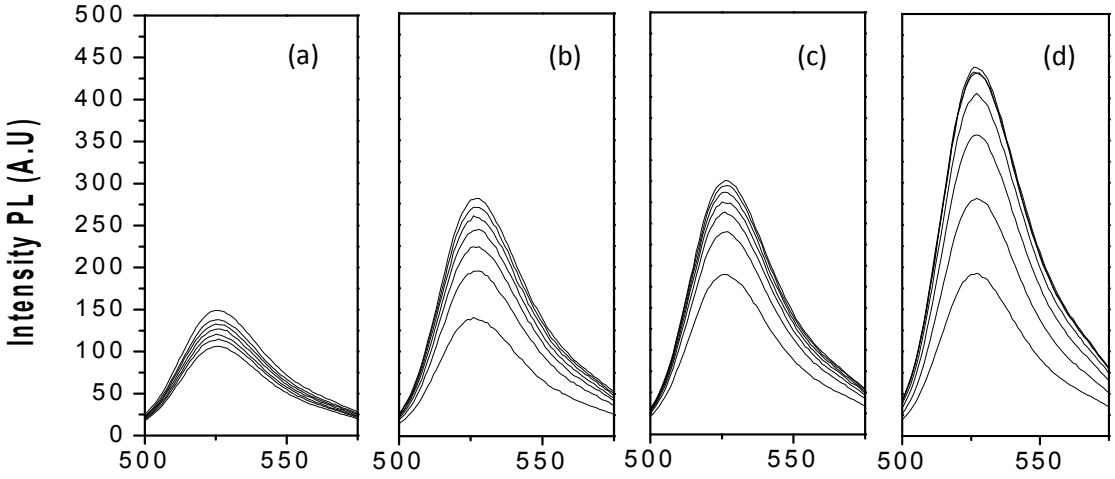

Figure 52. PL Spectra of: (a) Singlet oxygen sensor green without NPs (Blank); (b) pure ZnO; (c) Li=3 at%- doped ZnO; and (d) Li=5 at%-doped ZnO irradiated by UV light ($\lambda_{excitation}$: 345 nm) as a function of irradiation time (IT). The NPs concentration was 11.11 mg/L.

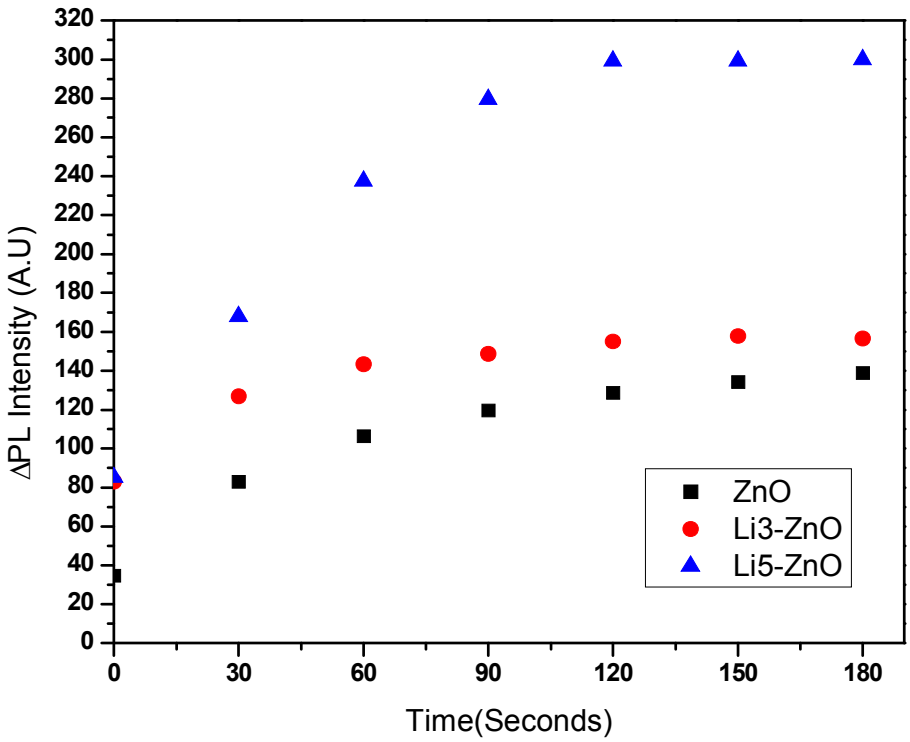

Figure 53. Net increase of the emission intensity of the 525nm peak, associated to SO generation, in pure and Li (3, and 5 at. %) – doped ZnO NPs, as a function of the exposure time to UV light.

Concluding

The incorporation of Ti in ZnO structure favors the increase of the concentration of structural defects in ZnO (trap states and zinc interstitials), which in turn could explain the enhanced generation of SO. As observed, the greater the incorporation of Li in ZnO the larger the enhancement of the 525 nm-emission peak intensity, ie. The larger the generation of SO. This enhanced generation of SO by Li doping would be a consequence to the promotion of Zn or Li interstitials concentration in the ZnO structure, as suggested by PL measurements. These defects would favor the presence of triplet or trap states in the oxide structure that are necessary for SO formation. Accordingly, the increased generation of SO by the Li-doped material enable Li-doped ZnO NPs to be considered as a direct Photosensitizer.

4.4. Two-photon Fluorescence Microscopy (TPFM)

As-synthesized all NPs were excited using TPFM equipped with a 690nm laser (700 mW) with a light pulse of 140 fs and 80 MHz repetition rate. Emitted light was collected between 400-600 nm, due to the fact that no PL signal was found outside this range. The data was collected at intervals of 3 nm.

4.4.1. Photoluminescence of ZnO Nanoparticles

The TPFM spectrum corresponding to pure ZnO NPs is presented in **Figure 54**. The spectrum evidenced the presence of a high emission peak in the green region (555 nm) that was assigned to oxygen vacancies, V_O [155]. Also, a weak but noticeable peak at 420 nm was detected, which is attributed to electron transition from the shallow donor level of Zn_i to the valence band [222]. This behavior in photoluminescence excited by two photons is characteristic of a non-linear process, which in turn is related to those nanomaterials that exhibit non-centrosymmetric crystal structures (i.e. lacks inversion symmetry). ZnO has not centrosymmetric crystal structure due to the tetrahedral coordination between O^{2-} and Zn^{2+} ions in the oxide lattice [156, 224].

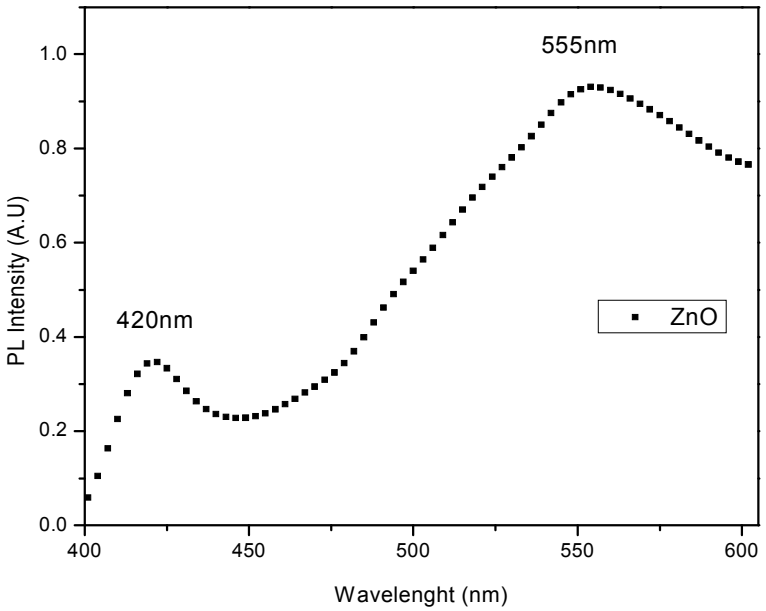

Figure 54. Normalized two photons-PL spectrum of pure ZnO NPs excited at 690 nm.

4.4.2 Photoluminescence of Ti-doped ZnO Nanoparticles

As-synthesized pure and Ti= 9 at. %-ZnO NPs were excited using TPFM with 690nm-light. The spectra, shown in **Figure 55,** revealed a high emission band in the green region (555 nm) and a weak one at 420 nm that were assigned to oxygen vacancies, V_O, and interstitial Zn, Zn_i, respectively. The increment of the intensity in the PL band at 555 nm, with respect to pure ZnO, could be due to the enhanced formation of oxygen vacancies by Ti^{4+} substitution of Zn^{2+} sites. The sharpening of the emission peaks, especially the one at 420 nm, can be attributed to the high monodispersity of the pure ZnO NPs compared to the Ti-doped ones. **Figure 56** graphically shows the variation in the relative intensity of the peaks at 55nm with respect to the one at 420 nm. In the case of Ti = 9%, the relative emission intensity of 555 nm (oxygen vacancies) with respect to 420 nm increased when compared with pure ZnO. This phenomenal suggesting that incorporation of Ti^{4+} ions favors the generation of oxygen vacancies in the material, which would promote the generation of SO species.

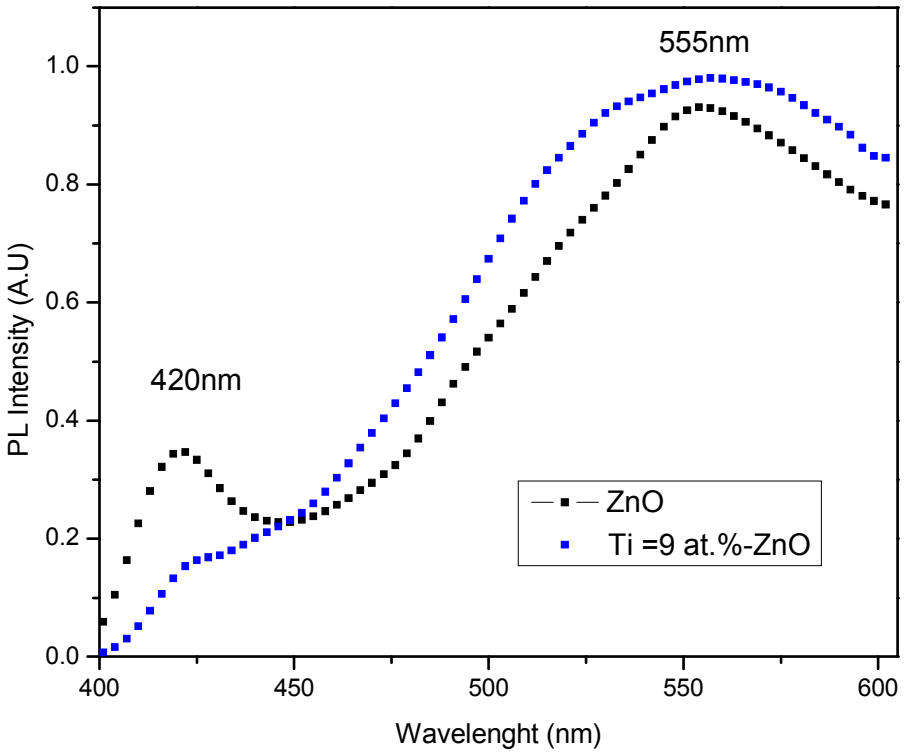

Figure 55. Two photons PL spectra for pure and Ti-doped ZnO-un NPs. The samples were excited using a 690 nm light source.

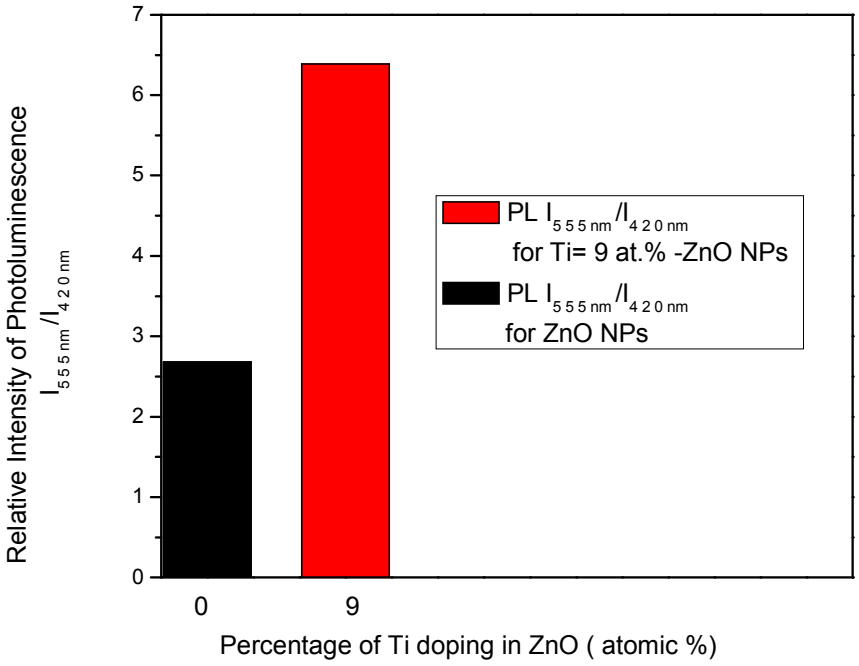

Figure 56. Relative intensity I_{555nm}/I_{420nm} ratio. Ti-doping induced the enhancement of the emission peak at 555nm, which is associated to oxygen vacancies.

4.4.3 Photoluminescence of Li-doped ZnO Nanoparticles

Figure 57 shows the normalized two-photon –excited emission spectra for pure and Li-doped (5 at. %) ZnO NPs. Although the presence of shoulders around 440nm and 555nm becomes evident, they are very broad. The broadening in the two-photon emission peaks can be attributed to the broad particle size distribution in Li-ZnO NPs that was evidenced by SEM analyses. Also in this case, the incorporation of Li species favored the presence of trap states associated to interstitials (around 440nm) and vacancies of oxygen (555nm).

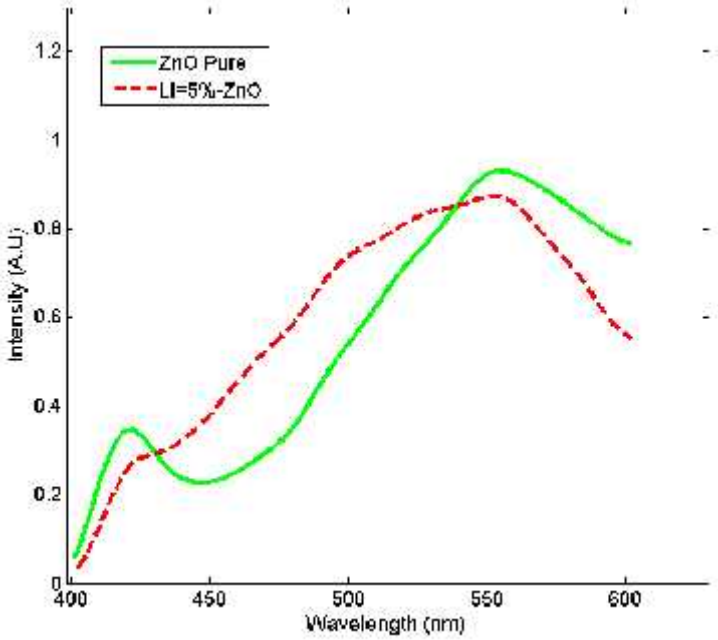

Figure 57. Two-photon-excited emission spectra of pure and Li (5 at. %)-doped ZnO NPs

Concluding Remarks

The incorporation of Ti and Li ions in the ZnO wurtzite structure favored the increase of the concentration of structural defects in ZnO. As-synthesized nanoparticles were photo-excited using a 2- photon light. The TPFM emission peaks observed at 420 nm and 555nm are attributed to the generation of trap states (interstitials and actual doping by Ti and Li ions) and oxygen vacancies in the host oxide, respectively. Evidently, the one-photon and two-photon emission spectra of pure and doped ZnO powders did not match. It can be caused by the use of a laser with light pulse higher than 100 fs that would prevent reaching the electronic states obtained by one-photon Nevertheless, the preliminary two-photon emission spectra evidenced the capability of pure and doped-ZnO NPs to be photo-excited using a 690 nm light source. This fact enables us to suggest that Ti- and Li-ZnO NPs can be considered suitable materials to be used as biomarkers and potential direct SO generators to detect and destroy cancer cells using NIR light.

5. General Conclusions

X-ray diffraction confirmed the formation of polycrystalline pure, Ti- and Li-doped ZnO-wurtzite NPs in the 87-140 nm size range. The monodispersity in pure and doped NPs can be explained in terms of the adsorbed charged species coming from the functional groups of the polyol and acetate compounds used for synthesis. Raman Spectroscopy analyses evidenced the generation of zinc interstitials (Zn_i) and oxygen vacancies (V_O) defects in the host oxide.

Although both pure and doped-ZnO NPs generated SO species, they were the doped samples that reported better results. Among doped samples, the ones with Ti species generated SO species at larger amounts and higher rates while retained intense violet emissions; doping should have favored the formation of trap states (interstitials and oxygen vacancies) which fostered the triplet energy transfer needed to excite molecular oxygen into its SO state. Furthermore, the presence of emission peaks using the two-photons excitation approach confirmed the capacity of Ti-ZnO NPs to be excited by 690-nm light. These emissions transitions will favor those triplet states required to generate cytotoxic reactive oxygen species.

These results enable Ti-ZnO NPs to be considered as an imaging agent for diagnostics and as potential photosensitizer for two-photon photodynamic therapy applications in cancer treatment.

7. References

[1] F. Yang, C. Jin, S. Subedi, C. Lek Lee, Q. Wang, Y. Jiang, J. Li, Y. Di, D. Fu. Emerging inorganic nanomaterials for pancreatic cancer diagnosis and treatment. Cancer Treatment Reviews. **38**, 566-579 (2012).

[2] S. Kumar, W. Ahlawat, R. Kumar, N. Dilbaghi. Graphene, carbon nanotubes, zinc oxide and gold as elite nanomaterials for fabrication of biosensors for healthcare. Biosensors and Biolectronics. **70**, 498-503 (2015).

[3] S.Nazir, T. Hussain, A. Ayub, U. Rashid, A. MacRobert. Nanomaterials in combating cáncer: Therapeutic applications and developments. Nanomedicine: Nanotechnology, Biology, and Medicine. **10**, 19-34 (2014).

[4] S American Association for Cancer Research. AACSR Cancer Progress Report 2014. Clin Cancer Res; 20(Supplement 1): SI-S112 (2014).

[5] G. Schoots, N. Petrides, F. Giganti, L. Bokhorst, A. Rannikko, L. Klotz, A. Villers, J. Hugosson, C. Moore. Magnetic Resonance Imaging in Active Surveillance of Prostate Cancer: A systematic Review. European Urology. **67**, 627-636 (2015).

[6] D. Zippel, V. Tsehmaister-Abitbol, A. Rundstein, A. Shalmon, A. Zbar, G. Nardini, I. Novikov, M. Sklair-Levy. Magnetic Resonance Imaging (MRI) evaluation of residual breast tissue following mastectomy and reconstruction with silicone implants. Clinical Imaging .**39**, 408-411 (2015).

[7] H. Kim, J. Kim, H. Chung, H. Kim, Y. Kim, B. Kim, W. Kim, N. Park, Y. Song, S. Kang. Significance of numbers of metastatic and removed lymph nodes in FIGO stage IB1 to IIA cervical cancer: Primary surgical treatment versus neoadjuvant chemotherapy before surgery. Gynecologic Oncology. **121**, 551-557 (2015).

[8] Y. Kim, Y. Choi, S. Kim, Y. Park, I. Oh, K. Kim, Y. Kim. Conventional cancer treatment alone or with regional hyperthermia for pain relief in lung cancer: A case-control study. Complementary Therapies in Medicicine.doi: http://dx.doi.org/10.1016/j.ctim.2015.04.004 (2015).

[9] R. Hudson, R. Boyle. Strategies for selective delivery of photodynamic sensitisers to biological targets. J Porphyrins Phthalocyanines. **8**, 954 (2004).

[10] A. Garg, D. Nowis, J. Golab , P. Agostinis. Photodynamic therapy: illuminating the road from cell death towards anti-tumor immunity. Apoptosis. **15**, 1050–1071 (2010).

[11] Z. Chen, P. Xu, J. Chen, H. Chen, P. Hu, X. Chen, L. Lin, Y. Huang, K. Zheng, S. Zhou, S. Chen, J. Liu, J. Xue, M. Huang. Zinc phthalocyanine conjugated with the amino-terminal fragment of urokinase for tumor-targeting PDT. Acta Biomaterialia. **10,** 4257-4268 (2014).

[12] D. Bechet, P. Couleaud, C. Frochot, M. Viriot, F. Guillemin and M. Barberi-Heyob. Nanoparticles as vehicles for delivery of photodynamic therapy agents. Trends in Biotechnology. **10,** 4257-4268 (2014).

[13] R. Alisson, CH. Siabata. Oncologic photodynamic therapy photosensitizers: a clinical review. Photodiagnosis Photodyn Ther. **7,** 61-75 (2010).

[14] M. Mansoor. Nanotechnology for Cancer Therapy. CRC Press, p.59 (2006).

[15] R. Braj, N. Brahma, W. Khan, H. Singh, A. Naqvi. ROS-mediated apoptotic cell death in prostate cancer LNCaP cells induced by biosurfactant stabilized CdS quantum dots. Biomaterials. **33**, 5753 (2012).

[16] L. Honglin, Z. Zhong, H. Jinzhao, L. Ruxi, W. Qingbao. Optical and structural analysis of rare earth and Li co-doped ZnO nanoparticles. Journal of Alloys and Compounds. **550**, 526-530(2013).

[17] Y. Xia, S. Huali, L. Weirong, G. Weizhong, S. Xiaoli, M. Yiqun. Endoplasmic reticulum stress and oxidative stress are involved in ZnO nanoparticle-induced hepatotoxicity. Toxicology Letters. **234**, 40-49(2015).
[18] T. Maldiney, B. Viana, A. Bessière, D. Gourier d,e , M. Bessodes, D. Scherman, C. Richard. In vivo imaging with persistent luminescence silicate-based nanoparticles. Optical Materials.**35,** 1852–1858 (2013).
[19] V. Shanov, Y. Yun. Nanomedicine Design of Particles, Sensors, Motors, Implants, Robots, and Devices. Artech House (2009).
[20] B. Kim, J. Rutka, Warren Chan. Nanomedicine. N. Engl J Med. **363**, 2434-43 (2010).
[21] L. Tzu-yin, C. Rodriguez, Y. Li. Nanomedicine in veterinary oncology. The Veterinary Journal. **205**, 189-197 (2015).
[22] K. Krishna, Y. Li, S. Li, C Kumar. Lab-on-a-chip synthesis of inorganic nanomaterials and quantum dots for biomedical applications. Advanced Drug Delivery Reviews. **65**, 1470-1495 (2013).
[23] M. Joula, M. Farbod. Synthesis of uniform and size-controllable carbon nanospheres by a simple hydrothermal method and fabrication of carbon nanospheresuper-hydrophobic surface. Applied Surface Science. **347**, 535–540 (2015).
[24] X. Huang, S. Tang, H.Zhang, Z. Zhou, N.Zheng. Controlled Formation of Concave Tetrahedral/Trigonal Bipyramidal Palladium Nanocrystals. J. Am. Chem. Soc.131, 13916–13917(2009).
[25] J.Burne. Photodynamic Therapy (PDT). Source: http://www.dailymail.co.uk/health/article-1022018/A-ray-light-Beams-light-used-diagnose-AND-treat-cancer--arent-patients-told.html
[26] Xian Chen, Dengfeng Peng and Feng Wang. Tuning $NaYF_4$ Nanoparticles through Alkaline Earth Doping. Nanomaterials.**3**, 583-591 (2013).
[27] J. Lai, W. Niu, R. Luque, G. Xu. Solvothermal synthesis of metal nanocrystals and their applications. Nano Today. **10**, 240—267 (2015).
[28] J. Wang. ZnO Nanotubes. http://nanotechweb.org/cws/article/lab/41156
[29] S. Lamrani, A. Guittoum, R. Schäfer, M. Hemmous, V. Neu, S. Pofahl, T. Hadjersi, N. Benbrahim. Morphology, structure and magnetic study of permalloy films electroplated on silicon nanowires . Journal of Magnetism and Magnentic Materials. http://dx.doi.org/10.1016/j.jmmm.2015.07.111
[30] R. Jin, H. Liu, Y. Guan, J. Zhou, G. Chen. ZnFe2O4/C nanodiscs as high performance anode material forlithium- ion batteries. MaterialsLetters. **158**, 218–221 (2015).
[31] V. Kazmiruk . Scanning Electron Microscopy. InTech (2012).
[32] Z. Chen, C. Zhang, Q. Wu, K. Li, L. Tan. Application of triangular silver nanoplates forcolorimetric detection of H2O2. Sensors and Actuators B. **220**, 314–317 (2015).
[33] D. Spencer, A. Puranik and N. Peppas. Intelligent nanoparticles for advanced drug delivery in cancer treatment. Current Opinion in Chemical Engineering. **7**, 84–92 (2015).
[34] R. Heukers, P. Bergen, S. Oliveira. Nanobody–photosensitizer conjugates for targeted photodynamic therapy. Nanomedicine: Nanotechnology, Biology, and Medicine. **10**, 1441–1451 (2014).
[35] R. Malik, A. Manocha. Photodynamic therapy- A strategic review. Indian Journal of dental research. **21**, 285-291(2010).
[36] K. Winckler. Special section: Focus on anti-microbial photodynamic therapy (PDT). J.Photochem. Photobiol. B Biol.**86**, 43–44 (2007).
[37] H. Mahmoud, A. Kader.Photodynamic therapy. From theory to application. Editors: Abdel-Kader**,** Mahmoud H. Springer Berlin Heidelberg; 1 edition, pp.6-7 (2014).
[38] S. Reddy, K. Tatapudi. Photo Dynamic Therapy in Oral DIseases. Int J Biol Med Res.**3**, 1875-1883(2012).
[39] M. Gold. Photodynamic therapy in Dermatology. Springer, pp. 2 (2011).

[40] A. Ormond, H. Freeman. Dye Sensitizers for Photodynamic Therapy. Materials. **6**, 817-840 (2013).

[41] A. Castano, T. Demidova, M. Hamblin. Mechanisms in photodynamic therapy: part one—photosensitizers, photochemistry and cellular localization. Photodiagnosis and Photodynamic Therapy. **1**, 279-293 (2004).

[42] L. Luan, L.Ding, W.Zhang, J.Shi, X.Yu, W.Liu. A naphthalocyanine based near-infrared photosensitizer: synthesis and in vitro photodynamic activities.. Bioorganic & Medicinal Chemistry Letters. **23**, 3775-3779 (2013).

[43] S. Lee, H. Koo, D. Lee,S.Min, S. Lee, X. Chen.Tumor-homing photosensitizer—conjugated glycol chitosan nanoparticles for synchronous photodynamic imaging and therapy based on cellular on/off system. Biomaterials.**32**, 4021-4029 (2011).

[44] R. Davies, D. Jans, K. Wagstaff. Use of fluorescence photobleaching techniques to measure the kinetics of intracellular transport. Microscopy: Science, Technology, Applications and Education (2010).

[45] B. McIlroy, T. Mann, J. Dysart, Brian C.The effects of oxygenation and photosensitizer substrate binding on the use of fluorescence photobleaching as a dose metric for photodynamic therapy. Vibrational Spectroscopy. **28** , 25-35 (2002).

[46] A. Master, M. Livingston, A. Gupta. Photodynamic nanomedicine in the treatment of solid tumors: Perspectives and challengues. Journal of Controlled Realese **168**, 88-102 (2013).

[47] R. Potter.Photodynamic Therapy with ALA: A Clinical Handbook.RCS Publishing (2006).

[48] S. B. Brown, E. A. Brown, and I. Walker, "The present and future role of photodynamic therapy in cancer treatment," Lancet Oncology. **5**, 497–508 (2004).

[49] Živilė Lukšienė. Photodynamic therapy: mechanism of action and ways to improve the efficiency of treatment. Medicina (Kaunas). **39**, 1137-50. (2003).

[50] A. Vargas. In vivo photodynamic activity of photosensitizer-loaded nanoparticles: Formulation properties, administration parameters and biological issues involved in PDT outcome. Eur J Pharm Biopharm. **69**,43-53 (2008).

[51] Advanced Clinical Research.Termoporfin. http://advancedcr.net/html/foscan.htm

[52] J.Burne. Photodynamic Therapy (PDT). Source: http://www.dailymail.co.uk/health/article-1022018/A-ray-light-Beams-light-used-diagnose-AND-treat-cancer--arent-patients-told.html

[53] Pholitelic. Photodynamic Therapy (PDT). http://www.photolitec.org/Tech_PDT.html

[54] X. Ragàs, M. Agut M, S. Nonell. Singlet oxygen in E. coli: New insights for antimicrobial photodynamic therapy. Free Radic. Biol. Med. **49**, 770–776 (2010).

[55] O. Yaman, B. Yaman, F. Aydın, A. Var, C. Temiz. Hyperbaric oxygen treatment in the experimental spinal cord injury model. The spine journal:**14**, 2184-2194 (2014).

[56] Dr. Jockers. The Health Benefits of HyperBaric Oxygen Therapy. http://drjockers.com/health-benefits-hyperbaric-oxygen-therapy/

[57] J. Lord. Hyperbaric Oxygen Therapy. http://nexusilluminati.blogspot.com/2014/08/alternative-cancer-cures-that-work-your.html

[58] A. Tavares, C. Carvalho, M. Faustino, M. Neves, J. Tomé, A. Tomé, J. Cavaleiro,Â. Cunha, N. Gomes, E. Alves, and A. Almeida. Antimicrobial Photodynamic Therapy: Study of Bacterial Recovery Viability and Potential Development of Resistance after Treatment. Mar Drugs. **8**, 91–105. (2010).

[59] X. Ragas, X. He, R. Augut, A. Gonsalves, A. Serra, S. Nonell. Singlet oxygen in antimicrobial photodynamic therapy: photosensitizer-dependent production and decay in E. coli. Molecules. **18**, 2712-25 (2013).

[60] N. Khandge, S. Pradhan, Y. Doshi, A. Kulkarni, I. Dhruva. Photodynamic Therapy (Part 1: Applications in Dentistry). Int J Laser Dent. **3**,7-13 (2013).

[61] L. Pérez-Pérez, J. García-Gavín, Y. Gilaberte. Daylight-mediated photodynamic therapy in Spain: advantages and disadvantages. Actas Dermosifiliogr. 105, 663-674 (2014).

[62] U.S. National Library of Medicine. Mitosis Process. http://ghr.nlm.nih.gov/handbook/howgeneswork/cellsdivide

[63] M. Scholz and R. Dědic. New Trends in Photodynamic Therapy Research. WDS'12 Proceedings of Contributed Papers, Part III, 46–51 (2012).

[64] Z. Yu, H. Li, Li-Ming Zhang, Z. Zhu, L.Yang. Enhancement of phototoxicity against human pancreatic cancer cells with photosensitizer-encapsulated amphiphilic sodium alginate derivative nanoparticles. International journal of pharmaceutics. **1**,501-509 (2014).

[65] P. Fu, Q. Xia, H. Hwang, P. Ray, H. Yu. Mechanisms of nanotoxicity: Generation of reactive oxygen species. Journal of Food and Drug Analysis. **22**, 64-75(2014).

[66] D. Chatterjee, L. Fong, Y. Zhang. Nanoparticles in photodynamic therapy: An emerging paradigm. Advanced Drug Delivery Reviews. 60, 1627-1637 (2008).

[67] L. Cao, P. Xue, H. Lu, Q. Zheng, Z. Wen, Z. Shao. Hematoporphyrin derivative-mediated photodynamic therapy inhibits tumor growth in human cholangiocarcinoma in vitro and in vivo. Hepatol Res. **39**,1190-1197 (2009).

[68] G. Gobe, D. Crane. Mitochondria, reactive oxygen species and cadmium toxicity in the kidney. Toxicology Letters. **198**, 49–55 (2010).

[69] L. Li, B. Bae, T. Tran, K. Yoon, K. Na, K. Moo Huh. Self-quenchable biofunctional nanoparticles of heparin–folate-photosensitizer conjugates for photodynamic therapy. Carbohydrate Polymers. **86** , 708-715 (2011).

[70] Physical vs. Chemical Sunscreen. http://www.skinacea.com/sunscreen/physical-vs-chemical-sunscreen.html

[71] Photodynamic therapy of melanoma skin cancer using carbon dot - chlorin e6 - hyaluronate conjugate. Acta Biomater. **15**,295-305 (2015).

[72] X. Xu, W. Ho, X. Zhang, N. Bertrand, O. Farokhzad. Cancer nanomedicine: from targeted delivery to combination therapy. Trends Mol Med. **21**, 223-232(2015).

[73] K. Sattler. Handbook of Nanophysics: Nanomedicine and Nanorobotics. CRC Taylor & Francis (2006).

[74] D.Larsen . Excited States Produces Fluorescence and Phosphorescence. http://chemwiki.ucdavis.edu/Physical_Chemistry/Spectroscopy/Electronic_Spectroscopy/Electronic_Spectroscopy%3A_Theory

[75] McCaughan, J. S. Photodynamic Therapy - A Review. Drugs & Aging. **15**, 49-68 (1999).

[76] F. Cieplik, A. Späth, J. Regensburger, A. Gollmer, L. Tabenski, K. Hiller, W. Bäumler , T. Maisch and G. Schmalz. Photodynamic biofilm inactivation by SAPYR - An exclusive singlet oxygen photosensitizer. Free Radic. Biol. Med. **65**, 477–487 (2013).

[77] R. Weijer, M. Broekgaarden, R. Vught, E. Breukink, T. Gulik, M. Heger. Enhancing photodynamic therapy of refractory solid cancers: combining second-generation photosensitizers with multi-targeted liposomal delivery. Free Radical Biology and Medicine .**23**, 103-131 (2015).

[78] T. Nyokong, V. Ahsen. Photosensitizers in Medicine, Environment, and Security. Springer (2012).

[79] N. James, T. Ohulchanskyy, Y. Chen, P. Joshi, X. Zheng, L. Goswami, R. Pandey. Nadine S. James et al.Comparative Tumor Imaging and PDT Efficacy of HPPH Conjugated in the Mono- and Di-Forms to Various Polymethine Cyanine Dyes. Theranostics. **3**, 703-718 (2013).

[80] R. Lehner, X. Wang, S. Marsch, P. Hunziker. Intelligent nanomaterials for medicine: Carrier platforms and targeting strategies in the context of clinical application. Nanomedicine: Nanotechnology, Biology and Medicine. **9**, 742-757 (2013).

[81] S. Jin and K. Ye. Nanoparticle-Mediated Drug Delivery and Gene Therapy. Biotechnol. Prog. 23, 32-41 (2007).

[82] M. Dabrzalska, M. Zablocka, S. Mignani, J. Majoral, B. Klajnert-Maculewicz. Phosphorus dendrimers and photodynamic therapy. Spectroscopic studies on two dendrimer-

photosensitizer complexes: Cationic phosphorus dendrimer with rose bengal and anionic phosphorus dendrimer with methylene blue. International Journal of Pharmaceutics. **492**, 266–274 (2015).

[83] N. Dayyani, S. Khoee, A. Ramazani. Design and synthesis of pH-sensitive polyamino-ester magneto dendrimers: Surface functional groups effect on viability of human prostate carcinoma cell lines DU145. European Journal of Medicinal Chemistry. **98**, 190-202 (2015).

[84] X. Qi, Y. Fan, H. He, Z. Wu. Hyaluronic acid-grafted polyamidoamine dendrimers enable long circulation and active tumor targeting simultaneously. Carbohydrate Polymers. **126**, 231–239 (2015).

[85] G. Soni, K. Yadav. Nanogels as potential nanomedicine carrier for treatment of cancer: A mini review of the state of the art. Saudi Pharmaceutical Journal (2014). http://dx.doi.org/10.1016/j.jsps.2014.04.001

[86] S. Manchun, C. Dass, K. Cheewatanakornkool,P. Sriamornsak. Enhanced anti-tumor effect of pH-responsive dextrin nanogelsdelivering doxorubicin on colorectal cancer. Carbohydrate Polymers. **126**, 222–230 (2015).

[87] X. Wang, D. Niu, Q. Wu, S. Bao, T. Su, X. Liu, S. Zhang, Q. Wang. Iron oxide/manganese oxide co-loaded hybrid nanogels as pH-responsive magnetic resonance contrast agents. Biomaterials. **53**, 349-357 (2015).

[88] N. Dayyani, S. Khoee, A. Ramazani. Design and synthesis of pH-sensitive polyamino-ester magnetodendrimers: Surface functional groups effect on viability of human prostate carcinoma cell lines DU145. European Journal of Medicinal Chemistry. **98**,190-202 (2015).

[89] S. Patra, S. Mukherjee, A. Kumar, A. Ganguly, B. Sreedhar, C.Ranjan. Green synthesis, characterization of gold and silver nanoparticles and their potential application for cancer therapeutics. Materials Science and Engineering C. **53**, 298–309, (2015).

[90] E. Petryayeva, J. Krull. Localized surface plasmon resonance: Nanostructures, bioassays and biosensing—A review. Analytica Chimica Acta. **706**, 8-24 (2011).

[91] M. Singh, D. Harris-Birtill, R. Markar, G. Hanna, D. Elson. Application of gold nanoparticles for gastrointestinal cancer theranostics: a systematic review. Nanomedicine: Nanotechnology, Biology, and Medicine. **11**, 2083-2098 (2015).

[92] A. Ravindran, P. Chandran, S. Khan. Biofunctionalized silver nanoparticles: Advances and prospects. Colloids and Surfaces B: Biointerfaces. **105**, 342– 352 (2013).

[93] N. Roy,A. Gaur,A. Jain, S. Bhattacharya, V. Rani. Green synthesis of silver nanoparticles: An approach to overcome toxicity. environmental toxicology and pharmacology. **36**, 807–812 (2013).

[94] C. Lappas. The immunomodulatory effects of titanium dioxide and silver nanoparticles. Food and Chemical Toxicology. (2015). doi:10.1016/j.fct.2015.05.015

[95] T. Shalaby, N. Fekry, A. Sodfy, A. Sheredy, M. Moustafa. Preparation and characterisation of antibacterial silver-containing nanofibres for wound healing in diabetic mice. Int. J. Nanoparticles. **8**, 82-98 (2015).

[96] J. Donegan and Y. Rakovich. Cadmiun Telluride Quantum Dots: Advances and Applications. CRC Taylor & Francis. (2013).

[97] E. Shibu, M. Hamada, N. Murase, V. Biju. Nanomaterials formulations for photothermal and photodynamic therapy of cancer. Journal of Photochemistry and Photobiology C: Photochemistry Reviews. **15**, 53– 72 (2013).

[98] Z. Aguilar. Nanomaterials for medical applications. Elsevier. (2012).

[99] Y. Volkov. Quantum dots in nanomedicine: recent trends, advances and unresolved issues. Biochemical and Biophysical Research Communications. (2015). doi:10.1016/j.bbrc.2015.07.039

[100] M. Lima-Tenório, E. Gómez Pineda, N. Ahmad, H. Fessi, A. Elaissari. International Journal of Pharmaceutics. **493**, 313–327 (2015).

[101] A. Akbarzadeh, M. Samiei and S. Davaran. Magnetic nanoparticles: preparation, physical properties, and applications in biomedicine. Nanoscale Research Letters. **7**, 144 (2012). doi: 10.1186/1556-276X-7-144

[102] G. Reju, M. Myeong, L. Hyegyeong, R. Arathyram, K. Cheol, P. In-Kyu, J. Yong. Hyaluronic acid conjugated superparamagnetic iron oxidenanoparticle for cancer diagnosis and hyperthermia therapy. Carbohydrate Polymers. **131**, 439–446 (2015).

[103] L. Varon, H. Barreto, G. Enrique. Estimation of state variables in the hyperthermia therapy of cancer with heating imposed by radiofrequency electromagnetic waves. International Journal of Thermal Sciences. **98**, 228-236 (2015).

[104] National Cancer Institute. Hyperthermia in Cancer Treatment. http://www.cancer.gov/about-cancer/treatment/types/surgery/hyperthermia-fact-sheet

[105] D. Tukmachev , O. Lunov, V. Zablotskii, A. Dejneka, M. Babic, E. Syková and Š. Kubinová. An effective strategy of magnetic stem cell delivery for spinal cord injury therapy. Nanoscale**. 7**, 3954-3958 (2015).

[106] O. Dössel. Calculation and Evaluation of Current Densities and Thermal Heating in the Human Body. https://www.ibt.kit.edu/english/2039.php

[107] E. Tomb, R. Turcu, V. Socoliuc. Magnetic iron oxide nanoparticles: Recent trends in design and synthesis of magnetoresponsive nanosystems. Biochemical and Biophysical Research Communications. (2015). doi:10.1016/j.bbrc.2015.08.030

[108] B. Johnson, S. Gilbert, B. Khan, D. Carroll,A. Ringwood. Cellular responses of eastern oysters, Crassostrea virginica, to titanium dioxide nanoparticles. Marine Environmental Research. **11**, 135-143 (2015).

[109] S. Fragomeni & S. Venkatesan. Incorporating Sustainable Practice in Mechanics of Structures and Materials. CRC Taylor & Francis. (2011).

[110] N. Daels, M. Radoicic, M. Radetic, K. De Clerck, S. Van Hulle. Electrospun nanofibre membranes functionalised with TiO2 nanoparticles: Evaluation of humic acid and bacterial removal from polluted water. Separation and Purification Technology. **149**, 488–494 (2015).

[111] R. Wahab, M. Siddiqui, Q. Saquib, S. Dwivedi, J. Ahmad, J. Musarrat, A. Al-Khedhairy, H. Shin. ZnO nanoparticles induced oxidative stress and apoptosis in HepG2and MCF-7 cancer cells and their antibacterial activity. Colloids and Surfaces B: Biointerfaces. **117**, 267–276 (2014).

[112] Z. Sharifalhoseini, M. Entezari, R. Jalal. Direct and indirect sonication affect differently the microstructure and the morphology of ZnO nanoparticles: Optical behavior and its antibacterial activity. Ultrasonics Sonochemistry. **27**, 466–473 (2015).

[113] Haja Bava Bakrudeen, Madurai Sugunalakshmi, Boreddy S.R. Reddy. Auto-fluorescent mesoporous ZnO nanospheres for drug delivery carrier application. Materials Science and Engineering C. **56**, 335–340 (2015).

[114] L. He, Y. Liu, A. Mustapha, M. Lin. Antifungal activity of zinc oxide nanoparticles against Botrytis cinerea and Penicillium expansum. Microbiological Research. **166** (2011) 207—215 (2011).

[115] Padmavathy N, Vijayaraghavan R. Enhanced bioactivity of ZnO nanoparticles — an antimicrobial study. Sci Technol Adv Mater. **9**, 1—7 (2008).

[116] A. Kołodziejczak-Radzimska and T. Jesionowski. Zinc Oxide—From Synthesis Application: A Review. Materials. **7**, 2833-2881 (2014).

[117] S. Ostrovsky, G. Kazimirsky, A. Gedanken, and C. Brodie. Selective Cytotoxic Effect of ZnO Nanoparticles on Glioma Cells. Nano Res. **2**, 882- 890 (2009).

[118] K. M. Reddy, Kevin Feris, Jason Bell, Denise G. Wingett, Cory Hanley, and Alex Punnoose. Selective toxicity of zinc oxide nanoparticles to prokaryotic and eukaryotic systems. Appl Phys Lett. **24**, 1–3 (2007).

[119] L. Zhang, Y. Jiang, Y. Ding, M. Povey, D. York. Investigation into the antibacterial behaviour of suspensions of ZnO nanoparticles (ZnO nanofluids), J. Nanopart. Res. **9**, 479–489 (2007).
[120] H. Zhang, B. Chen, H. Jiang, C. Wang, H. Wang, X. Wang. A strategy for ZnO nanorod mediated multi-mode cancer treatment. Biomaterials **32**, 1906-1914 (2011).
[121] J. Rasmussen, E. Martinez, P. Louka, D. Wingett. Zinc oxide nanoparticles for selective destruction of tumor cells and potential for drug delivery applications, Expert Opin. Drug Deliv. **7**, 1063–1077 (2010).
[122] A. Nel, T. Xia, L. Madler, N. Li. Toxic Potential of Materials at the Nano level. Science. **311**,622–627 (2006).
[123] D. Wang, D. Guo, H. Bi, Q. Wu, Q. Tian, Y. Du. Zinc oxide nanoparticles inhibit Ca2+-ATPase expression in human lens epithelial cells under UVB irradiation. Toxicology in Vitro. **27**, 2117–2126 (2013).
[124] R. Hariharan, S. Senthilkumar, A. Suganthi, M. Rajarajan. Synthesis and characterization of doxorubicin modified ZnO/PEG nanomaterials and its photodynamic action. Journal of Photochemistry and Photobiology B: Biology. **116**, 56–65 (2012).
[125] L. Rivas, G. Mellor, K. Gobius, N. Fegan. Detection and lyping strategies for pathogenic Escheria Coli. Springer. (2015).
[126] L. Zhang, Y. Ding, M. Povey, D. York. ZnO nanofluids – A potential antibacterial agent. Progress in Natural Science. **18**, 939–944 (2008).
[127] K. Kairyte, A. Kadys, Z. Luksiene. Antibacterial and antifungal activity of photoactivated ZnO nanoparticles in suspension. Journal of Photochemistry and Photobiology B: Biology. **128**, 78–84 (2013).
[128] A. Sirelkhatim, S. Mahmud, A. Seen, N. Mohamad, L. Ann, S. Bakhori, H. Hasan, D. Mohamad. Review on Zinc Oxide Nanoparticles: Antibacterial Activity and Toxicity Mechanism.Nano-Micro Lett. **7**, 213-242 (2015).
[129] B. Smith, P. Kempen, D. Bouley, A. Xu, Z. Liu, N. Melosh, H. Dai, R. Sinclair, S. Gambhir. Shape matters: intravital microscopy reveals surprising geometrical dependence for nanoparticles in tumor models of extravasation. Nano Lett. **12**, 3369-77 (2012).
[130] D. Jo, J. Kim, T. Lee, J. Kim. Size, surface charge, and shape determine therapeutic effects of nanoparticles on brain and retinal diseases. Nanomedicine. **11**, 1603-11 (2015).
[131] M. Arachchige, Y. Reshetnyak, O. Andreev. Advanced targeted nanomedicine. J Biotechnol. **202**, 88-97 (2015).
[132] K. Nagaraja, S. Pramodini, A. Santhosh, H. Nagaraja, P. Poornesh, D. Kekuda. Third-order nonlinear optical properties of Mn doped ZnO thin films under cw laser illumination. Optical Materials. **35**, 431–439 (2013).
[133] Q. Ouyang, Z. Xu, Z. Lei, H. Dong, H. Yu, L. Qi, C. Li, Y. Chen. Enhanced nonlinear optical and optical limiting properties of graphene/ZnO hybrid organic glasses. Carbon. **6 7**, 2 1 4 –2 2 0 (2014).
[134] Z. Zhang and H.Xiong. Photoluminescent ZnO Nanoparticles and Their Biological Applications. Materials. **8**, 3101-3127 (2015).
[135] M. Reinke, C. Canakis, D. Husain, N. Michaud, T. Flotte, E. Gragoudas & J. Miller. Verteporfin photodynamic therapy retreatment of normal retina and choroid in the cynomolgus monkey. Ophthalmology. **106**, 1915-1923 (1999).
[136] Y. Yang, Q. Shao, R. Deng, C. Wang, X. Teng, K. Cheng, et al. In Vitro and In Vivo Uncaging and Bioluminescence Imaging by Using Photocaged Upconversion Nanoparticles. Angew Chem. **51**, 3125-3129 (2012).

[137] J. Qian, D. Wang, F. Cai, Q. Zhan, Y. Wang, S. He. Photosensitizer encapsulated organically modified silica nanoparticles for direct two-photon photodynamic therapy and In Vivo functional imaging. Biomaterials. **33**, 4851-60 (2012).

[138] M. Oheim, D. Michael, M. Geisbauer, D. Madsen & R. Chow. Principles of two-photon excitation fluorescence microscopy and other nonlinear imaging approaches. Advanced Drug Delivery Reviews. **58**, 788-808 (2006).

[139] K. Samkoe. Two-photon excitation photodynamic therapy: Progress towards a new treatment for wet age-related macular degeneration. PhD thesis submitted to the Department of Chemistry, University of Calgary, Calgary, Canada (2007).

[140] B. Wilson and M. Patterson. "The physics, biophysics and technology of photodynamic therapy." Physics in medicine and biology. **53**, 61–109 (2008).

[141] S. Abed, M. Aida, K. Bouchouit, A. Arbaoui, K. Iliopoulos, B. Sahraoui. Non-linear optical and electrical properties of ZnO doped Ni Thin Films obtained using spray ultrasonic technique. Optical Materials. **33**, 968–972 (2011).

[142] L. Bonacina. ¨Nonlinear nanomedicine: Harmonic nanoparticles toward targeted diagnosis and therapy¨. Mol. Pharmaceutics. **10**, 783-792 (2013).

[143] P.Yadav et al. Synthesis of two-photon active cinnamoyl coumarins for high-contrast imaging of cancer cells and their photophysical characterization.Journal of Photochemistry and Photobiology A: Chemistry. **280**, 39–45 (2014).

[144] X. Zhang, Z. Tang, M. Kawasaki, A. Ohtomo and H. Koinuma, Z. Tang, M. Kawasaki, A. Ohtomo and H. Koinuma. Resonant exciton second-harmonic generation in self-assembled ZnO microcrystallite thin films. Journal of Physics: Condensed Matter. Thin Solid Films. **15**,30, (2003).

[145] A. Janotti and C. Van de Walle. Fundamentals of zinc oxide as a semiconductor. Rep. Prog. Phys. **72**, 126501 (2009).

[146] R. Sreeja, J. John, P. Aneesh, and M. Jayaraj. "Linear and nonlinear optical properties of luminescent ZnO nanoparticles embedded in PMMA matrix." Optics Communications. **283**, 2908–2913 (2010).

[147] Z.Feng. Handbook of Zinc Oxide and Related Materials Volume One, Materials. CRC Taylor & Francis (2012).

[148] T. Yu-Chih, L. Yow-Jon, C. Hsing-Cheng, C. Ya-Hui, L. Chia-Jyi, Z. Yi-Yan. Dependence of luminescent properties and crystal structure of Li-doped ZnO nanoparticles upon Li content. Journal of Luminescence **132**, 1896-1899(2012).

[149] A. Djuriić, A. Ng, X. Chen.ZnO nanostructures for optoelectronics: Material properties and device applications. Progress in Quantum Electronics. **34**, 191-259 (2010).

[150] Y.Collantes Goicochea.Synthesis and Characterization of ZnO-based Nanostructures for Potential Biomedical Applications. Thesis of Master of Science. University of Puerto Rico, Mayaguez Campus 2013.

[151] P. Juzenas, W. Chen, Y. Sun, M. Coelho, R. Generalov, N. Generalova, I. Christensen. Quantum dots and nanoparticles for photodynamic and radiation therapies of cancer. Advanced Drug Reviews. **60**, 1600-1614 (2008).

[152] X. Wang, J. Song, and Z. L. Wang. "Single crystal nanocrastles of ZnO." Chem. Phys. Lett. 424, 86–90 (2006).

[153] Ü. Özgür, Ya. Alivov, C. Liu, A. Teke, M. Reshchikov, S. Doğan, V. Avrutin, S. Cho, H. Morkoç. A comprehensive review of ZnO materials and devices. J. Appl. Phys. **98**, 041301 (2005).

[154] Z. Chuan Feng. Handbook of Zinc Oxide and Related Materials Volume One, Materials. CRC Taylor & Francis (2012).

[155] A. Filipetti, V. Fiorentini, G. Capellini, A. Bosin. Anomalous relaxations and chemical trends at III-V semiconductor nitride nonpolar surfaces. Phys. Rev. B. **59**, 8026 (1999).

[156] H. Morkoc, U. Özgür, Zinc Oxide: Fundamentals, Materials and Device Technology, Wiley-VCH Verlag GmbH Co, &Wienheim (2009).
[157] Yamin Leprince-Wang. Piezoelectric ZnO Nanostructure for Energy Harvesting, Volume 1. Wiley-VCH Verlag GmbH Co, &Wienheim (2015).
[158] Z. Lin Wang. ZnO nanowire and nanobelt platform for nanotechnology. Materials Science and Engineering: R. Reports. 64, 33-71 (2009).
[159] Rocksalt structure. https://markforeman.wordpress.com/category/crystals/page/3/
[160] ZnO structure.http://www.en.wikipedia.org/wiki/Zinc_oxide
[161] S. Shionoya and W. M. Yen, Phosphor Handbook. Boca Raton, Florida: Phosphor Research Society (1997).
[162] Semiconductor of direct band gap: http://www.zhihu.com/topic/19679406
[163] E. A. Meulenkamp, Synthesis and Growth of ZnO Nanoparticles. J. Phys. Chem. B. **102**, 5566–5572 (1998).
[164] Ch. Poole, F. Owens. Introduction to Nanotechnology. John Willey and Sons (2003).
[165] W. Fan, J. Xia, P. Agus, S. Tan, S. Yu, X. Sun. Band parameters and electronic structures of wurtzite ZnO and ZnO/MgZnO quantum wells. JOURNAL OF APPLIED PHYSICS. **99**, 013702 (2006).
[166] A. Mang, K. Reimann, and S. Rübenacke. Band gaps, crystal-field splitting, spin-orbit coupling, and exciton binding energies in ZnO under hydrostatic pressure. Solid State Commun. **94**, 251–254 (1995).
[167] L. Irimpan, V.P.N. Nampoori, and P. Radhakrishnan. Visible luminescence mechanism in nano ZnO under weak confinement regime. Journal of Applied Physics. **104**, 113112 (2008).
[168] S.T. Tan, et al. Blueshift of optical band gap in ZnO thin films grown by metal-organic chemical-vapor deposition. Journal of Applied Physics.**98**, 013505 (2005).
[169] S. Pearton.GaN and ZnO-based Materials and Devices. Springer (2012).
[170] S. Lowe, J. Dick, B. Cohen, M.Stevens. Multiplex sensing of protease and kinase enzyme activity via orthogonal coupling of quantum dot–peptide conjugates. Am. Chem. Soc. Nano. **6**, 851–857 (2012).
[171] A. Dodd, J. McKinley, M. Saunders, and T. Tsuzuki. Effect of Particle Size on the Photocatalytic Activity of Nanoparticulate ZnO. Journal of Nanoparticle Research. **8**, 43–51 (2006).
[172] Rao, M. Ramachandra, Okada, Tatsuo. ZnO Nanocrystals and Allied Materials. Springer (2014).
[173] Yu, Peter, Cardona, Manuel. Fundamentals of Semiconductors. Fourth Edition. Springer (2010).
[174] Frenkel exciton and Mott- Warnier exciton URL:http://www.oe.phy.cam.ac.uk/images/exciton_sketch.jpg
[175] H. Singh Virk. Luminescence:Basic Concepts, Applications and instrumentation. Trans Tech Publications Ltd. Switzerland (2014).
[176] Z. Wang. Zinc oxide nanostructures: growth, properties and applications. J. Phys.: Condens. Matter. **16**, R829–R858 (2004).
[178] P. Atkins, The Elements of Physical Chemistry. Oxford University Press: Oxford (2001).
[179] Semiconductors.http://electronics.howstuffworks.com/diode.htm
[180] Y. Lu, Z. Ye, Y. Zeng, H. He, L. Zhu, B. Zhao. Low-Temperature Growth of p-Type ZnO Thin Films via Plasma-Assisted MOCVD.**13**, 295-297 (2007).
[181] S.M.Park, T. Ikegami, K. Ebihara. Effect of substrate temperature on the properties of Ga-doped ZnO by pulsed laser deposition. Thin Solid Films. **513**, 90 (2006).
[182] T. Yanamoto, H. Katayama-Yoshida. Unipolarity of ZnO with a wide band gap and its solution using coping method. J. Crys.Growth. **214**, 552 (2000).
[183] X. Wang, J. Wu, J. Webb, and Z. Liu. Ferroelectric and dielectric properties of Li-doped ZnO

thin films prepared by pulsed laser deposition. Applied Physics A: Materials Science and Processing. **77**, 561- 565 (2003).
[184] A. Goldman. Modern Ferrite Technology.Van Nostrand Reinhold: New York (1990).
[185] Y. Zhang, M. K. Ram, E. K. Stefanakos, and D. Y. Goswami. Synthesis, Characterization, and Applications of ZnO Nanowires.J. Nanomater. **2012**, 1–22 (2012).
[186] K. Yu, T. Yoon, A. Minai-Tehrani, J. Kim, S. Park, M. Jeong, S. Ha, J. Lee, J. Kim, and M. Cho. Zinc oxide nanoparticle induced autophagic cell death and mitochondrial damage via reactive oxygen species generation. Toxicol. In Vitro. **27**, 1187–1195 (2013).
[187] S. J. Pearton, D. P. Norton, M. P. Ivill, A. F. Hebard, J. M. Zavada, W. M. Chen, and I. a. Buyanova. ZnO Doped with Transition Metal Ions. IEEE Trans. Electron Devices. **54**,1040–1048 (2007).
[188] M. Willander, O. Nur, J. Sadaf, Muhammad Qadir, S. Zaman,A. Zainelabdin , N. Bano and I. Hussain. Luminescence from Zinc Oxide Nanostructures and Polymers and their Hybrid Devices. Materials. **3**, 2643-2667 (2010).
[189] W. Zhang, X. Wu, H. Chen, J. Zhu, and G. Huang. Excitation wavelength dependence of the visible photoluminescence from amorphous ZnO granular films. J. Appl. Phys. **103**, (2008).
[190] K. Vanheusden, W. L. Warren, C. H. Seager, D. R. Tallant, J. A. Voigt, and B. E. Gnade. Mechanisms behind green photoluminescence in ZnO phosphor powders. J. Appl. Phys. **79**, (1996).
[191] V. Ischenko, S. Polarz, D. Grote, V. Stavarache, K. Fink, and M. Driess, "Zinc Oxide Nanoparticles with Defects," Advanced Functional Materials. **15**, 1945–1954 (2005).
[192] Y. Tseng, Y. Lin, H. Chang, Y. Chen, C. Liu, Y. Zou. Effects of Ti content on the optical and structural properties of the Ti-doped ZnO nanoparticles. Journal of Luminescence. **32**, 491-494 (2012).
[193] C. Hsu, Y. Gao, Y. Chen, T. Hsueh. Vertical Ti doped ZnO nanorods based on ethanol gas sensor prepared on glass by furnace system with hotwire assistance. Sensors and Actuators B: Chemical. **192**, 550-557 (2014).
[194] N. Han, L.Y. Chai, Q. Wang, Y.J. Tian, P.Y. Deng, Y.F. Chen. Evaluating the doping effect of Fe, Ti and Sn on gas sensing property of ZnO, Sens. Actuator B: Chem.**147**, 525–530 (2010).
[195] J. Chung, J. Chen, C. Tseng. The influence of titanium on the properties of zinc oxide films deposited by radio frequency magnetron sputtering, Appl. Surf. Sci. **254**, 2615–2620 (2008).
[196] S. Shinde, C. Bhosale, K. Rajpure. Photoelectrochemical properties of higly mobilized Li-doped ZnO thin films. Journal of Photochemistry and Photobiology B: Biology. **120**, 1-9 (2013).
[197] J. Zou, S. Zhou, C. Xia, X. Zhang, F. Su, G. Peng, X. Li, J. Xu. Optical properties of ZnO thin film on c-LiAlO2 substrate grown by pulsed laser deposition. Thin Solid Films. **496**, 205–207 (2006).
[198] K. Vanheusden, C. Seager, W. Warren, D. Tallant, J.Voigt. Correlation between photoluminescence and oxygen vacancies in ZnO phosphors, Appl. Phys. Lett. **68**, 403–405 (1996).
[199] S. Bailon-Ruiz and O. Perales-Perez. UV-enhanced toxicity of water-stable quantum dots in human pancreatic carcinoma cells. Journal of Experimental Nanoscience. **9**, 942-956 (2014)
[200] B. Cullity, Elements of X-ray Diffractions. Addison Wesley, MA, 1972, p. 102.
[201] A. Gomes, E. Fernandes, and J. F. C. ima, "Fluorescence probes used for detection of reactive oxygen species." Journal of biochemical and biophysical methods. **65**, 45–80 (2005).
[202] J. N. Lalena, D. A. Cleary, E. E. Carpenter and N. F. Dean, Inorganic Materials Synthesis a Fabrication, Wiley-Interscience, New Jersey (2008).
[203] W. Cai and J. Wan, "Facile synthesis of superparamagnetic magnetite nanoparticles in liquid polyols." Journal of colloid and interface science. **305**, 366–70 (2007).

[204] R. Wahab, S. Ansari, Y. Kim, M. Song & H. Shin. (2009). The role of pH variation on the growth of zinc oxide nanostructures. Applied Surface Science. **255**, 4891–4896 (2009).
[205] A. Umar, M. Rahman, M. Vaseem & Y. Hahn. (2009). Ultra-sensitive cholesterol biosensor based on low-temperature grown ZnO NPs. Electrochemistry Communications, **11**, 118–121 (2009).
[206] Duan L, Rao G, Wang Y, Yu J, Wang T: Magnetization and Raman scattering studies of (Co, Mn) codoped ZnO nanoparticles. J Appl Phys. **104**, 013909-013913 (2008).
[207] G. Exarhos, S. Sharma. Influence of Processing Variables on the Structure and Properties of ZnO Films. Thin Solid Films. **270**, 27−32 (1995).
[208] J. Serrano, A. H. Romero, F. J. Manjon, R. Lauck, M. Cardona, and A. Rubio. Phys. Rev. B .**69**, 094306 (2004).
[209] D. Motaung, G. Mhlongo, S. Nkosi, G. Malgas, B. Mwakikunga, E. Coetsee,H. Swart, H. Abdallah, T. Moyo, and S. Ray. Shape-Selective Dependence of Room Temperature Ferromagnetism Induced by Hierarchical ZnO Nanostructures. ACS Appl. Mater. Interfaces. **6**, 8981–8995 (2014).
[210] A. Mezni, F. Kouki, S. Romdhane, B. Warot-Fonrose, S. Joulié, A. Mlayah, L. Samia. Facile synthesis of ZnO nanocrystals in polyol. **86**, 153-156 (2012).
[211] A. Anlovar, Z. Crnjak, M. Zigon. Morphology and particle size of di(ethylene glycol) mediated metallic copper nanoparticles. Journal of Nanoscience and Nanotechnology. **8**, 3516–3525 (2008).
[212] A. Anlovar, Z. Crnjak, M. Zigon. Polyol mediated nano size zinc oxide and nanocomposites with poly(methyl methacrylate). Polymer Letters. **5**, 604–619 (2011).
[213] L. PoulL, S. AmmarS, N. JouiniN, F,Villain. Metastable solid solutions in the system ZnO-CoO: synthesis by hydrolysis in polyol medium and study of the morphological characteristics. Solid State Sci. **3**, 31–42 (2001).
[214] S. Chakraborty, P. Kumbhakar. Effect of polyethylene glycol on the particle size and photoluminescence emissions characteristics of chemically synthesized ZnO nanoparticles. Optics Communications. **318**, 61–66 (2014).
[215] S.Repp, E. Erdem. Controlling the exciton energy of zinc oxide (ZnO) quantum dots by changing the confinement conditions. Spectrochimica Acta Part A: Molecular and Biomolecular Spectroscopy. **152**, 637-644 (2015).
[216] J. Chung, J. Chen. Tseng. Preparation of TiO2-doped ZnO films by radio frequency magnetron sputtering in ambient hydrogen–argon gas. Applied Surface Science. **255**, 2494-2499 (2008).

[217] J. Alaria, H. Bieber, S. Colis, G. Schmerber and A. Dinia. Absence of ferromagnetism in Al-doped Zn0.9Co0.10O diluted magnetic semiconductors. Appl. Phys. Lett. **88**, 112503 (2006).
[218] H. Chen, J. Ding, Sh. Ma. Violet and blue-green luminescence from Ti-doped ZnO films deposited by RF reactive magnetron sputtering. Superlattices and Microstructures **49** ,176–182 (2011).
[219] Y. Collantes, O. Perales- Pérez. Structural and Functional Properties of Iron (II, III)-Doped ZnO Monodisperse Nanoparticles Synthesized by Polyol Method. Materials Research Society, 2013.
[220] S. Awan, S. Hasanain, M. Bertino and G. Hassnain. Effects of subtitutional Li on the ferromagnetic response of Li co-doped ZnO:Co nanoparticles. J.Phys.: Condens. Matter,**25**, 156005 (2013).
[221] E. Jeong , H. Yu, Y. Kim, G. Yi, Y. Choi, S. Han. Local structural and optical properties of ZnO nanoparticles. Journal of Nanoscience and Nanotechnology, **10**, 3562-3565(2010).
[222] H. Zeng, G. Duan, Y. Li, S. Yang, X. Xu, and W. Cai. “Blue luminescence of ZnO nanoparticles based on non-equillibrium processes: Defect origins and emission controls.” Adv. Funct. Mater. **20**(4), 561–572 (2010).

[223] S. Chawla, K. Jayanthi, and R. K. Kotnala. Room-temperature ferromagnetism in Li-doped p-type luminescent ZnO nanorods. PHYSICAL REVIEW B. **79**, 125204 (2009).
[224] O. Dulub, L. Boatner, U. Diebold. STM study of the geometric and electronic structure of ZnO (0001)-Zn, (000-1)-O, (10-10), and (11-20) surfaces. Surf. Scie. **519**, 201-217 (2002).